University of Genova

Modelling and Identification of Underwater Robotic Systems

Giovanni Indiveri

Ph.D. Thesis in
Electronic Engineering and
Computer Science

December 1998

DIST
Department of Communications, Computer and Systems Science
University of Genova,
Via all'Opera Pia, 13 C.A.P. 16145 Genova, Italy

CNR-IAN
National Council of Research,
Institute for Naval Automation
Via De Marini, 6 C.A.P. 16149 Genova, Italy

Università degli Studi di Genova

Facoltà di Ingegneria

“Modelling and Identification of Underwater Robotic Systems”

Tesi per il conseguimento del

Dottorato di Ricerca in Ingegneria Elettronica ed Informatica

Giovanni Indiveri

Dicembre 1998

Relatore,
Prof. Ing. Giuseppe Casalino,
DIST, Università di Genova

Co-relatore,
Ing. Gianmarco Veruggio,
CNR-IAN

Coordinatore del corso di Dottorato di Ricerca,
Prof. Ing. Riccardo Zoppoli,
DIST, Università di Genova

Quel che è detto è detto.
Ma sarà poi vero? Io non ho accesso
al vero, il mio pensiero ha un andamento
incerto, è sottoposto al vento
di scirocco, ma so per certo
che questi giorni invernalprimaverili
sono un eccesso inutile di luce e a me
non è concesso che attraversare i ponti
e al rosso del semaforo guardare con invidia
qualche ossesso che tra bestemmie e insulti
a passo lento infrange l'armata compatta
delle macchine. E basta, non c'è che questo.

(*Patrizia Cavalli*,
POESIE (1974-1992)
Giulio Einaudi Editore, 1992)

ABSTRACT

Whatever is the strategy pursued to design a control system or a state estimation filter for an underwater robotic system the knowledge of its identified model is very important. As far as ROVs are concerned the results presented in this thesis suggest that low cost on board sensor based identification is feasible: the detailed analysis of the residual least square costs and of the parameter estimated variances show that a decoupled vehicle model can be successfully identified by swimming pool test provided that a suitable identification procedure is designed and implemented. A two step identification procedure has been designed on the basis of: *(i)* the vehicle model structure, which has been deeply analyzed in the first part of this work, *(ii)* the type of available sensors and *(iii)* the actuator dynamics. First the drag coefficients are evaluated by constant speed tests and afterwards with the aid of their knowledge a sub-optimal sinusoidal input thrust is designed in order to identify the inertia parameters. Extensive experimental activity on the ROMEO ROV of CNR-IAN has shown the effectiveness of such approach. Moreover it has been shown that the standard unmanned underwater vehicle models may need, as for the ROMEO ROV, to take into account propeller-propeller and propeller-hull interactions that have a most relevant influence on the system dynamics (up to 50% of efficiency loss in the applied thrust with respect to the nominal model). It has been shown that such phenomena can be correctly modelled by an efficiency parameter and experimental results concerning its identification on a real system have been extensively analyzed. The parameter estimated variances are generally relatively low, specially for the drag coefficients, confirming the effectiveness of the adopted identification scheme. The surge drag coefficients have been estimated relatively to two different vehicle payload configurations, i.e. carrying a plankton sampling device or a Doppler velocimeter (see chapter 4 for details), and the results show that in the considered surge velocity range ($|u| < 1m/s$) the drag coefficients are different, but perhaps less then expected. Moreover it has been shown that in the usual operating yaw rate range ($|\dot{\psi}| < 10 \deg/s$) drag is better modeled by a simple linear term rather then both a linear and a quadratic one. This is interesting as it suggests that the control system of the yaw axis of slow motion open frame ROV can be realized by standard linear control techniques. For a detailed description of the identification procedure and of the identification results of the ROMEO ROV consult chapter 4.

In the last part of this thesis the issue of planar motion control of a nonholonomic vehicle has been addressed. Inspired by the previous works of Casalino et al.[1] and Aicardi et al.[2] regarding a unicycle like kinematic model, a novel globally asymptotically convergent smooth feedback control law for the point stabilization of a car-like robot has been developed. The resulting linear velocity does not change sign, curvature is bounded and the target is asymptotically approached on a straight line. Applications to the control of underwater vehicles are discussed and extensive simulations are performed in order to analyze the algorithms behaviour with respect to actuator saturation. It is analytically shown that convergence is achieved also in presence of actuator satu-

ration and simulations are performed to evaluate the control law performance with and without actuator saturation. Moreover the generation of smooth paths having minimum square curvature, integrated over length, is addressed and solved with variational calculus in $3D$ for an arbitrary curve parametrization. The plane projection of such paths are shown to be least yaw drag energy paths for the $2D$ underwater motion of rigid bodies.

Chapter 1
Introduction

The scope of this chapter is to describe the motivations and objectives of this work.

1.1 Motivations and Objectives

Underwater robotics applications have extensively grown in the last twenty years both for scientific investigations and industrial needs. Technological improvements in the design and development of the mechanics and electronics of the systems have been followed by the development of very efficient and elaborate control strategies. Indeed the framework of underwater robotics is challenging form both a theoretical and experimental point of view. From a robotics perspective the challenge consists in dealing with an unknown parameter, highly nonlinear and coupled plant affected by non predictable noise, e.g. currents, with only partial state feedback provided by noisy and low sampling frequency sensors. This setting affects not only the *control* system synthesis, but also the *navigation* and *guidance* ones. Following [3], the navigation system is defined to be a velocity and position estimation module, the guidance system is a subsystem required to perform navigation system and, eventually, inertial reference trajectory data processing to compute local velocity and/or position references and the control system is a subsystem that takes care of generating the actuator inputs on the basis of the guidance system output. Within the classical control literature the above three subsystems are, roughly speaking, equivalent to the sensing system, the reference generator, sometimes called high level control, and the compensator (low level control).

The interest of the theoretical control system community towards underwater robotics is confirmed by the large and growing number of scientific publications and conferences touching every branch of the field. This research activity has made the state of the art in the navigation, control and guidance of underwater systems wide and variegate. As far as the control synthesis problem is concerned, all sorts of approaches have been analyzed: optimal control, adaptive control, sliding mode control, feedback linearization based control, Lyapunov based robust control, gain scheduling control, neurofuzzy and neural control. Sliding mode control for robust underwater vehicle trajectory tracking has been first proposed by the pioneer work of Yoerger and Slotine [4] in 1985. Since then many other contributions based on sliding mode control theory applied to the control of unmanned underwater vehicles (UUVs) have been proposed: among the many others, Cristi et al.[5] have reported and adaptive sliding mode approach combined with a state observer algorithm, Healey et al.[6] have discussed a multivariable sliding mode technique based on state variable errors, rather then output errors as accounted in [5], da Cunha et al.[7] have proposed a variable structure algorithm requiring only position measurements, Corradini et al.[8] have discussed a MIMO (multi input multi output)

discrete time variable structure approach and Bartolini et al.[9] have suggested a second order sliding mode technique. Also adaptive control approaches for the control of UUVs have been analyzed as shown, for example, in the works of Fossen et al.[10] [11], Ramadorai et al.[12], Sagatun et al.[13] and Yuh [14]. Examples of Lyapunov based and H_∞ robust control approaches for the synthesis of underwater vehicle control systems are given by Conte et al.[15] [16] [17], while examples of the use of neural net and neurofuzzy techniques for the control of underwater vehicles are given by the works of J. Yuh[18] [19] and of Craven et al.[20]. A similarly broad range of techniques have been proposed for the synthesis of control systems for mobile base underwater manipulators. This topic is very interesting as the hydrodynamic interactions between the manipulator and the fluid may induce relevant forces on the manipulator base that should be taken into account by the system model, rather then considered external disturbances, in order to achieve satisfactory control performance. In particular, the problem of coordinated manipulator-vehicle modelling and control has been addressed, e.g., by Mahesh et al.[21], Schjølberg et al.[22], McMillan et al.[23], Tarn et al.[24], McLain et al.[25], Dunnigan et al.[26] and Canudas de Wit et al.[27].

Each of the above reported control approaches for either vehicles, manipulators or combined vehicle-manipulators systems require at some stage the knowledge of the system model and parameters. Each of the above approaches is at some extent capable of dealing with model uncertainties and system noise, but each of them necessarily needs the knowledge of a fully identified, perhaps simplified, *nominal* model. Each of the above reported control approaches increases its performance as the model uncertainty is reduced. These may seem obvious considerations that apply to any robotic system, not only to underwater ones. Indeed if complex land or space robots, e.g. manipulators, need to be identified experimentally in order to develop a reliable dynamic model, the urge for system identification applied to underwater systems is even higher as for the great majority of underwater robots model parameters can not be estimated *a priori* on the basis of geometrical or structural information. The point is that given an underwater bluff body system of known geometry, what will be its drag coefficients or its inertia parameters? There is no reliable method of answering this question without experimental data. As far as underwater vehicles are concerned, experimental data for identification can be collected either in towing tank facilities or with on board sensors. The first method relies on consolidated naval engineering methodology and is more precise but complex, lengthy and expensive. As underwater vehicles configuration is time and mission dependent, system identification by means of on board sensors is certainly more appealing being faster, cheaper and easier to be repeated for different configurations when necessary.

Another important motivation for the analysis of underwater system modelling and identification is related to state and, eventually, environment estimation problem. As pointed out at the beginning of the above discussion, underwater systems sensors generally have a low sampling rate frequency (typically less then $5Hz$ for sonar profilers and Doppler effect velocimeters) and do not provide full state feedback as not all the

degrees of freedom are measured. The angular positions and, eventually, velocities are measured by inertial devices and a compass for yaw, while position with respect to the environment is measured by means of acoustic devices as long base line (LBL) or ultra short base line (USBL) positioning systems, or by sonar profilers. If velocity measurements are absent state estimation techniques as Kalman filters (KF) or extended Kalman filters (EKF) are generally adopted for velocity estimation. Indeed within this framework the need of an identified system model is related not only to control system design as discussed above, but also to the navigation one. Examples of dynamic model based navigation and motion estimation filters are given by the works of Caccia et al.[28] [29] [30] and Smith et al.[31]. The use of a correctly identified and reliable model to design dynamic filters for state estimation indirectly affects also the control system performance if the control strategy uses the estimated state as feedback. These considerations have motivated the majority of the work presented in this thesis: the development of a physical based model and its on board sensor based identification strategy for an open frame ROV. The proposed approach has been tested on the ROMEO ROV of the Institute for Naval Automation of the Italian National Research Council CNR-IAN and the experimental results are reported in this work. The proposed model is based on the classical Newton Euler unmanned underwater vehicle model presented, among others, by Yuh [14] and Fossen [32]. It is experimentally shown that such models may need to be extended in order to take into account propeller propeller, propeller hull and momentum drag interactions that are usually neglected. A two step procedure is proposed for the identification of a simplified model of the vehicles model: first the drag coefficients are estimated by constant velocity tests, then the drag coefficients values are adopted to design a suboptimal experiment for the identification of the inertia parameters.

Given the vehicles model, the motion control problem is addressed in the last part of this research and a novel algorithm for nonholonomic vehicle control taking into account the paths curvature is proposed in the last part of this work.

1.2 Outline of the work

The first chapter is mainly devoted to the discussion of the motivations and objectives of this research. In chapters 2 the adopted vector notation and some general (classical) kinematic results are presented, while in chapter 3 the dynamics of a rigid body in a fluid media is described within a Newton Euler formulation and the general equations of motion of an underwater vehicle are derived and discussed in detail. General considerations regarding underwater manipulators are also briefly addressed. Chapter 4 is devoted to the presentation of the proposed identification scheme, within the setting of classical least squares (LS) approach, and of the experimental results. At last Chapter 5 addresses the issue of nonholonomic vehicle motion control with reference to the case of underwater vehicles. Some original results regarding possible navigation solutions are presented.

1.3 Acknowledgments

The research activity described in this work has been supported by the Institute for Naval Automation CNR-IAN of the Italian National Research Council. The author is grateful to the Director of the CNR-IAN and to the whole staff of the IAN Robotics Department. Most of the experimental data analyzed in this work has been collected during late evening sessions in the summer of 1998 realized thanks to the work of the whole staff of the IAN Robotics Department.

In particular the author wishes to gratefully acknowledge Massimo Caccia of CNR-IAN and the research staff of the GRAAL laboratory of DIST, University of Genoa, for helpful discussions and suggestions.

Chapter 2
Kinematics

The scope of this chapter is to introduce the adopted notation and to review some basic concepts of kinematics that will be employed.

2.1 Vectors

2.1.1 Vector notation

Free vectors will be denoted with bold characters and no particular superscript or subscript, e.g. $\mathbf{a}$, while geometric vectors, i.e. vectors projected on a specific reference frame, will be bold variables having a left hand side superscript denoting the reference frame, e.g. ${}^{i}\mathbf{a}$. The position vector $\mathbf{r}_{q,p}$ of point p with respect to point q will be written, according to Grassman's notation, as $\mathbf{r}_{q,p} = p - q$, so if O_i and O_j are the origins of reference frames $< i >$ and $< j >$ then $\mathbf{r}_{i,j} = O_j - O_i$ will denote O_js position with respect to O_i. The projection of $\mathbf{r}_{i,j}$ on reference $< n >$ is ${}^{n}\mathbf{r}_{i,j} = (\mathbf{r}_{i,j})_x\mathbf{e}_1 + (\mathbf{r}_{i,j})_y\mathbf{e}_2 + (\mathbf{r}_{i,j})_z\mathbf{e}_3 = \sum_{h=1}^{3}(\mathbf{r}_{i,j})_h\mathbf{e}_h$ being $(\mathbf{e}_1, \mathbf{e}_2, \mathbf{e}_3)$ an orthonormal basis of $< n >$.

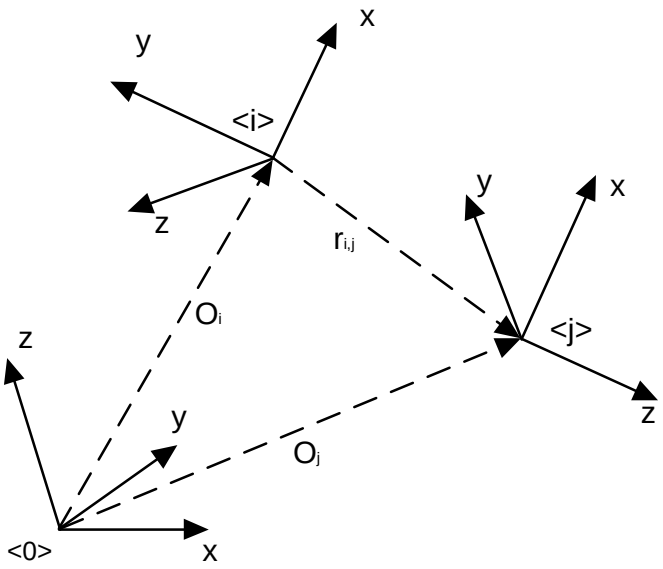

2.1.2 Time derivatives of vectors

The majority of books on Robotics start with a note on reference frames, rotations and homogenous transformations. Indeed these concepts are the basis of kinematics and rely on the idea of time derivative of a vector. This is a tricky topic that is worthwhile discussing in some detail as a starting point. The building block of classical mechanics is the concept of *event*. This is the mathematical abstraction of a primitive idea that can be defined only heuristically as the limit for null time duration and space occupation of a certain physical phenomenon as viewed by an observer. The set of all events is said *space-time*, denoted by V_4 that can be identified with the Cartesian product $E_3 \times \Re$ being E_3 the $3D$ Euclidean space and $\Re$ the set of real numbers. The evolution of a material point can be described by a continuous curve (*line of universe)* in V_4 made by the sequence it's events. Given the line of universe *absolute time* can be unambiguously defined through the following:

Axiom of Absolute Time Given two events $a, b \in V_4$ their time separation $\Delta t(a, b)$ is unambiguously defined for every observer as a continuous function $\Delta t : V_4 \times V_4 \rightarrow \Re$ satisfying

$$\Delta t(a, a) = 0$$
$$\Delta t(a, b) + \Delta t(b, c) = \Delta t(a, c) \; \forall \; a, b, c \in V_4$$

so that chosen a reference event 0 the absolute time can be defined as the continuous function $t : V_4 \rightarrow \Re, \; t(a) \triangleq \Delta t(0, a)$. According to the properties of Δt and to the definition of $t(a)$ it follows that $\Delta t(a, b) = t(b) - t(a)$ showing the independence of Δt from the reference event. Events a and b are said to be *simultaneous* if and only if $\Delta t(a, b) = 0$.

As a consequence of the above axiom given $a \in V_4$ the equation $t = t(a)$ defines a $3D$ hyperplane Σ_t (*hyperplane of simultaneity*) subset of V_4 made of all and only the simultaneous events of a. At each fixed instant t, Σ_t can be identified with the physical space at time t, common to every observer. In particular the following axiom is assumed to hold:

Axiom of Absolute Space Each hyperplane Σ_t for a fixed $t \in \Re$, is a $3D$ space having intrinsic Euclidean structure, i.e., in every hyperplane Σ_t a Euclidean distance is defined and all axioms and theorems of Euclidean geometry hold.

It follows that every geometric result at each fixed instant has an absolute character, i.e., is independent from the observer: for example calling $V_3(\Sigma_t)$ the set of all geometric vectors at instant t the time dependent vector $\mathbf{u}(t)$ is defined as $\mathbf{u}(t) : \Re \rightarrow V_3(\Sigma_t)$ and is an absolute quantity. Notice, however, that at each instant $t_i \neq t_j$ $\mathbf{u}(t_i)$ and $\mathbf{u}(t_j)$ are elements of different spaces as Σ_{t_i} and Σ_{t_j} are not only different, but disjoint. As a matter of fact the absolute time and space axioms do not specify what is meant by a fixed point at different times and thus the same concept of movement can not be defined. In particular as $\mathbf{u}(t_i) \in V_3(\Sigma_{t_i})$ and $\mathbf{u}(t_j) \in V_3(\Sigma_{t_j})$ with $V_3(\Sigma_{t_i}) \neq V_3(\Sigma_{t_j})$

vectors $\mathbf{u}(t_i)$ and $\mathbf{u}(t_j)$ can't be compared and the incremental ratio $\frac{\mathbf{u}(t+\Delta t)-\mathbf{u}(t)}{\Delta t}$ has no meaning whatsoever. It follows that even if the concept of vector as a function of time is well posed and has an absolute meaning, it is impossible to formally introduce the time derivative of a vector on the only basis of the axioms of absolute time and space. So, as the concept of event has an absolute meaning, the one of movement and time derivative of a vector is intrinsically relative, it can not even be formally defined prior to the introduction of the concepts of *reference space* and *reference frame*. Each observer maps the space-time set V_4 in it's own distinct $3D$ Euclidean *reference space* Γ_3 with a mapping function $\pi : V_4 \rightarrow \Gamma_3$ that, according to the axiom of absolute space, must have an invertible and isometric restriction on each Σ_t; that is $\pi|_{\Sigma_t} : \Sigma_t \rightarrow \Gamma_3$ is invertible and isometric so that at each instant every observer has it's own, but coherent to all the other observers, view of the common absolute space. Given an observer 0 and it's reference space Γ_3, it's *reference frame* $< 0 >$ is an orthonormal set of 3 constant vectors in $V(\Gamma_3)$, being $V(\Gamma_3)$ the set of all geometric vectors in Γ_3. Notice that constant vectors in reference $< 0 >$ are generally time dependent as viewed by a different observer as each observer has it's own mapping π. This is the reason why time derivatives of vectors are relative to a specific observer and not absolute quantities. In particular calling $(\mathbf{e}_1, \mathbf{e}_2, \mathbf{e}_3)$ the unit vector of reference $< 0 >$ each time dependent vector in $V(\Gamma_3)$ can be thought of as ${}^0\mathbf{u}(t) = \sum_{i=1}^3 u_i(t)\, \mathbf{e}_i$ and the time derivative of $\mathbf{u}$ with respect to reference $< 0 >$ is $\frac{d_{<0>}}{dt}\, {}^0\mathbf{u}(t) = \sum_{i=1}^3 \dot{u}_i(t)\, \mathbf{e}_i$ where the dot indicates the usual observer independent time derivative of a scalar function, $\dot{u}(t) \triangleq \frac{d}{dt}u(t)$. In the view of a different moving observer, say 1, the vectors $(\mathbf{e}_1, \mathbf{e}_2, \mathbf{e}_3)$ may not be constant with respect to his reference frame $< 1 >$, so the time derivative of $\mathbf{u}$ with respect to $< 1 >$ is $\frac{d_{<1>}}{dt}\, {}^1\mathbf{u}(t) = \sum_{i=1}^3 (\dot{u}_i(t)\, \mathbf{e}_i + u_i(t)\, \frac{d_{<1>}}{dt}\mathbf{e}_i)$. To better understand the nature of the term $\frac{d_{<1>}}{dt}\mathbf{e}_i$ remember that each mapping π must be isometric and invertible, so that orthonormality among vectors is observer independent. This fact is at the basis of *Poisson' s Formula*.

Poisson Formula Having noticed that orthonormal vectors in a reference frame must be viewed as orthonormal in each other, and indicating with $(\mathbf{e}_1, \mathbf{e}_2, \mathbf{e}_3)$ an orthonormal set of vectors fixed to reference $< 0 >$, the following holds:

$$\frac{d_{<1>}}{dt}(\mathbf{e}_i \cdot \mathbf{e}_j) = \left(\frac{d_{<1>}}{dt}\mathbf{e}_i\right) \cdot \mathbf{e}_j + \mathbf{e}_i \cdot \left(\frac{d_{<1>}}{dt}\mathbf{e}_j\right) = \dot{\mathbf{e}}_i \cdot \mathbf{e}_j + \mathbf{e}_i \cdot \dot{\mathbf{e}}_j = 0 \qquad (2.1)$$

where $\dot{\mathbf{e}}_i \triangleq \frac{d_{<1>}}{dt}\mathbf{e}_i$. Next the time dependent $\boldsymbol{\omega}_{0/1}(t)$ vector is defined as

$$\begin{cases} \boldsymbol{\omega}_{0/1}(t) \triangleq \dfrac{1}{2}\displaystyle\sum_{h=1}^{3} \mathbf{e}_h \wedge \dot{\mathbf{e}}_h \\ \dot{\mathbf{e}}_i \triangleq \dfrac{d_{<1>}}{dt}\mathbf{e}_i \\ \mathbf{e}_h : h = 1, 2, 3 \text{ orthonormal basis of reference } < 0 > \end{cases} \qquad (2.2)$$

being $\wedge$ the vector product. Remembering that for any three vectors $\mathbf{a}, \mathbf{b}, \mathbf{c}$

$$\mathbf{a} \wedge (\mathbf{b} \wedge \mathbf{c}) = \mathbf{b}(\mathbf{a} \cdot \mathbf{c}) - \mathbf{c}(\mathbf{a} \cdot \mathbf{b}) \tag{2.3}$$

being $\cdot$ the scalar product, the following is calculated

$$\begin{aligned} \boldsymbol{\omega}_{0/1} \wedge \mathbf{e}_i &= -\frac{1}{2}\sum_{h=1}^{3}\left[\mathbf{e}_i \wedge (\mathbf{e}_h \wedge \dot{\mathbf{e}}_h)\right] = -\frac{1}{2}\sum_{h=1}^{3}\left[\mathbf{e}_h\left(\mathbf{e}_i \cdot \dot{\mathbf{e}}_h\right) - \dot{\mathbf{e}}_h\left(\mathbf{e}_i \cdot \mathbf{e}_h\right)\right] = \\ &= +\frac{1}{2}\sum_{h=1}^{3}\left[\mathbf{e}_h\left(\dot{\mathbf{e}}_i \cdot \mathbf{e}_h\right) + \dot{\mathbf{e}}_h\,\delta_{ih}\right] = \dot{\mathbf{e}}_i \end{aligned} \tag{2.4}$$

where δ_{ih} is the Kronecker symbol and the substitution $\mathbf{e}_h\left(\dot{\mathbf{e}}_i \cdot \mathbf{e}_h\right) = -\mathbf{e}_h\left(\mathbf{e}_i \cdot \dot{\mathbf{e}}_h\right)$ is possible due to equation (2.1). The equation

$$\frac{d_{<1>}}{dt}\,\mathbf{e}_i \triangleq \dot{\mathbf{e}}_i = \boldsymbol{\omega}_{0/1} \wedge \mathbf{e}_i \tag{2.5}$$

is known as Poisson's equation and allows to express the time derivative of a vector with respect to a given reference in terms of it's derivative with respect to a different reference. To stress it's physical meaning, the angular velocity vector $\boldsymbol{\omega}$ of reference $< 0 >$ with respect to the fixed reference $< 1 >$ will be denoted as $\boldsymbol{\omega}_{0/1}$. Equation (2.2) can not be considered a *definition* of angular velocity, but rather the mathematical demonstration of the existence of a free vector $\boldsymbol{\omega}$ that depends on the only relative motions of two given frames and allows to calculate the time derivative of a vector with respect to a reference as a function of the time derivative of the same vector with respect to the other reference. Remembering that $(\mathbf{e}_1, \mathbf{e}_2, \mathbf{e}_3)$ are an orthonormal set of vectors fixed to reference $< 0 >$, the time derivative of a vector with respect to a given reference $< 1 >$ will be:

$$\begin{aligned} \frac{d_{<1>}}{dt}\,\boldsymbol{\rho} &= \frac{d_{<1>}}{dt}\,{}^{0}\boldsymbol{\rho} = \frac{d_{<1>}}{dt}\,\left(\sum_{i=1}^{3}\rho_i \mathbf{e}_i\right) = \\ &= \sum_{i=1}^{3}\left(\frac{d_{<1>}}{dt}\,\rho_i\right)\mathbf{e}_i + \sum_{i=1}^{3}\left(\frac{d_{<1>}}{dt}\mathbf{e}_i\right)\rho_i = \\ &= \frac{d_{<0>}}{dt}\,{}^{0}\boldsymbol{\rho} + \boldsymbol{\omega}_{0/1} \wedge\, {}^{0}\boldsymbol{\rho} \qquad \Rightarrow \\ \Rightarrow\ \frac{d_{<1>}}{dt}\,\boldsymbol{\rho} &= \frac{d_{<0>}}{dt}\,\boldsymbol{\rho} + \boldsymbol{\omega}_{0/1} \wedge\, \boldsymbol{\rho} \end{aligned} \tag{2.6, 2.7}$$

In the above calculations $\sum_{i=1}^{3}\left(\frac{d_{<1>}}{dt}\,\rho_i\right)\mathbf{e}_i$ has been replaced by $\frac{d_{<0>}}{dt}\,{}^{0}\boldsymbol{\rho}$ because by definition a scalar ρ is invariant for rotations, i.e. $\frac{d_{<i>}}{dt}\rho = \frac{d_{<j>}}{dt}\rho\ \forall\ < i >, < j >$. Notice that in (2.6) and (2.7) the geometric vector ${}^{0}\boldsymbol{\rho}$ has been replaced by the free vector

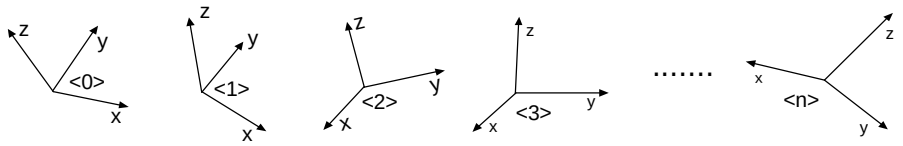

2.1.Kinematic chain

$\boldsymbol{\rho}$ as the time derivative of a vector depends on the reference in which it is evaluated but not on the frame eventually used to represent the vector itself. From equation (2.7) some properties of angular velocity can be deduced:

$$\frac{d_{<1>}}{dt}\,\boldsymbol{\omega}_{1/0} = \frac{d_{<0>}}{dt}\,\boldsymbol{\omega}_{1/0} \tag{2.8}$$

$$\boldsymbol{\omega}_{1/0} = -\boldsymbol{\omega}_{0/1} \tag{2.9}$$

$$\boldsymbol{\omega}_{j/j} = 0 \tag{2.10}$$

$$\boldsymbol{\omega}_{c/a} = \boldsymbol{\omega}_{c/b} + \boldsymbol{\omega}_{b/a} \tag{2.11}$$

where the last one follows from

$$\frac{d_{<a>}}{dt}\,\boldsymbol{\rho} = \frac{d_{<b>}}{dt}\,\boldsymbol{\rho} + \boldsymbol{\omega}_{b/a} \wedge\ \boldsymbol{\rho} \tag{2.12}$$

$$\frac{d_{<b>}}{dt}\,\boldsymbol{\rho} = \frac{d_{<c>}}{dt}\,\boldsymbol{\rho} + \boldsymbol{\omega}_{c/b} \wedge\ \boldsymbol{\rho} \tag{2.13}$$

$$\frac{d_{<a>}}{dt}\,\boldsymbol{\rho} = \frac{d_{<c>}}{dt}\,\boldsymbol{\rho} + \boldsymbol{\omega}_{c/a} \wedge\ \boldsymbol{\rho} \tag{2.14}$$

the substitution of (2.13) and (2.14) in (2.12).

Velocity composition rules Equations (2.7) and (2.11) can be used to calculate the relationship among the linear and angular velocities of a chain of n reference frames. From equation (2.11) follows

$$\boldsymbol{\omega}_{n/0} = \sum_{i=1}^{n} \boldsymbol{\omega}_{i/i-1} \tag{2.15}$$

As far as the linear velocity is concerned the linear velocity vector $\mathbf{v}_{i/j}$ of frame $< i >$ with respect to frame $< j >$ is defined as:

$$\mathbf{v}_{i/j} \triangleq \frac{d_{<j>}}{dt}\,(O_i - O_j) \tag{2.16}$$

so that

$$\begin{aligned}
\mathbf{v}_{i/0} &= \frac{d_{<0>}}{dt}(O_i - O_0) = \frac{d_{<0>}}{dt}(O_i - O_{i-1}) + \frac{d_{<0>}}{dt}(O_{i-1} - O_0) = \\
&= \frac{d_{<i-1>}}{dt}(O_i - O_{i-1}) + \boldsymbol{\omega}_{i-1/0} \wedge (O_i - O_{i-1}) + \mathbf{v}_{i-1/0} \qquad \Rightarrow \\
\mathbf{v}_{i/0} &= \mathbf{v}_{i/i-1} + \boldsymbol{\omega}_{i-1/0} \wedge \mathbf{r}_{i-1,i} + \mathbf{v}_{i-1/0} \qquad (2.17)
\end{aligned}$$

From equation (2.17) follows:

$$\begin{aligned}
\mathbf{v}_{n/0} + \sum_{i=1}^{n} \mathbf{v}_{i/0} &= \sum_{i=1}^{n} \mathbf{v}_{i/i-1} + \sum_{i=1}^{n} (\boldsymbol{\omega}_{i-1/0} \wedge \mathbf{r}_{i-1,i}) + \sum_{i=1}^{n} \mathbf{v}_{i-1/0} + \mathbf{v}_{n/0} \Rightarrow \\
\mathbf{v}_{n/0} &= \sum_{i=1}^{n} \mathbf{v}_{i/i-1} + \sum_{i=1}^{n} (\boldsymbol{\omega}_{i-1/0} \wedge \mathbf{r}_{i-1,i}) \qquad (2.18)
\end{aligned}$$

as $\sum_{i=1}^{n} \mathbf{v}_{i/0} = \sum_{i=1}^{n} \mathbf{v}_{i-1/0} + \mathbf{v}_{n/0}$. To understand the nature of the second sum on the right hand side of equation (2.18) notice that

$$\begin{aligned}
&\sum_{i=1}^{n} (\boldsymbol{\omega}_{i-1/0} \wedge \mathbf{r}_{i-1,i}) = \boldsymbol{\omega}_{0/0} \wedge \mathbf{r}_{0,1} + \boldsymbol{\omega}_{1/0} \wedge \mathbf{r}_{1,2} + \boldsymbol{\omega}_{2/0} \wedge \mathbf{r}_{2,3} + \boldsymbol{\omega}_{3/0} \wedge \mathbf{r}_{3,4} + \cdots = \\
&= \boldsymbol{\omega}_{1/0} \wedge \mathbf{r}_{1,2} + \left[(\boldsymbol{\omega}_{2/1} + \boldsymbol{\omega}_{1/0}) \wedge \mathbf{r}_{2,3} \right] + \left[(\boldsymbol{\omega}_{3/2} + \boldsymbol{\omega}_{2/1} + \boldsymbol{\omega}_{1/0}) \wedge \mathbf{r}_{3,4} \right] + \cdots = \\
&= \boldsymbol{\omega}_{1/0} \wedge (\mathbf{r}_{1,2} + \mathbf{r}_{2,3} + \mathbf{r}_{3,4} + \cdots) + \boldsymbol{\omega}_{2/1} \wedge (\mathbf{r}_{2,3} + \mathbf{r}_{3,4} + \mathbf{r}_{4,5} + \cdots) + \cdots = \\
&= \boldsymbol{\omega}_{1/0} \wedge \mathbf{r}_{1,n} + \boldsymbol{\omega}_{2/1} \wedge \mathbf{r}_{2,n} + \boldsymbol{\omega}_{3/2} \wedge \mathbf{r}_{3,n} + \cdots \qquad \Rightarrow \\
&\sum_{i=1}^{n} (\boldsymbol{\omega}_{i-1/0} \wedge \mathbf{r}_{i-1,i}) = \sum_{i=1}^{n} (\boldsymbol{\omega}_{i/i-1} \wedge \mathbf{r}_{i,n}) \qquad (2.19)
\end{aligned}$$

Replacing equation (2.19) in (2.18) the linear velocity of the n-th frame of a kinematic chain is calculated as a function of the relative velocities of each other frame with respect to the previous one, i.e.:

$$\mathbf{v}_{n/0} = \sum_{i=1}^{n} (\mathbf{v}_{i/i-1} + \boldsymbol{\omega}_{i/i-1} \wedge \mathbf{r}_{i,n}) \qquad (2.20)$$

Considering the special case $n = 2$ both, the rigid body velocity composition rule, and the Galilean velocity composition rule can be deduced from (2.20). By direct calculation

$$\mathbf{v}_{2/0} = \mathbf{v}_{1/0} + \mathbf{v}_{2/1} + \boldsymbol{\omega}_{1/0} \wedge \mathbf{r}_{1,2}$$

so that if the origin of the third frame is called p instead then O_2 follows

$$\mathbf{v}_{p/0} = \mathbf{v}_{1/0} + \mathbf{v}_{p/1} + \boldsymbol{\omega}_{1/0} \wedge \mathbf{r}_{1,p} \qquad (2.21)$$

with obvious meaning of notation. The relative velocity $\mathbf{v}_{p/1}$of point p with respect to $O_1$is null if p and the frame $< 1 >$ are fixed to the same rigid body. Thus if $< 0 >$ is a fixed (*absolute*) reference and $< 1 >$ moves attached to a rigid body (*relative* reference), each point p of the rigid body will have absolute velocity

$$\mathbf{v}_{p/0} = \mathbf{v}_{1/0} + \boldsymbol{\omega}_{1/0} \wedge \mathbf{r}_{1,p} \tag{2.22}$$

being $\mathbf{r}_{p,1} = p - O_1$ the position vector of p respect to O_1 by definition. As far as the Galilean velocity composition rule is concerned, equation (2.21) can be written as

$$\begin{aligned} \mathbf{v}_{p/0} - \mathbf{v}_{1/0} &= \frac{d_{<0>}}{dt}\left(p - O_0 - O_1 + O_0\right) = \\ &= \frac{d_{<0>}}{dt}\mathbf{r}_{1,p} = \mathbf{v}_{p/1} + \boldsymbol{\omega}_{1/0} \wedge \mathbf{r}_{1,p} \qquad \Rightarrow \\ \frac{d_{<0>}}{dt}\mathbf{r}_{1,p} &= \frac{d_{<1>}}{dt}\mathbf{r}_{1,p} + \boldsymbol{\omega}_{1/0} \wedge \mathbf{r}_{1,p} \end{aligned} \tag{2.23}$$

which is the desired Galilean velocity composition rule equation.

2.1.3 On useful vector operations properties

As n-dimensional vector quantities are assumed to be elements of $\Re^{n\times 1}$ the scalar product operation introduced in (2.3) with the symbol $\cdot$ can be also thought of as a row by column product, i.e. $\mathbf{a} \cdot \mathbf{b} = \mathbf{a}^T\ \mathbf{b}\ \forall\ \mathbf{a}, \mathbf{b} \in \Re^{n\times 1}$. The vector product $\mathbf{a} \wedge \mathbf{b}$ can be thought of as

$$\mathbf{a} \wedge \mathbf{b} \triangleq [\mathbf{a}\wedge]\ \mathbf{b} \triangleq S(\mathbf{a})\ \mathbf{b} \triangleq \begin{pmatrix} 0 & -a_3 & a_2 \\ a_3 & 0 & -a_1 \\ -a_2 & a_1 & 0 \end{pmatrix} \begin{pmatrix} b_1 \\ b_2 \\ b_3 \end{pmatrix} \tag{2.24}$$

and more generally any skew-symmetric operator can be thought of as a vector product. This is an important property that may be worthwhile showing. Consider a generic skew-symmetric operator A: by definition of skew-symmetry given any vectors $\mathbf{u}$,$\mathbf{v}$ the following must hold $A(\mathbf{u}) \cdot \mathbf{v} = -\mathbf{u} \cdot A(\mathbf{v})$ which is equivalent to the statement that for any skew-symmetric operator A and any vector $\mathbf{v}$, $A(\mathbf{v}) \cdot \mathbf{v} = 0$. Given a generic skew-symmetric operator A and an othonormal basis $(\mathbf{e}_1, \mathbf{e}_2, \mathbf{e}_3)$, consider the vector $\mathbf{a} \triangleq \frac{1}{2}\sum_{i=1}^{3} \mathbf{e}_i \wedge A(\mathbf{e}_i)$ (*axis vector*) and the for any vector $\mathbf{v}$ the following holds:

$$\begin{aligned} \mathbf{a} \wedge \mathbf{v} &= \left(\frac{1}{2}\sum_{i=1}^{3} \mathbf{e}_i \wedge A(\mathbf{e}_i)\right) \wedge \mathbf{v} = \frac{1}{2}\sum_{i=1}^{3} \left(\left(\mathbf{v} \cdot \mathbf{e}_i\right) A(\mathbf{e}_i) - \left(A(\mathbf{e}_i) \cdot \mathbf{v}\right) \mathbf{e}_i\right) = \\ &= \frac{1}{2}\sum_{i=1}^{3} \left(v_i\, A(\mathbf{e}_i) + \left(A(\mathbf{v}) \cdot \mathbf{e}_i\right) \mathbf{e}_i\right) = A(\mathbf{v}) \end{aligned}$$

being $-A(\mathbf{e}_i)\cdot\mathbf{v} = A(\mathbf{v})\cdot\mathbf{e}_i$ by definition of skew-symmetry of A and $\sum_{i=1}^{3}(\mathbf{v}\cdot\mathbf{e}_i)\,A(\mathbf{e}_i) = \sum_{i=1}^{3} v_i\,A(\mathbf{e}_i) = \sum_{i=1}^{3} A(v_i\mathbf{e}_i) = A(\mathbf{v})$ by the linearity of A. Two simple consequences of the above result are

- $\mathbf{a}$ is unique (suppose $\mathbf{a}$, $\mathbf{b}$ such that $A(\mathbf{v}) = \mathbf{a}\wedge\mathbf{v} = \mathbf{b}\wedge\mathbf{v}$ then $(\mathbf{a}-\mathbf{b})\wedge\mathbf{v} = 0 \Rightarrow \mathbf{a} = \mathbf{b}$).
- A has only one real eigenvalue $\lambda = 0$ relative to the eigenvector $\mathbf{a}$.

A frequent kind of vector operation in kinematic and dynamic calculations is the double vector product (2.3) $\mathbf{a}\wedge(\mathbf{b}\wedge\mathbf{c})$ which is linear in each of the three vectors. Noting by direct calculation that for any three vectors $(\mathbf{a}\cdot\mathbf{b})\,\mathbf{c} = [\mathbf{c}\,\mathbf{a}^T]\,\mathbf{b}$ where

$$[\mathbf{c}\,\mathbf{a}^T] = \begin{pmatrix} c_1a_1 & c_1a_2 & c_1a_3 \\ c_2a_1 & c_2a_2 & c_2a_3 \\ c_3a_1 & c_3a_2 & c_3a_3 \end{pmatrix} \tag{2.25}$$

$[\mathbf{c}\,\mathbf{a}^T]$ is the *external vector product*, the double vector product (2.3) can be written as

$$\begin{aligned} \mathbf{a}\wedge(\mathbf{b}\wedge\mathbf{c}) &= \mathbf{b}(\mathbf{a}\cdot\mathbf{c}) - \mathbf{c}(\mathbf{a}\cdot\mathbf{b}) = \\ &= ([\mathbf{b}\,\mathbf{c}^T - \mathbf{c}\,\mathbf{b}^T])\,\mathbf{a} && (2.26)\\ &= (I_{3\times3}(\mathbf{a}\cdot\mathbf{c}) - [\mathbf{c}\,\mathbf{a}^T])\,\mathbf{b} && (2.27)\\ &= ([\mathbf{b}\,\mathbf{a}^T] - I_{3\times3}(\mathbf{a}\cdot\mathbf{b}))\,\mathbf{c} && (2.28) \end{aligned}$$

being $I_{3\times3}$ the 3×3 identical matrix.

Another useful result in vector analysis is *Helmholtz's theorem*: any finite, uniform, continuous and vanishing at infinity vector field $\mathbf{F}$ may be written as the sum of the gradient of a scalar φ and the curl of a zero divergence vector $\mathbf{a}$, i.e.[33]

$$\begin{aligned} \forall\,\mathbf{F} &\in \Re^{3\times1} \text{ uniform, finite and vanashing at infinite} \Rightarrow \\ \exists\,\varphi &\in \Re, \mathbf{a}\in\Re^{3\times1} \mid \mathbf{F} = \nabla\varphi + \nabla\wedge\mathbf{a}\ ,\ \nabla\cdot\mathbf{a} = 0 \end{aligned}$$

As the divergence of the rotor of any vector is identically null, from the above follows that the divergence of a vector field $\mathbf{F}$ satisfying the above hypothesis can be written as the laplacian of a scalar, i.e.

$$\nabla\cdot\mathbf{F} = \nabla\cdot(\nabla\varphi) + \nabla\cdot(\nabla\wedge\mathbf{a}) = \nabla^2\varphi$$

moreover if the rotor of $\mathbf{F}$ is null ($\mathbf{F}$ is *conservative*) then $\mathbf{a}$ itself is identically null [33]. These results are useful in the hydrodynamic theory of ideal fluids that will be discussed in the next chapter.

Chapter 3
Dynamics

Within this chapter the dynamics of a robotic structure will be revised and extended to a fluid environment. The Euler-Newton formulation will be adopted.

3.1 Rigid body Newton-Euler equations

With reference to figure (3.1) the Newton-Euler equations of motion of the rigid body will be outlined. Reference $< 0 >$ having origin in o is inertial, while reference $< 1 >$ having origin in u is fixed to the rigid body having center of mass in point c. Indicating with $\rho(\mathbf{r})$ the density of the body, with m it's mass, with V it's volume, with $\mathbf{r}_{u,c} \triangleq (c-u)$ (Grassman's notation, see Chapter 2) the position of c with respect to u and with T it's kinetic energy the following hold by definition

$$m \triangleq \int_V \rho(\mathbf{r}_{u,p})\, dV \tag{3.1}$$

$$m\, \mathbf{r}_{u,c} \triangleq \int_V \rho(\mathbf{r}_{u,p}) \mathbf{r}_{u,p}\, dV \tag{3.2}$$

$$T \triangleq \frac{1}{2} \int_V \rho(\mathbf{r}_{o,p})\, \mathbf{v}_{p/o} \cdot \mathbf{v}_{p/o}\, dV \tag{3.3}$$

being p a generic point of the rigid body, dV an infinitesimal volume element equal to $d^3(p-u)$ in (3.1) and (3.2) and to $d^3(p-o)$ in (3.3). According to equation (2.17) the velocity $\mathbf{v}_{p/o}$ of equation (3.3) can be written as

$$\begin{aligned} \mathbf{v}_{p/o} &= \frac{d_{<0>}}{dt}(p-o) = \frac{d_{<0>}}{dt}(p-c) + \frac{d_{<0>}}{dt}(c-o) = \\ &= \mathbf{v}_{p/c} + \boldsymbol{\omega}_{c/o} \wedge \mathbf{r}_{c,p} + \mathbf{v}_{c/o} \Rightarrow \\ \mathbf{v}_{p/o} &= \mathbf{v}_{c/o} + \boldsymbol{\omega}_{c/o} \wedge \mathbf{r}_{c,p} \end{aligned} \tag{3.4}$$

being $\mathbf{v}_{p/c} = \frac{d_{<1>}}{dt}(p-c) = 0 \ \ \forall\, p$ by definition of rigid body. Replacing equation (3.4) in (3.3) Köenig's theorem is derived:

$$\begin{aligned} T &= \frac{1}{2} \int_V \rho\ \mathbf{v}_{p/o} \cdot \mathbf{v}_{p/o}\, dV = \frac{1}{2} \int_V \rho\ \mathbf{v}_{c/o} \cdot \mathbf{v}_{c/o}\, dV + \\ &+ \frac{1}{2} \int_V \rho\ (\boldsymbol{\omega}_{c/o} \wedge \mathbf{r}_{c,p}) \cdot (\boldsymbol{\omega}_{c/o} \wedge \mathbf{r}_{c,p})\, dV = \\ &= \frac{1}{2}\, v_{c/o}^2 \int_V \rho\, dV + \frac{1}{2} \boldsymbol{\omega}_{c/o} \cdot \int_V \rho\, \mathbf{r}_{c,p} \wedge (\boldsymbol{\omega}_{c/o} \wedge \mathbf{r}_{c,p})\, dV \Rightarrow \end{aligned}$$

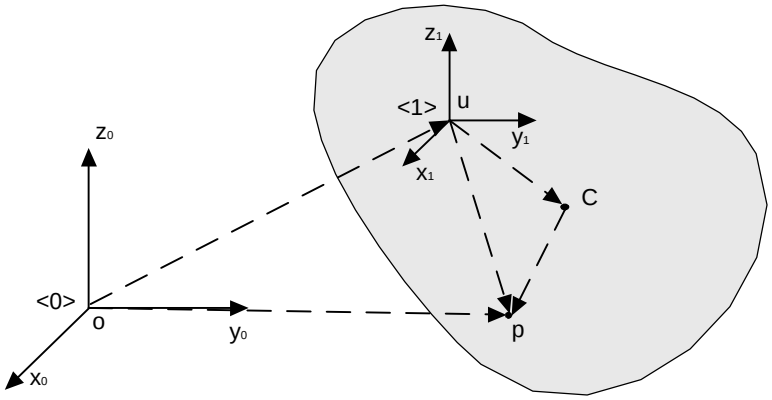

3.1.Rigid body, refer to text

$$T = \frac{1}{2} m\, v_{c/o}^2 + \frac{1}{2} \boldsymbol{\omega}_{c/o} \cdot I_c \boldsymbol{\omega}_{c/o} \tag{3.5}$$

where the inertia matrix operator I_c with respect to the center of mass has been introduced. By definition of inertia operator and remembering equations (2.26), (2.27) and (2.28) the inertia operator with respect an arbitrary point, e.g. u, is

$$\begin{aligned} I_u \boldsymbol{\omega} &\triangleq \int_V \rho\, \mathbf{r}_{u,p} \wedge (\boldsymbol{\omega} \wedge \mathbf{r}_{u,p})\, dV = \qquad (3.6) \\ &= \left(\int_V \rho\, [I_{3\times 3}(\mathbf{r}_{u,p} \cdot \mathbf{r}_{u,p}) - \mathbf{r}_{u,p}\mathbf{r}_{u,p}^T]\, dV \right) \boldsymbol{\omega} \Rightarrow \\ I_u &\triangleq \int_V \rho\, [I_{3\times 3}(\mathbf{r}_{u,p} \cdot \mathbf{r}_{u,p}) - \mathbf{r}_{u,p}\mathbf{r}_{u,p}^T]\, dV. \qquad (3.7) \end{aligned}$$

The inertia tensor thus defined is symmetric and positive definite. With reference to figure (3.1) notice that replacing $\mathbf{r}_{u,p} = \mathbf{r}_{c,p} - \mathbf{r}_{c,u}$ in equation (3.7) the *parallel axis theorem* is immediately derived, i.e.,

$$\begin{aligned} I_u = & \int_V \rho(\mathbf{r}_{u,p})\, [I_{3\times 3}(\mathbf{r}_{c,p} \cdot \mathbf{r}_{c,p}) - \mathbf{r}_{c,p}\mathbf{r}_{c,p}^T]\, dV + \\ & + \int_V \rho(\mathbf{r}_{u,p})\, [I_{3\times 3}(\mathbf{r}_{c,u} \cdot \mathbf{r}_{c,u}) - \mathbf{r}_{c,u}\mathbf{r}_{c,u}^T]\, dV + \end{aligned}$$

$$- \int_V \rho(\mathbf{r}_{u,p}) \left[I_{3\times 3}(2\, \mathbf{r}_{c,p} \cdot \mathbf{r}_{c,u}) - \mathbf{r}_{c,p}\mathbf{r}_{c,u}^T - \mathbf{r}_{c,u}\mathbf{r}_{c,p}^T \right] dV.$$

The first integral is just I_c, by definition, the second one is equal to $m \left[I_{3\times 3}(\mathbf{r}_{c,u} \cdot \mathbf{r}_{c,u}) - \mathbf{r}_{c,u}\mathbf{r}_{c,u}^T \right]$ being $\mathbf{r}_{u,c}$ constant, and the third one is null as by definition of center of mass c the following holds: $m\, \mathbf{r}_{c,c} \triangleq \int_V \rho(\mathbf{r}_{u,p})\, \mathbf{r}_{c,p}\, dV = 0$. Thus for any point u the parallel axis theorem states that

$$I_u = I_c + m \left[I_{3\times 3}(\mathbf{r}_{c,u} \cdot \mathbf{r}_{c,u}) - \mathbf{r}_{c,u}\mathbf{r}_{c,u}^T \right] \tag{3.8}$$

As the hydrodynamic forces applied on a body are usually derived with respect to the local reference frame, the standard Newton equations of a rigid body will be now calculated in reference $< 1 >$. With reference to equation (2.7) the absolute velocity of a generic point p of the rigid body in figure (3.1) is

$$\begin{aligned}
\mathbf{v}_{p/o} &= \frac{d_{<0>}}{dt}(p-o) = \frac{d_{<0>}}{dt}(u-o) + \frac{d_{<0>}}{dt}(p-u) = \\
&= \mathbf{v}_{u/o} + \frac{d_{<1>}}{dt}(p-u) + \boldsymbol{\omega}_{1/0} \wedge \mathbf{r}_{u,p} \Rightarrow \\
\mathbf{v}_{p/o} &= \mathbf{v}_{u/o} + \boldsymbol{\omega}_{1/0} \wedge \mathbf{r}_{u,p}
\end{aligned} \tag{3.9}$$

being $\frac{d_{<1>}}{dt}(p-u) = \frac{d_{<1>}}{dt}\mathbf{r}_{u,p} = 0$ by definition of rigid body. Notice that all involved vectors are free vectors although according to equation (2.7) the most "natural" reference frame where to project $\mathbf{v}_{u/o}$, $\boldsymbol{\omega}_{1/0}$ and $\mathbf{r}_{u,p}$ is the local reference $< 1 >$. The absolute acceleration will be:

$$\begin{aligned}
\mathbf{a}_{p/o} &= \frac{d_{<0>}}{dt}\mathbf{v}_{p/o} = \frac{d_{<1>}}{dt}\mathbf{v}_{p/o} + \boldsymbol{\omega}_{1/0} \wedge \mathbf{v}_{p/o} = \\
&= \frac{d_{<1>}}{dt}(\mathbf{v}_{u/o} + \boldsymbol{\omega}_{1/0} \wedge \mathbf{r}_{u,p}) + \boldsymbol{\omega}_{1/0} \wedge (\mathbf{v}_{u/o} + \boldsymbol{\omega}_{1/0} \wedge \mathbf{r}_{u,p}) \Rightarrow \\
\mathbf{a}_{p/o} &= \frac{d_{<1>}}{dt}\mathbf{v}_{u/o} + \left(\frac{d_{<1>}}{dt}\boldsymbol{\omega}_{1/0} \right) \wedge \mathbf{r}_{u,p} + \\
&\quad + \boldsymbol{\omega}_{1/0} \wedge \mathbf{v}_{u/o} + \boldsymbol{\omega}_{1/0} \wedge (\boldsymbol{\omega}_{1/0} \wedge \mathbf{r}_{u,p})
\end{aligned} \tag{3.10}$$

This equation can be used to calculate the Newton force equation

$$\frac{d_{<0>}}{dt} \int_V \rho(\mathbf{r}_{u,p}) \mathbf{v}_{p/o} dV = \sum_i \mathbf{F}_i^{external}$$

for a rigid body having a time invariant density, in the local reference. By direct calcu-

lation it follows that

$$m\left(\frac{d_{<1>}}{dt}\mathbf{v}_{u/o}+\left(\frac{d_{<1>}}{dt}\boldsymbol{\omega}_{1/0}\right)\wedge\mathbf{r}_{u,c}+\boldsymbol{\omega}_{1/0}\wedge\mathbf{v}_{u/o}+\boldsymbol{\omega}_{1/0}\wedge(\boldsymbol{\omega}_{1/0}\wedge\mathbf{r}_{u,c})\right)$$
$$=\sum_i\mathbf{F}_i^{external} \tag{3.11}$$

where m is the total time-constant mass of the body, $r_{u,c}$ its center of mass position relative to reference $<1>$ as given by equation (3.2), $\mathbf{v}_{u/o}$ is the absolute velocity of references $<1>$ origin u, $\boldsymbol{\omega}_{1/0}$ its absolute angular velocity and $\sum_i\mathbf{F}_i^{external}$ is the sum of all external forces applied on the body. Again notice that by construction the most natural reference frame where to project all the free vectors in equation (3.11) is $<1>$. In particular adopting the standard SNAME notation for marine systems the following hold:

$$\begin{aligned}
{}^1(\mathbf{v}_{u/o}) &= (u,v,w)^T\\
{}^1(\boldsymbol{\omega}_{1/0}) &= (p,q,r)^T\\
{}^1\left(\frac{d_{<1>}}{dt}\mathbf{v}_{u/o}\right) &= (du/dt,dv/dt,dw/dt)^T\\
{}^1\left(\frac{d_{<1>}}{dt}\boldsymbol{\omega}_{1/0}\right) &= (dp/dt,dq/dt,dr/dt)^T\\
u &= surge\\
v &= sway\\
w &= heave\\
p &= roll\\
q &= pitch\\
r &= yaw
\end{aligned}$$

The Newton equation for the rotational dynamics is related to the absolute angular momentum balance. In particular calling $\mathbf{N}_u$ the force moment about point u by definition the following holds:

$$\begin{aligned}
\sum_i\mathbf{N}_{u,i}^{external} &= \int_V(\mathbf{r}_{u,p}\wedge\frac{d_{<0>}}{dt}\mathbf{v}_{p/o})\rho(\mathbf{r}_{u,p})\,dV=\\
&= \int_V(\mathbf{r}_{u,p}\wedge\mathbf{a}_{p/o})\rho(\mathbf{r}_{u,p})\,dV
\end{aligned}\tag{3.12}$$

Substituting equation (3.10) in (3.12):

$$\int_V(\mathbf{r}_{u,p}\wedge\mathbf{a}_{p/o})\rho(\mathbf{r}_{u,p})\,dV=$$

$$
\begin{aligned}
&= \int_V \left(\mathbf{r}_{u,p} \wedge \left(\frac{d_{<1>}}{dt} \mathbf{v}_{u/o} + \boldsymbol{\omega}_{1/0} \wedge \mathbf{v}_{u/o} \right) \right) \rho(\mathbf{r}_{u,p})\, dV + \\
&+ \int_V \left(\mathbf{r}_{u,p} \wedge \left(\left(\frac{d_{<1>}}{dt} \boldsymbol{\omega}_{1/0} \right) \wedge \mathbf{r}_{u,p} \right) \right) \rho(\mathbf{r}_{u,p})\, dV + \\
&+ \int_V (\mathbf{r}_{u,p} \wedge (\boldsymbol{\omega}_{1/0} \wedge (\boldsymbol{\omega}_{1/0} \wedge \mathbf{r}_{u,p}))) \rho(\mathbf{r}_{u,p})\, dV = \sum_i \mathbf{N}_{u,i}^{external}
\end{aligned}
$$

where the integral in the second line is $m\, \mathbf{r}_{u,c} \wedge \left(\frac{d_{<1>}}{dt} \mathbf{v}_{u/o} + \boldsymbol{\omega}_{1/0} \wedge \mathbf{v}_{u/o} \right)$, the one in the third is $I_u \left(\frac{d_{<1>}}{dt} \boldsymbol{\omega}_{1/0} \right)$by equation (3.6), and the on in the fourth can be shown to be $\boldsymbol{\omega}_{1/0} \wedge I_u \boldsymbol{\omega}_{1/0}$ by some vector manipulations based on the properties shown in paragraph 2.1.3. The second Newton equation for a rigid body can be thus expressed in the local reference frame having origin in u, as

$$
\begin{aligned}
& I_u \left(\frac{d_{<1>}}{dt} \boldsymbol{\omega}_{1/0} \right) + \boldsymbol{\omega}_{1/0} \wedge I_u \boldsymbol{\omega}_{1/0} + m\, \mathbf{r}_{u,c} \wedge \left(\frac{d_{<1>}}{dt} \mathbf{v}_{u/o} + \boldsymbol{\omega}_{1/0} \wedge \mathbf{v}_{u/o} \right) \\
= & \sum_i \mathbf{N}_{u,i}^{external}
\end{aligned} \tag{3.13}
$$

Equations (3.11) and (3.13) can be written in matrix (space notation) form as:

$$
M\, \frac{d_{<1>}}{dt} \boldsymbol{\nu} + C(\boldsymbol{\omega}_{1/0})\, \boldsymbol{\nu} = \boldsymbol{\tau}^{ext} \tag{3.14}
$$

$$
\boldsymbol{\nu} = (\mathbf{v}_{u/o}^T, \boldsymbol{\omega}_{1/0}^T)^T \in \Re^{6\times 1} \tag{3.15}
$$

being $\boldsymbol{\nu}$ the generalized velocity, $M \in \Re^{6\times 6}$ the inertia operator, $C(\boldsymbol{\omega}) \in \Re^{6\times 6}$ the Coriolis and centripetal operator and $\boldsymbol{\tau}^{ext} = \sum_i (\mathbf{F}_i^T, \mathbf{N}_{u,i}^T)^{T\, external} \in \Re^{6\times 1}$ the generalized torque applied to the body. By direct calculation it can be shown that the inertia and Coriolis-centripetal operators are given by

$$
M \triangleq \begin{pmatrix} m\, I_{3\times 3} & -m\, S(\mathbf{r}_{u,c}) \\ m\, S(\mathbf{r}_{u,c}) & I_u \end{pmatrix} \tag{3.16}
$$

$$
C(\boldsymbol{\omega}_{1/0}) \triangleq \begin{pmatrix} m\, S(\boldsymbol{\omega}_{1/0}) & -m\, S(\boldsymbol{\omega}_{1/0})\, S(\mathbf{r}_{u,c}) \\ m\, S(\mathbf{r}_{u,c})\, S(\boldsymbol{\omega}_{1/0}) & -S(I_u \boldsymbol{\omega}_{1/0}) \end{pmatrix} \tag{3.17}
$$

being S the skew symmetric vector product operator defined by equation (2.24). It can be shown [32] that while the parametrization of the positive definite rigid body inertia matrix given in equation (3.16) is unique, the Coriolis-centripetal matrix can be parametrized in a non-unique skew symmetric form. The one given in equation (3.17) has the advantage of depending only on $\boldsymbol{\omega}_{1/0}$, but as shown in [32] other skew symmetric parametrizations depending on $\boldsymbol{\nu} = (\mathbf{v}_{u/o}^T, \boldsymbol{\omega}_{1/0}^T)^T$ are possible. To characterize the dynamics of a rigid body in a fluid environment the right hand side $\boldsymbol{\tau}^{ext}$ of equation (3.14) has to be calculated explicitly.

3.2 Fluid forces and moments on a rigid body

When a body moves in a fluid environment it experiences external forces due to the interaction between itself and the fluid. As can be imagined even intuitively, all these forces are somehow proportional to the fluids density and to the relative speed and acceleration between the body and the fluid. When a body moves in atmospheric air at low speeds, as for the majority of the robotic applications, these forces are negligeable. On the contrary in underwater applications, due to the high density of water, these forces are never negligeable even at the lowest speeds. The calculation of hydrodynamic generalized forces on a rigid body is a classical and well known topic in fluid dynamics theory that will thus be here only revised in view of the robotic applications of interest. For a more detailed discussion refer to [34] [35] [36].

3.2.1 The Navier Stokes equation

The Navier Stokes equation is the equation of motion of an infinitesimal volume of newtonian, incompressible and time-constant density fluid. To derive this equation the following notation will be used: ρ will denote the fluid density (dimensions $[Kg/m^3]$), $\mathbf{F}$ the force per unit volume (dimensions $[N/m^3]$), $\boldsymbol{\tau}_{ij}$ the stress tensor (dimensions $[N/m^2]$), p the pressure (dimensions $[N/m^2]$), V a volume element (dimensions $[m^3]$) of surface S (dimensions $[m^2]$) having unit normal vector $\mathbf{n} = (n_1, n_2, n_3)^T$ (dimensions $[m]$), $\mathbf{u} = (u_1, u_2, u_3)^T$ the fluids local velocity (dimensions $[m/s]$) with respect to an inertial frame. A preliminary result for the derivation of the Navier Stokes equation and other important fluid dynamic properties is the *transport theorem*. Given a differentiable function $f(\mathbf{x}, t)$, the quantity $I(t) = \int\int\int_{V(t)} f(\mathbf{x}, t) dV$ where $V(t)$ is a time evolving volume of surface $S(t)$ has time derivative

$$\frac{d}{dt} I(t) = \int\int\int_{V(t)} \frac{\partial}{\partial t} f(\mathbf{x}, t)\, dV + \int\int_{S(t)} f(\mathbf{x}, t) U_n\, dS \tag{3.18}$$

being U_n the normal velocity of S. An important special case of equation (3.18) is related to the situation where the volume $V(t)$ and the surface $S(t)$ are relative to the same fluid particles. In such situation $U_n \triangleq \mathbf{u}^T \mathbf{n} = u_i n_i$ (where repeated indexes are to be interpreted as summed) and by applying the Gauss theorem to the second integral on the right hand side of (3.18) the following holds

$$\frac{d}{dt} \int\int\int_{V(t)} f(\mathbf{x}, t)\, dV = \int\int\int_{V(t)} \left(\frac{\partial}{\partial t} f(\mathbf{x}, t) + \nabla \cdot f(\mathbf{x}, t) \mathbf{u} \right) dV \tag{3.19}$$

being $\nabla \triangleq (\partial/\partial x_1, \partial/\partial x_2, \partial/\partial x_3)^T$ the gradient operator. Substituting the fluid density ρ to the function f for a generic volume element in equation (3.19) the principle of

mass conservation implies $\int\int\int_{V(t)} \left(\frac{\partial}{\partial t}\rho(\mathbf{x},t) + \nabla\cdot\rho(\mathbf{x},t)\mathbf{u}\right) dV = 0$ and thus

$$\frac{\partial}{\partial t}\rho(\mathbf{x},t) + \nabla\cdot\rho(\mathbf{x},t)\mathbf{u} = 0 \tag{3.20}$$

for the arbitrary of V. If the fluid is assumed incompressible and of constant density in time it follows

$$\left.\begin{array}{l}\frac{\partial}{\partial t}\rho(\mathbf{x},t) = 0\\ \nabla\rho(\mathbf{x},t) = 0\end{array}\right\} \Rightarrow \nabla\cdot\mathbf{u} = \frac{\partial}{\partial x_j}u_j = 0 \tag{3.21}$$

Equation (3.19) can be applied to the momentum ρu_i conservation of a generic volume V of fluid yielding

$$\begin{aligned}\frac{d}{dt}\int\int\int_{V(t)} \rho u_i\, dV &= \int\int\int_{V(t)} \left(\frac{\partial}{\partial t}(\rho u_i) + \frac{\partial}{\partial x_j}(\rho u_i u_j)\right) dV = \\ &= \int\int\int_{V(t)} \left(\frac{\partial}{\partial x_j}\tau_{ij} + F_i\right) dV\end{aligned}$$

As the choice of V is arbitrary this last equation implies

$$\frac{\partial}{\partial t}(\rho u_i) + \frac{\partial}{\partial x_j}(\rho u_i u_j) = \frac{\partial}{\partial x_j}\tau_{ij} + F_i$$

which in the hypothesis stated in (3.21) implies the Euler's equation of an incompressible time-constant density fluid

$$\frac{\partial}{\partial t}u_i + u_j\frac{\partial}{\partial x_j}u_i = \frac{1}{\rho}\left(\frac{\partial}{\partial x_j}\tau_{ij} + F_i\right) \tag{3.22}$$

To finally derive the Navier Stokes equation some further hypothesis on the stress tensor $\boldsymbol{\tau}$ must be made. The balance of moments acting on a free element of fluid dV implies its symmetry, i.e., $\boldsymbol{\tau}_{ij} = \boldsymbol{\tau}_{ji}\ \forall\ ij$. Moreover it can be shown [34] that the most general form of stress tensor of an isotropic fluid satisfying (3.21) and whose volume element dV does not undergo deformation when moving as a rigid body, i.e. with a velocity $\mathbf{v} + \boldsymbol{\omega}\wedge\mathbf{r}$ being $\mathbf{v}$ and $\boldsymbol{\omega}$ constant, is

$$\tau_{ij} = -p\,\delta_{ij} + \mu\,(\partial u_i/\partial x_j + \partial u_j/\partial x_i)\ \forall\ i \neq j \tag{3.23}$$

being δ_{ij} the Kronecker delta symbol, p the pressure and μ the *viscous shear coefficient* (dimensions $[Kg/ms]$). Equation (3.23) defines a *newtonian* fluid; notice that the vast majority of fluids, including air and water, indeed exhibit a newtonian behaviour. Replacing equation (3.23) in (3.22) and using property (3.21) the Navier Stokes equation is derived

$$\frac{\partial}{\partial t}\mathbf{u} + (\mathbf{u}\cdot\nabla)\mathbf{u} = -\frac{1}{\rho}\nabla p + \nu\,\nabla^2\mathbf{u} + \frac{1}{\rho}\mathbf{F} \tag{3.24}$$

being ν the *kinematic viscosity* $\nu = \mu/\rho$ (dimensions $[m^2/s]$). Equations (3.21) and

(3.24) with suitable boundary conditions totally describe the flow of a newtonian incompressible time-constant density fluid, but are of relevant practical use only in those very special cases where the geometry and boundary conditions of the problem allow to find an analytical solution, e.g. $2D$ flows past two parallel walls (*Couette flow*) or flow in a cylindrical pipe (*Poiseuille flow*). Fortunately it can be shown theoretically and experimentally that the viscous effects in a fluid flow are relevant only in a very limited fluid volume next to the separating surface with a rigid body (*thin boundary layer theory*) and that they decay very rapidly in the bulk of a fluid. As a consequence the standard approach to estimate fluid forces on a rigid body consists in calculating all inertial pressure effects as if the fluid was inviscid, i.e. $\nu = 0$, and then to add the viscous effects estimated by the thin boundary layer theory or experimentally.

3.2.2 Viscous effects

To get a qualitative understanding of viscous effects in a fluid flow it may be useful to calculate the order of magnitude of the ratio between inertial and viscous forces in a general fluid dynamic problem. Assuming that the problem is characterized by velocity U, length l, viscous shear coefficient μ, gravitational acceleration $g = 9.81\ m/s^2$, and fluid density ρ, consider the ratios [34]

$$F^{1/2} \triangleq \frac{Inertial\ force}{Gravitational\ force} = \frac{\rho U^2 l^2}{\rho g l^3} = U^2/gl \tag{3.25}$$

$$R \triangleq \frac{Inertial\ force}{Viscous\ force} = \frac{\rho U^2 l^2}{\mu U l} = \rho U l/\mu = U l/\nu \tag{3.26}$$

being the first the square root of the *Froude Number* and the second the *Reynolds Number* of the specific problem. As both fresh and salt water have a kinematic viscosity ν ranging form $0.8 \cdot 10^{-6}\ m^2/s$ to $1.8 \cdot 10^{-6}\ m^2/s$ for temperatures between 0° and 30° degrees Celsius, it follows that the Reynolds number for typical underwater robotic systems of $1m$ length-scale and $1m/s$ velocity-scale is $R \in [0.6, 1.2] \cdot 10^6$. This value actually suggests that in the bulk of the fluid viscous effects may be neglected with respect to the inertial ones. Notice that the different scaling properties of the Reynolds Number and the Froude Number with respect to variables of interest U, l and ν are at the basis of the difficulty in simulating the behaviour of large marine systems by scaled models. Roughly speaking viscous forces on a rigid body can be thought of as *drag* forces and lift *forces*. The former are parallel to the relative velocity of the body with respect to the fluid and the latter are normal to it.

3.2.2.1 Viscous drag forces

By dimensional analysis it can be argued [34] that the drag force F_{drag} experienced by a sphere of diameter d moving in a fluid of density ρ with velocity U can be written as $F_{drag} = \frac{1}{2}\rho U^2 S\ C_d(R)$ being $S = \pi d^2/4$ the frontal area of the sphere and $C_d(R)$ the

Reynolds dependent drag coefficient. Experimental data reported in [34] relative to a wide range of different sphere diameters d and different fluids shows the validity of that equation. Moreover the plot of C_d versus R shows a sharp discontinuity at about $R = 3 \cdot 10^5$ relative to the transition between the so called *laminar* and *turbulent* regimes. For more general slender body geometries it is assumed that the drag coefficient C_d can be thought of as the sum of a *frictional* term C_f and a *pressure* or *form* term C_p, i.e. $C_d = C_f + C_p$. The frictional term is due to the shear drag experienced by the surface of the body travelling parallel to the relative velocity U, while the pressure term is due to the frontal surface of the body normal to U. The frictional drag coefficient C_f on a slender body is usually modeled as equal to the one experienced by a flat plate of equal surface and Reynolds number. As a matter of fact the frictional drag on a flat plate in steady state laminar regime can be evaluated by means of the boundary layer theory yielding Blasius result $C_f = 1.328\ R^{-1/2}$ which is experimentally shown to hold for $R \leq 3 \cdot 10^5$. In the turbulent regime, i.e. $R \geq 3 \cdot 10^5$, the semiempirical equation of Schoenherr $0.242/\sqrt{C_f} = log_{10}(RC_f)$ holds. It is worthwhile noticing that even within this somehow "ideal" framework of steady state flat plates there is a quite large domain of Reynold numbers, i.e. $R \in [10^5, 2 \cdot 10^6]$, in which the experimental data points reported in [34] are very scattered indicating that in that range of R neither of the two models can be thought to be totally reliable. Notice that unfortunately many underwater robotic systems operate in that range of the Reynolds Number R. As far as the pressure drag coefficient C_p is concerned, there is no general result of practical interest. It is usually assumed to be roughly independent from R and it's value has to be determined experimentally for the particular body of interest.

Indeed the classical results outlined above are of little practical interest for underwater robotic applications. The experimental identification of the drag coefficients appears to be mandatory as even assuming to work with Reynold numbers far from the laminar/turbulent transition zone, which is highly unrealistic in the most common situations, the great majority of underwater robotic systems can not be modeled as slender bodies operating in steady state conditions.

3.2.2.2 Lift forces

Lift forces are another consequence of viscosity. Generally speaking there are two kind of lift forces: *hydrofoil* and *vortex shedding* lift forces. A hydrofoil is a streamlined thin body that behaves as a lifting surfaces, i.e., that experience a force normal to its surface in a wing-like fashion. The lift force F_{lift} applied to a hydrofoil of area S in a fluid of density ρ moving with steady state relative velocity U can be modeled as $F_{lift} = \frac{1}{2}\rho U^2 S\ C_l(R, \alpha)$ being α the angle of attack, i.e., the angle between U and the tangent to the surface S. As a rule of thumb the hydrofoil lift coefficient C_l can be thought to be proportional to α for small values of $|\alpha|$, e.g. $|\alpha| < 10\,\mathrm{deg}$, and sharply decaying to zero otherwise as for large values of the angle of attack stall occurs. The phenomenon of hydrofoil lift is of fundamental importance in a wide range of fluid dynamic applications as propellers, sails, wings, rudders and all kind of control surfaces. Nevertheless in all

those situations where sharp surfaces are absent or the typical operating velocities are small, as for the majority of open frame bluff body ROVs or underwater manipulators, they can be reasonably neglected.

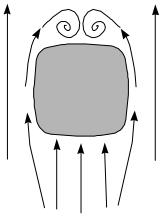

To qualitatively understand the phenomenon of vortex shedding consider a circular cylinder at rest in a still fluid. If the cylinder is suddenly accelerated to a constant regime speed normal to its axis separation of the flow will occur downstream. If upstream the flow may still be laminar, two initially symmetric vortices will start to grown in the downstream wake. These vortices can be shown to be unstable and in the final regime state of the cylinder they will be antisymmetric. The net result of the vortices instability is a periodic force normal to the cylinder axis and to its speed. This phenomenon is very important in many underwater systems: it is responsible for the strumming oscillations of cables and it may cause oscillations in many different kinds of underwater structures. As far as underwater robotic vehicles are concerned vortex shedding is usually neglected for slow motion open frame or bluff body vehicles. In principle fast slender body vehicles as many AUVs could be subject to vortex shedding periodic lift forces, but in practice it is not too difficult to employ small control surfaces in the downstream wake that limit the vortices correlation thus greatly reducing the overall vortex shedding lift effect. As far as underwater manipulators are concerned their cylindrical-like links could be reasonably subject to this phenomenon.

3.2.3 Added mass effects

The viscous effects described in paragraph (3.2.2) are not the only cause of forces applied to a rigid body moving in a fluid environment: indeed when a rigid body moves in an otherwise unbounded fluid it is expected to experience inertial forces related to the kinetic energy that the body itself induces on the whole bulk of fluid. These inertial forces have little to do with the viscosity properties of the fluid and for standard hydrodynamic Reynolds numbers ($R \geq 10^4$) they are described within the theory of ideal fluid.

3.2.3.1 On the properties of ideal fluids

A first important property of inviscid fluids is Lord Kelvin's theorem stating the "constancy of circulation in a circuit moving with the fluid in an inviscid fluid in which the density is either constant or is a function of the pressure" ([35] pag. 84). Circulation Γ on a closed circuit c moving with the same fluid particles is defined as $\Gamma \triangleq \oint_c \mathbf{u}^T d\mathbf{x}$

being $\mathbf{u}$ the fluids velocity. The time derivative of Γ is

$$\frac{d}{dt}\Gamma = \frac{d}{dt}\oint_c \mathbf{u}^T d\mathbf{x} = \oint_c (\frac{d}{dt}\mathbf{u}^T) d\mathbf{x} + \oint_c \mathbf{u}^T (\frac{d}{dt} d\mathbf{x}) \tag{3.27}$$

where the last integral is equal $\oint_c \mathbf{u}^T d\mathbf{u}$ which is zero. To evaluate the term $\oint_c (\frac{d}{dt}\mathbf{u}^T) d\mathbf{x}$ notice that the left hand side of the Navier Stokes equation (3.24) is exactly $\frac{d}{dt}\mathbf{u}^T$. Neglecting viscosity, i.e. $\nu = 0$, and assuming that the only external force applied to the fluid is the conservative gravitational force, the right hand side of equation (3.24) can be written as $-\frac{1}{\rho}\nabla(p + \rho g h)$ being $g = 9.81 m/s^2$ the gravitational acceleration and h the vertical Cartesian coordinate. Applying Stokes' theorem to equation (3.27) and replacing $\frac{d}{dt}\mathbf{u}^T = -\frac{1}{\rho}\nabla(p + \rho g h)$, the following holds:

$$\frac{d}{dt}\Gamma = \oint_c (\frac{d}{dt}\mathbf{u}^T) d\mathbf{x} = \int_S \left(\nabla \wedge \frac{d}{dt}\mathbf{u}\right)^T \mathbf{n}\, dS = -\int_S \nabla \wedge \left(\frac{1}{\rho}\nabla(p + \rho g h)\right) \cdot \mathbf{n}\, dS$$

being S any surface bounded by the closed curve c. In the standard hypothesis of incompressible fluid (equation (3.21)) the last integral is equal to zero proving Kelvin's theorem $\frac{d}{dt}\Gamma = 0$. From a physical point of view Kelvin's theorem just states that in absence of shear dissipative stress and under the action of only conservative forces a circulation state of the fluid is a steady state. Assuming that the initial state of the circulation is $\Gamma = 0$ Kelvin's theorem implies that it remains null in time and by applying Stokes' theorem again

$$\oint_c \mathbf{u}^T d\mathbf{x} = \int_S (\nabla \wedge \mathbf{u})^T \mathbf{n}\, dS = 0 \;\; \forall\, t \tag{3.28}$$

being S any surface bounded by c. From the arbitrary of S it follows that the integrand of the last integral must be identically null in time, thus showing that an inviscid incompressible fluid with no initial circulation is *irrotational*, i.e. $\nabla \wedge \mathbf{u} = 0$. Notice that equation (3.28) states that the velocity field $\mathbf{u}$ is conservative and can thus be written as the gradient of a scalar potential ϕ, i.e. the velocity field of an inviscid incompressible fluid having initial circulation equal to zero can always be written as $\mathbf{u} = \nabla\phi$. Moreover notice that as in the same hypothesis equation (3.21) holds, the scalar ϕ must be a solution of Laplace equation $\nabla^2\phi = 0$, i.e. a *harmonic* function.

The Navier Stokes equation (3.24) for an inviscid fluid ($\nu = 0$) subject to the only gravitational force can now be written in terms of the velocity potential ϕ to yield Bernoulli's equation:

$$\begin{aligned} \frac{\partial}{\partial t}\nabla\phi + (\nabla\phi \cdot \nabla)\nabla\phi &= -\frac{1}{\rho}\nabla(p + \rho g h) \Rightarrow \\ \nabla(\frac{\partial}{\partial t}\phi + \frac{1}{2}\nabla\phi \cdot \nabla\phi) &= -\frac{1}{\rho}\nabla(p + \rho g h) \Rightarrow \end{aligned}$$

$$\frac{\partial}{\partial t}\phi + \frac{1}{2}\nabla\phi \cdot \nabla\phi + C(t) \quad = \quad -\frac{1}{\rho}(p + \rho g h) \tag{3.29}$$

being $C(t)$ constant with respect to the position, but possibly function of time. $C(t)$ is related to the additive constant of the velocity potential ϕ and can be always chosen to be zero. The two terms on the right hand side of equation (3.29) are sometimes referred to as the *dynamic pressure* p and *hydrostatic pressure* $\rho g h$. The Bernoulli equation (3.29), as the Navier Stokes equation (3.24) for a viscid fluid, are general equations of motion that can describe a specific physical problem only if solved with the suitable boundary conditions. As a matter of fact all the information regarding the geometry of the problem is embedded in the boundary conditions. For a rigid body in a fluid environment the correct kinematic boundary condition to impose is that the fluid does not flow through the separating (moving) surface between itself and the body. With reference to figure

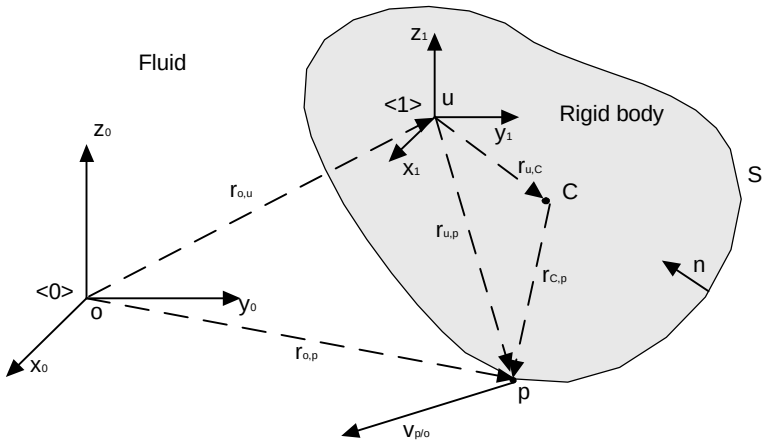

3.2.Rigid body underwater

(3.2), assuming $\mathbf{n}$ to be the unit vector normal to the separating surface pointing outside the fluid, i.e. inside the body, and $\mathbf{v}_{p/o}$ the velocity of a point p on the separating surface defined as in equation (3.9), the above stated kinematic condition is satisfied if and only if the fluid velocity $\nabla\phi$ and the surface velocity $\mathbf{v}_{p/o}$ in every point p have equal projection along $\mathbf{n}$, i.e.

$$\frac{\partial}{\partial \mathbf{n}}\phi = \mathbf{v}_{p/o}^T \mathbf{n} = (\mathbf{v}_{u/o} + \boldsymbol{\omega}_{1/0} \wedge \mathbf{r}_{u,p})^T \mathbf{n} \tag{3.30}$$

As it can be shown [34] that two different harmonic functions ϕ_1, ϕ_2 satisfying condition

(3.30) may differ only by a constant, equation (3.30) is actually just the right amount of "extra" information needed to solve the Bernoulli equation (3.29). In a real viscous fluid, equation (3.30) should hold not for points p on the separating surface of the rigid body, but for the points laying on the external face of the boundary layer within the fluid. Due to the negligeable thickness of the fluid boundary layer with respect to the rigid body for the great majority of robotic applications, it is reasonable to assume equation (3.30) to hold on the separating surface.

3.2.3.2 Dynamic pressure forces and moments on a rigid body

Within the above developed theory of ideal or inviscid fluid the total force $\mathbf{F}_{dp}$ and moment $\mathbf{N}_{dp}$ experienced by a rigid body in a fluid media due to the only dynamic pressure can be written as

$$\mathbf{F}_{dp} = \int_S p\mathbf{n}\, dS = -\rho \int_S \left(\frac{\partial}{\partial t}\phi + \frac{1}{2}\nabla\phi \cdot \nabla\phi\right) \mathbf{n}\, dS \tag{3.31}$$

$$\mathbf{N}_{dp} = \int_S p(\mathbf{r}_{o,p} \wedge \mathbf{n})\, dS = -\rho \int_S \left(\frac{\partial}{\partial t}\phi + \frac{1}{2}\nabla\phi \cdot \nabla\phi\right) (\mathbf{r}_{o,p} \wedge \mathbf{n})\, dS \tag{3.32}$$

being ϕ a harmonic function subject to boundary conditions (3.30), S the separating surface, $\mathbf{n}$ a unit normal vector and $\mathbf{r}_{o,p}$ a position vector as shown in figure (3.2). To explicitly solve equation (3.31) and (3.32) one more simplifying hypothesis is needed: the unboundedness of the fluid. As shown by Newman in [34] if the fluid is assumed to be unbounded except for the rigid body itself, equations (3.31) and (3.32) with boundary condition (3.30) can be solved analytically. To match the boundary condition (3.30) the total scalar velocity potential ϕ can be written in terms of a new vector $\boldsymbol{\psi} \in \Re^{6\times 1}$ and the generalized velocity $\boldsymbol{\nu}$ (defined by equation (3.15)) as

$$\phi = \boldsymbol{\psi}^T \boldsymbol{\nu} \tag{3.33}$$

The analytical solution of equations (3.31) and (3.32) as reported by Newman [34] yields for each component $j = 1, 2, 3$

$$F_{dp_j} = -\sum_{i=1}^{6} \left[m_{ji} \frac{d_{<1>}}{dt}\nu_i + \sum_{k,l=1}^{3} \varepsilon_{jkl}\nu_i\omega_k m_{li} \right] \tag{3.34}$$

$$N_{dp_j} = -\sum_{i=1}^{6} \left[m_{j+3,i} \frac{d_{<1>}}{dt}\nu_i + \sum_{k,l=1}^{3} \varepsilon_{jkl}\nu_i\omega_k m_{l+3,i} + \sum_{k,l=1}^{3} \varepsilon_{jkl}\nu_i\nu_k m_{li} \right] \tag{3.35}$$

being $\boldsymbol{\nu}$ the generalized velocity defined in equation (3.15), $\boldsymbol{\omega}$ the angular velocity $\boldsymbol{\omega}_{1/0}$, ε_{jkl} the *Levi-Civita density* defined such that the j^{th} component of the vector product

between to given vectors $\mathbf{a}$ and $\mathbf{b}$ is $(\mathbf{a} \wedge \mathbf{b})_j = \sum_{k,l=1}^{3} \varepsilon_{jkl} a_k b_l$, i.e.

$$\begin{aligned} \varepsilon_{jkl} &= 1 \text{ if } jkl = \left\{ \begin{array}{l} 1,2,3 \\ 2,3,1 \\ 3,1,2 \end{array} \right. \\ \varepsilon_{jkl} &= -1 \text{ if } jkl = \left\{ \begin{array}{l} 1,3,2 \\ 2,1,3 \\ 3,2,1 \end{array} \right. \\ \varepsilon_{jkl} &= 0 \text{ otherwise} \end{aligned}$$

and m_{ji} the components of the *added mass tensor* defined as

$$m_{ji} \triangleq \rho \int_S \psi_i \frac{\partial}{\partial \mathbf{n}} \psi_j \, dS \tag{3.36}$$

being ψ_i the components of the $\boldsymbol{\psi}$ vector introduced in (3.33). Each component of $\boldsymbol{\psi}$ has to be harmonic (i.e., $\nabla^2 \psi_i = 0$) in the bulk of the fluid and has to satisfy the kinematic conditions

$$\frac{\partial \psi_i}{\partial n} = n_i \; \forall \; i = 1,2,3 \tag{3.37}$$

$$\frac{\partial \psi_i}{\partial n} = (\mathbf{r}_{u,p} \wedge \mathbf{n})_{i-3} \; \forall \; i = 4,5,6 \tag{3.38}$$

on the separating surface S. As a consequence each added mass component m_{ji} given by equations (3.36) depends only on the shape of the boundary surface S and on the constant (by hypothesis (3.21)) fluid density ρ. Equations (3.34) and (3.35) can be expressed in a more compact form writing the added mass tensor as

$$M_A = \left[\begin{array}{cc} M_{11} & M_{12} \\ M_{21} & M_{22} \end{array} \right] \tag{3.39}$$

being each M_{ij} a 3×3 matrix. With such notation equations (3.34) and (3.35) can be written as

$$\mathbf{F}_{dp} = -(M_{11} \; M_{12}) \frac{d_{<1>}}{dt} \boldsymbol{\nu} - \boldsymbol{\omega}_{1/0} \wedge [(M_{11} \; M_{12}) \, \boldsymbol{\nu}] \tag{3.40}$$

$$\begin{aligned} \mathbf{N}_{dp} = & -(M_{21} \; M_{22}) \frac{d_{<1>}}{dt} \boldsymbol{\nu} - \boldsymbol{\omega}_{1/0} \wedge [(M_{21} \; M_{22}) \, \boldsymbol{\nu}] \\ & - \mathbf{v}_{u/o} \wedge [(M_{11} \; M_{12}) \, \boldsymbol{\nu}] \end{aligned} \tag{3.41}$$

or in spatial notation $\boldsymbol{\tau}_{dp} \triangleq (\mathbf{F}_{dp}^T, \mathbf{N}_{dp}^T)^T$

$$\boldsymbol{\tau}_{dp} = -M_A \frac{d_{<1>}}{dt} \boldsymbol{\nu} - C_A(\boldsymbol{\nu}) \, \boldsymbol{\nu} \tag{3.42}$$

being

$$C_A(\boldsymbol{\nu}) \triangleq \begin{bmatrix} S(\boldsymbol{\omega}_{1/0}) & 0 \\ S(\mathbf{v}_{u/o}) & S(\boldsymbol{\omega}_{1/0}) \end{bmatrix} \begin{bmatrix} M_{11} & M_{12} \\ M_{21} & M_{22} \end{bmatrix} \tag{3.43}$$

Notice that from equations (3.40) and (3.41) follows that a rigid body subject to a constant linear velocity, i.e. $\mathbf{v}_{u/o} = const.$ and $\boldsymbol{\omega}_{1/0} = 0$, in an infinite inviscid fluid does not experience any dynamic pressure force (although it may experience a non zero moment due to the term $\mathbf{v}_{u/o} \wedge [(M_{11}\ M_{12})\ \boldsymbol{\nu}]$ in (3.41)); this fact is often referred to as the *D'Alembert paradox* in the fluid dynamic literature. Applying Green's theorem to the added mass components definition (3.36) it can be shown [34] that the added mass tensor M_A of a rigid body in an ideal infinite fluid is symmetrical, i.e. $m_{ij} = m_{ji}$. Moreover starting from the energy conservation principle it can be shown [35] [34] that M_A is related to the fluid kinetic energy by the quadratic form equation

$$T_{fluid} = \frac{1}{2}\boldsymbol{\nu}^T\ M_A\ \boldsymbol{\nu}$$

being $\boldsymbol{\nu}$ the generalized rigid body velocity defined in equation (3.15). This property shows that M_A is positive definite.

The practical limit of the above formulation describing the dynamic pressure on a whatsoever rigid body is related to the calculation of the added mass coefficients m_{ij}. These have been evaluated analytically (see for example [37]) only for very special geometries like spheroids or ellipsoids that are of very limited interest in real applications. To model real underwater system M_A should be estimated experimentally. Moreover the above formulation has been derived with a number of ideal hypothesis that are here summarized:

(1) the body in the fluid is rigid
(2) the fluid is incompressible (equation (3.21))
(3) the fluid is ideal, i.e. inviscid, which implies Lord Kelvin's theorem and the irrotational nature of the fluid as derived in equation (3.28)
(4) the fluid is unbounded except for the rigid body itself

If the first two hypothesis are reasonably satisfied in most applications, the last two of them require some comments. The assumption of inviscid fluid for the derivation of the dynamic pressure forces is justified by the large value of the Reynolds number in the great majority of underwater robotic applications; of course viscous effects as drag and lift have to be taken into account by independent terms in the equation of motion of the system. As far as the last hypothesis is concerned an illustrative example of what happens to a sphere moving in the presence of an infinite fixed rigid wall is reported from [35]: if x and y are two Cartesian axes respectively normal and parallel to the wall (refer to figure (3.3)), a sphere of radius r has a kinetic energy given to a first

approximation by $T = \frac{1}{2}(Au^2 + Bv^2)$, being $u = \dot{x}$ and $v = \dot{y}$ the surge and sway velocities, $A = m + \frac{1}{2}m_f(1 + \frac{3}{8}(\frac{r}{x})^3)$, $B = m + \frac{1}{2}m_f(1 + \frac{3}{16}(\frac{r}{x})^3)$, m the mass of the sphere and m_f the mass of the displaced fluid. By applying Lagrange equations to the

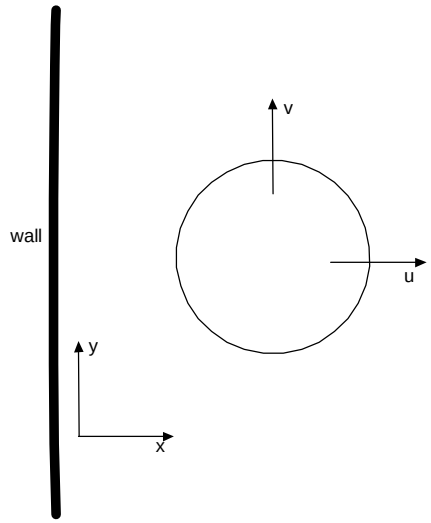

3.3.Sphere inpresence of a wall

given kinetic energy the forces along the x and y axes follow

$$\begin{aligned} F_x &= \frac{9}{64}m_f\frac{r^3}{x^4}(-2u^2 + v^2) \\ F_y &= -\frac{9}{32}m_f\frac{r^3}{x^4}\,u\,v \end{aligned}$$

from which it is seen that the dynamic pressure force tends to repel the sphere if this moves at constant speed towards or away from the wall ($v = 0, u \neq 0$) and attracts it if the sphere tends to move parallel to the wall ($u = 0, v \neq 0$).

3.2.4 Current effects

Within the above described theory nothing have been said about eventual fluid currents. From the definition (3.33) and from the equations (3.37) and (3.38) it should be noticed that if the fluid is subject to a uniform motion $\mathbf{v}_{fluid/o}(t)$, the rigid body generalized velocity $\boldsymbol{\nu} = (\mathbf{v}_{u/o}^T, \boldsymbol{\omega}_{1/0}^T)^T$ appearing in equation (3.42) must be replaced by the relative velocity $((\mathbf{v}_{u/o} - \mathbf{v}_{fluid/0})^T, \boldsymbol{\omega}_{1/0}^T)^T$. As a matter of fact such a uniform current would also induce a buoyancy-like force, sometimes called *horizontal-buoyancy*, proportional to the product of the displaced fluid m_f times the fluid acceleration $\frac{d_{<0>}}{dt}\mathbf{v}_{fluid/o}$. These forces are usually taken into account when underwater robotic systems are simulated [14] [38] [23] [39] but are usually neglected in control and identification schemes as it is

very difficult to measure $\mathbf{v}_{fluid/o}$ and its time derivative. If the current is not uniform, as in presence of waves, the situation is even more complex as also the gradient of the fluid velocity is expected to produce a pressure force on the body. This latter phenomenon, which is fundamental in the modeling of surface systems, is generally neglected in deep water, but should be taken somehow into account in shallow water [40] [41] [42] [43].

3.2.5 Weight and buoyancy

Weight and buoyancy generalized force may be modeled as

$$\begin{pmatrix} \mathbf{F}_{wb} \\ \mathbf{N}_{wb} \end{pmatrix} = g \begin{bmatrix} -m\, I_{3\times 3} & m_f\, I_{3\times 3} \\ -m\, S(\mathbf{r}_{u,c}) & m_f\, S(\mathbf{r}_{u,B}) \end{bmatrix} \begin{pmatrix} {}^1\mathbf{k}_0 \\ {}^1\mathbf{k}_0 \end{pmatrix} \tag{3.44}$$

Being m_f the displayed liquid volume, m the rigid body mass, $g = 9.81\ m/s^2$ the gravitational acceleration, $\mathbf{r}_{u,B}$ the center of buoyancy local position vector, $\mathbf{r}_{u,c}$ the center of mass local position vector and ${}^1\mathbf{k}_0$ the projection of the z-axis inertial unit vector on the local reference $< 1 >$.

3.3 Underwater Remotely Operated Vehicles Model

The rigid body dynamic equations described in the previous sections can be viewed as the building blocks for more complex robotic system models as the ones of underwater vehicles or manipulators. In particular the dynamic models of a bluff body UUV will be derived. Generally bluff body UUVs are designed for low speed operations and are not equipped with lifting or control surfaces so their dynamic models do not take into account lift forces. The added mass and viscous drag effects are modeled on the basis of the rigid body theory described in the previous sections. Although drag is a distributed force on the surface of the vehicle for the sake of simplicity it is usually modeled within a lumped parameter formulation. The standard approach to drag modeling consists in the sum of a linear and quadratic term in the relative generalized six dimensional velocity $\boldsymbol{\nu}$, i.e.,

$$\mathbf{F}_{drag} = -D_{\boldsymbol{\nu}}\boldsymbol{\nu} - D_{\boldsymbol{\nu}|\boldsymbol{\nu}|}\boldsymbol{\nu}|\boldsymbol{\nu}| \tag{3.45}$$

being the matrixes $D_{\boldsymbol{\nu}}$ and $D_{\boldsymbol{\nu}|\boldsymbol{\nu}|}$ positive definite. A further and very common simplification [32] consists in assuming $D_{\boldsymbol{\nu}}$ and $D_{\boldsymbol{\nu}|\boldsymbol{\nu}|}$ diagonal thus neglecting the viscous drag coupling. The most common notation for the drag coefficients is

$$D_{\boldsymbol{\nu}} = diag(X_u, Y_v, Z_w, K_p, M_q, N_r) \tag{3.46}$$

$$D_{\boldsymbol{\nu}|\boldsymbol{\nu}|} = diag(X_{u|u|}, Y_{v|v|}, Z_{w|w|}, K_{p|p|}, M_{q|q|}, N_{r|r|}) \tag{3.47}$$

To obtain the complete model of a UUV thruster and cable dynamics are to be considered. The cable dynamics is sometimes modeled in simulation studies, but even being

potentially a major source of drag or external applied force on an ROV, it is usually neglected in the design of ROV control systems. Indeed as for underwater currents, also cable forces are usually assumed to be disturbances of a nominal model that neglects them explicitly. From a practical point of view this can be an acceptable working hypothesis when the vehicle operates in a limited area, the cable is neutrally buoyant and is not in tension. If these conditions are not satisfied the cable forces applied on an ROV may be large and should be taken into account by an explicit term in the dynamic equation. As all the experimental data presented in this work has been collected matching the above stated working hypothesis regarding the cable, in the sequel its dynamics will not be taken explicitly into consideration but assumed to be a disturbance of the nominal model.

3.3.1 Thruster dynamics

As far as thruster dynamics is concerned a steady state equation can be obtained by dimensional analysis [34] yielding

$$\frac{T}{\rho n^2 d^4} = K(J) \tag{3.48}$$

being J the advance ratio,

$$J = \frac{U}{nd} \begin{cases} U \text{ constant thruster velocity} \\ n \text{ number of revolutions per second} \\ d \text{ propeller diameter} \end{cases}$$

T the thrust and ρ the water density. In the great majority of the applications K in equation (3.48) is assumed to be constant and the square dependance of T on n is written as $n|n|$ to take into account the sign of the thrust. Moreover in real application saturation occurs, thus the usual thrust model is assumed to be [32]

$$T = a\, n|n| - b\, n v_a \tag{3.49}$$

being v_a the velocity of advance of the water through the propeller blades. The saturation term may be very important at high speeds, but is usually neglected in standard low speed operating conditions of ROVs. A dynamic thruster model taking into account the motor dynamics has been proposed by Yoerger et al. [44] and consists of the following equations:

$$\begin{aligned} \frac{dn}{dt} &= \beta\, \tau - \alpha\, n|n| \\ T &= C_t\, n|n| \end{aligned}$$

being α and β constants, and τ the input torque. Although the topic of thruster dynamic modeling and control has received a quite large attention in the past years [45]

[46] a simple steady state model as $T = a\ n|n|$ in which the propeller revolution rate is assumed to be linear in the applied DC motor voltage, thus neglecting the motor dynamics, is actually a very good approximation in all those applications in which n does not suddenly change sign. In the sequel the thruster applied force will be modeled as

$$T = c\ V|V| \tag{3.50}$$

being V the applied DC motor voltage and c a constant to be experimentally identified. A difficulty related with this approach is that, as the identification of the c constant in equation (3.50) is generally performed putting the single thruster in a cavitation tunnel and measuring the thrust as a function of the applied voltage, the propeller hull interactions are neglected. Indeed due to possible propeller hull interactions the operating conditions of the thruster in the cavitation tunnel may differ from the real ones especially, but not only, when open frame vehicles are considered. It will be shown in the next chapter by experimental data relative to the ROMEO open frame ROV that the propeller hull interaction may be significant and must be taken into account. Another kind of potentially important hydrodynamic "interference" phenomenon regarding the thrusters dynamics is *momentum drag*. This phenomenon occurs when a thruster moves

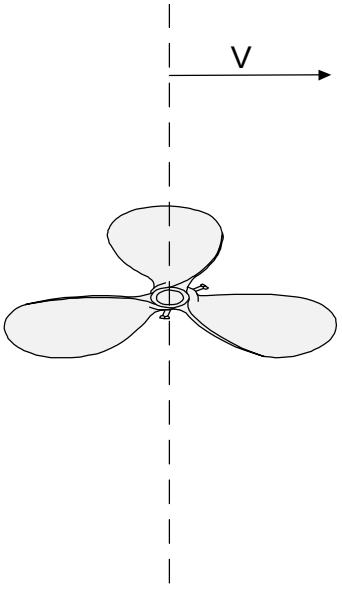

3.4.Momentum drag

normally to its axis. With reference to figure (3.4) notice that in order to produce a flow parallel to the propeller axis, the fluid must be first accelerated to the same axis normal velocity V. This produces a drag force in the direction normal to the propeller axis that

may be modeled as

$$\mathbf{F}_{md} = -\alpha n \mathbf{V} \tag{3.51}$$

being n the propeller revolution rate, $\mathbf{V}$ the axis normal velocity and α a constant parameter. Momentum drag may be important in ROV systems as most of them are equipped with both horizontal and vertical thrusters that allow full translational control in $3D$ and that frequently operate together. Nevertheless to the knowledge of the author the literature relative to the modeling of such phenomenon in ROVs is limited to the only work of K. R. Goheen [38] and papers there cited.

3.3.2 Overall ROV Model

The complete model of an open frame UUV can be written as

$$\begin{aligned}&(M + M_A)\frac{d_{<1>}}{dt}\boldsymbol{\nu} + [C(\boldsymbol{\omega}_{1/0}) + C_A(\boldsymbol{\nu})]\boldsymbol{\nu} + \\ &+D_{\boldsymbol{\nu}}\boldsymbol{\nu} + D_{\boldsymbol{\nu}|\boldsymbol{\nu}|}\boldsymbol{\nu}|\boldsymbol{\nu}| - gW\,\mathbf{k} = \boldsymbol{\tau}_{th} + \boldsymbol{\delta}\end{aligned} \tag{3.52}$$

being all the terms defined as follows:

$$M \triangleq \begin{bmatrix} m\,I_{3\times 3} & -m\,S(\mathbf{r}_{u,c}) \\ m\,S(\mathbf{r}_{u,c}) & I_u \end{bmatrix} \text{ as in equation (3.16)}$$

$$C(\boldsymbol{\omega}_{1/0}) \triangleq \begin{bmatrix} m\,S(\boldsymbol{\omega}_{1/0}) & -m\,S(\boldsymbol{\omega}_{1/0})\,S(\mathbf{r}_{u,c}) \\ m\,S(\mathbf{r}_{u,c})\,S(\boldsymbol{\omega}_{1/0}) & -S(I_u\boldsymbol{\omega}_{1/0}) \end{bmatrix} \text{ as in equation (3.17)}$$

$$M_A \triangleq \begin{bmatrix} M_{11} & M_{12} \\ M_{21} & M_{22} \end{bmatrix} \text{ as in equation (3.39)}$$

$$C_A(\boldsymbol{\nu}) \triangleq \begin{bmatrix} S(\boldsymbol{\omega}_{1/0}) & 0 \\ S(\mathbf{v}_{u/o}) & S(\boldsymbol{\omega}_{1/0}) \end{bmatrix} \begin{bmatrix} M_{11} & M_{12} \\ M_{21} & M_{22} \end{bmatrix} \text{ as in equation (3.43)}$$

$$D_{\boldsymbol{\nu}} \triangleq diag(X_u, Y_v, Z_w, K_p, M_q, N_r) \text{ as in equation (3.46)}$$

$$D_{\boldsymbol{\nu}|\boldsymbol{\nu}|} \triangleq diag(X_{u|u|}, Y_{v|v|}, Z_{w|w|}, K_{p|p|}, M_{q|q|}, N_{r|r|}) \text{ as in equation (3.47)}$$

$$W \triangleq \begin{bmatrix} -m\,I_{3\times 3} & m_f\,I_{3\times 3} \\ -m\,S(\mathbf{r}_{u,c}) & m_f\,S(\mathbf{r}_{u,B}) \end{bmatrix} \text{ as in equation (3.44)}$$

$$\mathbf{k} \triangleq ({}^1\mathbf{k}_0^T, {}^1\mathbf{k}_0^T)^T$$

$\boldsymbol{\tau}_{th}$ is the generalized thruster force

$\boldsymbol{\delta}$ disturbance vector

As discussed in the previous sections, the generalized velocity vector $\boldsymbol{\nu}$ defined in equation (3.15) has to be replaced with the relative velocity vector $\boldsymbol{\nu}_{rel} = ((\mathbf{v}_{u/o} - \mathbf{v}_{fluid/0})^T, \boldsymbol{\omega}_{1/0}^T)^T$ in order to take into account eventual irrotational uniform constant underwater currents. Currents with time changing velocity give rise to an additional hydrodynamic force sometimes called horizontal buoyancy (see section 3.2.4) that can be modelled and simulated only with the knowledge of the fluids inertial acceleration which is usually unaccessible. The velocity gradient of non uniform currents may cause a pressure gradient on the vehicles hull that induces another hydrodynamic load. This latter phenomenon is generally unmodeled as it would require a complete knowledge of the current velocity filed.

3.4 Underwater Manipulator Model

The model of an underwater manipulator can be deduced on the basis of the standard model of a land industrial manipulator and the hydrodynamic forces acting on an underwater rigid body described in the previous sections. Both Lagrange and Newton-Euler methods have been adopted in the literature for the synthesis of an underwater arm model. Schjølberg et al.[22] have derived a lumped parameter dynamic model of an underwater manipulator-vehicle system by an iterative Newton-Euler method. The proposed model is an extension of the classical land manipulator model as outlined by Spong et al.[47] to the underwater environment. The resulting dynamic equation has the same structure of land manipulators, i.e.

$$M(\mathbf{q})\ddot{\mathbf{q}} + C(\mathbf{q}, \dot{\mathbf{q}})\dot{\mathbf{q}} + D(\mathbf{q}, \dot{\mathbf{q}})\dot{\mathbf{q}} + \mathbf{g}(\mathbf{q}) = \boldsymbol{\tau}_m \tag{3.53}$$

being $\mathbf{q}$ the generalized link coordinate vector, M the sum of the standard inertia matrix with the added mass one, C the centripetal-Coriolis matrix including the added mass terms responsible of the hydrodynamic coupling (D'Alembert paradox) discussed previously for a single rigid body, D the hydrodynamic lift and drag generalized forces, $\mathbf{g}$ the weight and buoyancy generalized forces and $\boldsymbol{\tau}_m$ the applied joint generalized forces. The same model structure has been derived with the use of Kane's equations by Tarn et al. both for a single n-axis manipulator-vehicle system [48] and for multiple manipulators-vehicle system [24]. A manipulator-vehicle dynamic model may be use either for simulation purposes, or for control system design.

As far as simulation is concerned McMillan et al.[23] have described an efficient simulator based on an articulated-body algorithm taking into account the major hydrodynamic forces on a manipulator-vehicle system. They show that the computational requirement for a mobile six degrees of freedom underwater manipulator is about double then for a land system, although the amount of computation still grows linearly with the degrees of freedom. In their work drag is modeled as a distributed effect on each link which is approximated with a cylinder. The same kind of drag model is adopted in [49] where a fixed base partially (or totally) immersed manipulator is considered.

Before taking into account the control system design of an underwater-vehicle system it is necessary to understand the actual relevance of hydrodynamic effects on an underwater industrial manipulator and on the overall arm-vehicle system. To this extent most interesting is the experience of the Deep Submergence Laboratory of the Woods Hole Oceanographic Institution as reported in [50]: as the major hydrodynamic effect on a fixed base manipulator is damping, the authors conclude that on their system *"while performing routine tasks hydrodynamic effects have no significant effect on manipulator control"*. On the other hand for a mobile base system the effects of fast manipulator motion on the vehicle have experimentally shown to be relevant. Intuitively this is reasonable as it corresponds to a "swimming-like" coupling effect between the manipulator and the vehicle. This phenomenon has been extensively analyzed by McLain et al.[51] [52] [53] [25] both theoretically and experimentally. Their approach basically consists of two steps: first a model arm, developed on the basis of Sarpkaya's study of the added mass and drag coefficients on a cylinder [54], is experimentally identified. Then the dynamic model of the arm is used to compensate the arm-vehicle coupling effect by a model-based feedforward signal. Experimental tests carried out with a single link arm on an unmanned underwater vehicle [53] show good improvements in the control performance with only a small (5%) increase in vehicle thrust. Nevertheless the implementation of such approach on a real system would require an accurate and complete identification of the underwater arm model and a much higher computational burden with all the drawbacks that this implies. In the words of Sayers et al. [50] "*when operating at normal speeds in the real environment the principal benefit resulting from a full model for combined manipulator/vehicle motion is not the ability to compensate for dynamic effects on-line, but rather the assistance it provides in planning alternative motions off-line*". As a matter of fact to avoid a complete off-line identification procedure an adaptive approach may be considered. Simulation results of an adaptive scheme for underwater manipulator-vehicle control have been reported by Mahesh et al.[21] and adaptive algorithms for underwater manipulators have been analyzed also by Ramadorai et al. [12]. Assuming a full knowledge of the system parameters a feedback linearization control of the vehicle manipulator system may be implemented as suggested Schjølberg et al.[55]. Finally robust control approaches to the problem have been taken into account in [27].

Chapter 4
Identification

In this chapter the topic of underwater robotic system identification will be addressed. Experimental results regarding open frame ROVs will be outlined.

4.1 Estimation approach

In order to describe the adopted estimation approach some notation will be introduced. Suppose that a model of some phenomena is given in the form

$$\mathbf{y_0}(t) = H(\mathbf{x}(t), t, \boldsymbol{\theta}) \tag{4.1}$$

being t the time, $\mathbf{y_0}(t) \in \Re^{n\times 1}$ a measurable quantity (either deterministic or stochastic), $\mathbf{x}(t) \in \Re^{m\times 1}$ a time dependent variable and $\boldsymbol{\theta} \in \Re^{p\times 1}$ a vector of parameters: the problem of parameter estimation consists in calculating some "estimate" $\hat{\boldsymbol{\theta}}$ (estimates will be denoted by a hat) of the parameter vector $\boldsymbol{\theta}$ given noisy measures $\mathbf{y}(t) = \mathbf{y_0}(t) + \boldsymbol{\varepsilon}$ (being $\boldsymbol{\varepsilon}$ the measurement noise). Notice that due to the unavoidable measurement noise the measures $\mathbf{y}(t)$ of $\mathbf{y_0}(t)$ are random variables being H either a stochastic or a deterministic model. The approach to the estimation problem is different according to the nature of the parameter vector $\boldsymbol{\theta}$: if it is a vector of unknown constants a so called *non-Bayesian* approach should be followed, otherwise a *Bayesian* one. Within the Bayesian approach the parameter vector is a random variable having a probability density function (pdf) $p(\boldsymbol{\theta})$ and one may argue that a good estimate of it could be the mode of the pdf of $\boldsymbol{\theta}$ conditioned to the measurements $\mathbf{y}$, i.e.

$$\hat{\boldsymbol{\theta}} \triangleq \arg\max_{\boldsymbol{\theta}} p(\boldsymbol{\theta}|\mathbf{y}) = \arg\max_{\boldsymbol{\theta}} \frac{p(\mathbf{y}|\boldsymbol{\theta})p(\boldsymbol{\theta})}{p(\mathbf{y})} = \arg\max_{\boldsymbol{\theta}} p(\mathbf{y}|\boldsymbol{\theta})p(\boldsymbol{\theta})$$

Within the non-Bayesian approach the parameter vector is an unknown deterministic quantity which has no probability density function (or better, its pdf is a Dirac function centered on the unknown value $\boldsymbol{\theta}$). A typical non-Bayesian estimator is the maximum likelihood estimator, i.e. the parameter estimate $\hat{\boldsymbol{\theta}}_{MLE}$ is the mode of the measurement probability density function given the deterministic parameter vector,

$$\hat{\boldsymbol{\theta}}_{MLE} \triangleq \arg\max_{\boldsymbol{\theta}} p(\mathbf{y}|\boldsymbol{\theta}) \tag{4.2}$$

The pdf of the measurements $\mathbf{y}$ given $\boldsymbol{\theta}$ is called *likelihood function* $\Lambda_{\mathbf{y}}(\boldsymbol{\theta}) \triangleq p(\mathbf{y}|\boldsymbol{\theta})$ and the estimator described by the above equation is called *maximum likelihood estimator* (MLE). The underwater robotic models developed in the previous chapters are deterministic models that contain only deterministic parameters as masses, drag coeffi-

cients and geometrical quantities that should be regarded as unknown constants rather then random variables. This suggests to work within the non-Bayesian framework and in particular estimation should be performed with a maximum likelihood technique. Notice that according to the above statements regarding the stochastic nature of $\mathbf{y}(t)$ due to the measurement noise $\boldsymbol{\varepsilon}$, in both the Bayesian and non-Bayesian frameworks, the estimate $\hat{\boldsymbol{\theta}}$ of the parameter vector $\boldsymbol{\theta}$ is a random variable either if $\boldsymbol{\theta}$ is a deterministic quantity or a stochastic one. Indeed important informations on the model structure can be deduced analyzing the covariance of $\hat{\boldsymbol{\theta}}$. As a matter of fact the underwater robotic models to identify are linear in the unknown parameters, thus least squares estimation can be applied.

4.1.1 Least Squares Technique

Within this paragraph the least squares technique for estimation of models linear in their parameters will be reviewed in order to introduce the adopted notation and to outline the criteria that have been used for input and model selection. As all the following results are standard in the identification literature many of them will be reported only for reference and without proof.

If the equation (4.1) model happens to be linear in $\boldsymbol{\theta}$,

$$\mathbf{y_0}(t) = H(\mathbf{x}(t), t)\,\boldsymbol{\theta} \Rightarrow \mathbf{y}(t) = H(\mathbf{x}(t), t)\,\boldsymbol{\theta} + \boldsymbol{\varepsilon}$$

one can analytically calculate the *least squares estimate* (LS) $\hat{\boldsymbol{\theta}}_{LS}$ defined as

$$\hat{\boldsymbol{\theta}}_{LS} \triangleq \arg\min_{\boldsymbol{\theta}} J_{LS} = \arg\min_{\boldsymbol{\theta}} \| \mathbf{y}(t) - H(\mathbf{x}(t), t)\,\boldsymbol{\theta} \|^2 \tag{4.3}$$

being J_{LS} the least squares cost function

$$J_{LS} \triangleq (\mathbf{y}(t) - H(\mathbf{x}(t), t)\,\boldsymbol{\theta})^T (\mathbf{y}(t) - H(\mathbf{x}(t), t)\,\boldsymbol{\theta}) \tag{4.4}$$

equivalent to the squared norm of the measuring error vector $\|\boldsymbol{\varepsilon}\|^2$ for a deterministic model H. By direct calculation it follows that

$$\hat{\boldsymbol{\theta}}_{LS} = (H^T H)^{-1} H^T \mathbf{y} \tag{4.5}$$

showing that the existence of this estimator relies on the existence of the inverse of $H^T H$ (*observability condition*). If the measurement vector $\mathbf{y}$ of a given process is a stochastic variable having mean $E_{\mathbf{y}}[\mathbf{y}] = H\boldsymbol{\theta}$ and covariance $E_{\mathbf{y}}[(\mathbf{y} - H\boldsymbol{\theta})(\mathbf{y} - H\boldsymbol{\theta})^T] = \sigma^2 I$[1] being I the identity matrix, then the least squares estimate (4.5) has the following properties [56]:

(1) it is linear in $\mathbf{y}$

[1] if H is a deterministic model this is equivalent to the statement that the measurement noise has zero mean and covariance $I\sigma^2$

(2) it is *unbiased*, i.e. $E_{\mathbf{y}}[\hat{\boldsymbol{\theta}}_{LS}] = \boldsymbol{\theta}$
(3) $cov(\hat{\boldsymbol{\theta}}_{LS}) \triangleq E_{\mathbf{y}}[(\hat{\boldsymbol{\theta}}_{LS} - \boldsymbol{\theta})(\hat{\boldsymbol{\theta}}_{LS} - \boldsymbol{\theta})^T] = \sigma^2(H^T H)^{-1}$
(4) $cov(\hat{\boldsymbol{\theta}}_{LS}) \leq cov(\hat{\boldsymbol{\theta}}_{ULE})$ being $\hat{\boldsymbol{\theta}}_{ULE}$ the estimate given by *any other* unbiased linear estimator.

This last property is equivalent to the statement that in the given hypothesis the least squares estimator is a so called *best linear unbiased estimator* (BLUE). Moreover in the above equations the function $E_{\mathbf{y}}$ is the expectation operator defined as

$$E_{\mathbf{y}}[f(\mathbf{y})] = \int f(\mathbf{y})\, p_{\mathbf{y}}(\mathbf{y})\, d\mathbf{y}$$

Property (1) is immediate, properties (2) and (3) can be proven by direct calculation

$$E_{\mathbf{y}}(\hat{\boldsymbol{\theta}}_{LS}) = E_{\mathbf{y}}[(H^T H)^{-1} H^T \mathbf{y}] = (H^T H)^{-1} H^T E_{\mathbf{y}}[\mathbf{y}] = (H^T H)^{-1} H^T H\boldsymbol{\theta} = \boldsymbol{\theta}$$

and

$$\hat{\boldsymbol{\theta}}_{LS} - \boldsymbol{\theta} = (H^T H)^{-1} H^T \mathbf{y} - \boldsymbol{\theta} = (H^T H)^{-1} H^T (\mathbf{y} - H\boldsymbol{\theta}) \Rightarrow$$

$$cov(\hat{\boldsymbol{\theta}}_{LS}) \triangleq E_{\mathbf{y}}[(\hat{\boldsymbol{\theta}}_{LS} - \boldsymbol{\theta})(\hat{\boldsymbol{\theta}}_{LS} - \boldsymbol{\theta})^T] =$$

$$= (H^T H)^{-1} H^T E_{\mathbf{y}}[(\mathbf{y} - H\boldsymbol{\theta})(\mathbf{y} - H\boldsymbol{\theta})^T] H (H^T H)^{-1} =$$

$$= (H^T H)^{-1} H^T \sigma^2 I\, H (H^T H)^{-1} = \sigma^2 (H^T H)^{-1} \Rightarrow$$

$$cov(\hat{\boldsymbol{\theta}}_{LS}) = \sigma^2 (H^T H)^{-1} \tag{4.6}$$

Property (4) can be proven as follows [56]: by definition a linear unbiased estimator C is such that $C\mathbf{y} = \hat{\boldsymbol{\theta}}_{LUE}$ and

$$E_{\mathbf{y}}[\hat{\boldsymbol{\theta}}_{LUE}] = E_{\mathbf{y}}[C\mathbf{y}] = CE_{\mathbf{y}}[\mathbf{y}] = CH\boldsymbol{\theta} = \boldsymbol{\theta}$$

for any $\boldsymbol{\theta}$ so that

$$CH = I \tag{4.7}$$

By direct calculation the covariance of $\hat{\boldsymbol{\theta}}_{ULE}$ is

$$\begin{aligned} cov(\hat{\boldsymbol{\theta}}_{LUE}) &\triangleq E_{\mathbf{y}}[(\hat{\boldsymbol{\theta}}_{LUE} - \boldsymbol{\theta})(\hat{\boldsymbol{\theta}}_{LUE} - \boldsymbol{\theta})^T] = E_{\mathbf{y}}[(C\mathbf{y} - \boldsymbol{\theta})(C\mathbf{y} - \boldsymbol{\theta})^T] = \\ &= E_{\mathbf{y}}[(C\mathbf{y} - CH\boldsymbol{\theta} + CH\boldsymbol{\theta} - \boldsymbol{\theta})(C\mathbf{y} - CH\boldsymbol{\theta} + CH\boldsymbol{\theta} - \boldsymbol{\theta})^T] = \\ &= E_{\mathbf{y}}[(C\mathbf{y} - CH\boldsymbol{\theta})(C\mathbf{y} - CH\boldsymbol{\theta})^T] = CE_{\mathbf{y}}[(\mathbf{y} - H\boldsymbol{\theta})(\mathbf{y} - H\boldsymbol{\theta})^T] C^T = \\ &= CC^T\sigma^2 \end{aligned}$$

Next consider the positive semi-definite matrix DD^T being $D = C - (H^T H)^{-1} H^T$. By direct calculation the following holds:

$$\begin{aligned} DD^T &= (C - (H^T H)^{-1} H^T)(C - (H^T H)^{-1} H^T)^T = \\ &= CC^T - (H^T H)^{-1} H^T C^T - CH(H^T H)^{-1} + (H^T H)^{-1} = \\ &= CC^T - (H^T H)^{-1} \geq 0 \end{aligned}$$

which implies property (4).

With the same kind of calculations it can be shown that the BLUE estimator for a process having mean $E_{\mathbf{y}}[\mathbf{y}] = H\boldsymbol{\theta}$ and covariance $E_{\mathbf{y}}[(\mathbf{y} - H\boldsymbol{\theta})(\mathbf{y} - H\boldsymbol{\theta})^T] = \Sigma$ is given by

$$\hat{\boldsymbol{\theta}}_{WLS} = (H^T \Sigma^{-1} H)^{-1} H^T \Sigma^{-1} \mathbf{y} \tag{4.8}$$

having covariance

$$cov(\hat{\boldsymbol{\theta}}_{WLS}) \triangleq E_{\mathbf{y}}[(\hat{\boldsymbol{\theta}}_{WLS} - \boldsymbol{\theta})(\hat{\boldsymbol{\theta}}_{WLS} - \boldsymbol{\theta})^T] = (H^T \Sigma^{-1} H)^{-1} \tag{4.9}$$

This BLUE estimator may be regarded as a *Weighted Least Squares* estimator as it can be seen by direct calculation that $\hat{\boldsymbol{\theta}}_{WLS}$ given by equation (4.8) minimizes with respect to $\boldsymbol{\theta}$ the cost function J_{WLS} defined as

$$J_{WLS} \triangleq (\ \mathbf{y}(t) - H(\mathbf{x}(t), t)\ \boldsymbol{\theta}\ )^T\ \Sigma^{-1}\ (\ \mathbf{y}(t) - H(\mathbf{x}(t), t)\ \boldsymbol{\theta}\ ) \tag{4.10}$$

Equation (4.6) tells us a great deal about the precision and reliability of the estimates calculated by the least squares technique: if H is a deterministic model then σ is the standard deviation of the measurement noise and the covariance of the estimates will be proportional to it. Even more interesting is the dependance of $cov(\hat{\boldsymbol{\theta}}_{LS})$ on $(H^T H)^{-1}$. This matrix depends on the input signal $\mathbf{x}(t)$ that in the identification experiments is designed by the experimenter keeping into account all the required constraints. Indeed H is sometimes referred to as the *design matrix* in estimation theory. The existence of the inverse of $H^T H$ is the so called *observability condition* which of course depends on the input vector $\mathbf{x}(t)$. The relationship between the parameter estimate covariance and the conditioning of the regressor H can be understood considering the singular value decomposition (SVD) [57] of H

$$\begin{aligned} H &= USV^T \\ H &\in \Re^{n \times p}; U \in \Re^{n \times n}; V \in \Re^{p \times p} : U^T U = I,\ V^T V = I \\ S &= diag(s_1, s_2, \cdots, s_p) \end{aligned}$$

being $s_1, s_2, \cdots, s_p$ the singular values of H. Given this SVD decomposition, from equation (4.6) it follows that

$$\sigma^2_{\hat{\theta}_i} \triangleq (cov(\hat{\boldsymbol{\theta}}_{LS}))_i = (\sigma^2 (H^T H)^{-1})_i = \sigma^2 (S^T S)^{-1}_i = \frac{\sigma^2}{s_i^2}$$

which clearly shows the relationship between the parameter estimate variance, the measurement noise variance σ^2 and the regressor singular values. If $\mathbf{x}(t)$ guarantees $H^T H$ to be nonsingular it is called *persistently exciting* for the model. The degree of excitations provided to a system by an input can be measured by several indicators as the determinant of $H^T H$, or its trace or its condition number. The issue of designing persistently exciting inputs is the topic of a very wide literature a discussion of which goes beyond the scope of this work. For a detailed discussion of such topics refer to [56] [58].

4.1.2 Consistency and Efficiency

The concepts of consistency and efficiency are related to the asymptotic properties of an estimator as functions of the available "information". In particular an estimator, for both a random or deterministic parameter vector, is said to be *consistent* if the estimate converges to the true value in some stochastic sense [59], e.g. in the mean square sense if

$$\lim_{t\to\infty} E[(\hat{\boldsymbol{\theta}} - \boldsymbol{\theta})^T(\hat{\boldsymbol{\theta}} - \boldsymbol{\theta})] = 0$$

where the expectation is taken over $\mathbf{y}$ and $\mathbf{x}$. The concept of efficiency is instead related to the covariance of an estimator. In this regard the covariance of the estimate of either a random or deterministic parameter vector has to satisfy the *Cramer-Rao lower bound* stating that

$$\left(cov(\hat{\boldsymbol{\theta}}) - M^{-1}\right) \text{ is positive semi-definite}$$

or equivalently

$$cov(\hat{\boldsymbol{\theta}}) \geq M^{-1}$$

being M the *Fisher information matrix* defined for the deterministic parameter case as [59]

$$M \triangleq E_{\mathbf{y}}[(\nabla_{\boldsymbol{\theta}} \ln \Lambda_{\mathbf{y}}(\boldsymbol{\theta}))(\nabla_{\boldsymbol{\theta}} \ln \Lambda_{\mathbf{y}}(\boldsymbol{\theta}))^T]|_{\boldsymbol{\theta}=\boldsymbol{\theta}_0} = -E_{\mathbf{y}}[\nabla_{\boldsymbol{\theta}} \nabla_{\boldsymbol{\theta}}^T \ln \Lambda_{\mathbf{y}}(\boldsymbol{\theta})]|_{\boldsymbol{\theta}=\boldsymbol{\theta}_0}$$

being $\Lambda_{\mathbf{y}}(\boldsymbol{\theta}) \triangleq p(\mathbf{y}|\boldsymbol{\theta})$ the likelihood function, $\boldsymbol{\theta}_0$ the value of the unknown deterministic parameter vector, $\nabla_{\boldsymbol{\theta}}$ gradient operator $\nabla_{\boldsymbol{\theta}} \triangleq (\frac{\partial}{\partial\theta_1}, \frac{\partial}{\partial\theta_2}, \cdots, \frac{\partial}{\partial\theta p})^T$ and $\nabla_{\boldsymbol{\theta}} \nabla_{\boldsymbol{\theta}}^T$ the Hessian. The Fisher information matrix of a random parameter vector can be defined as above simply replacing the combined probability density function $p(\mathbf{y}, \boldsymbol{\theta})$ to $\Lambda_{\mathbf{y}}(\boldsymbol{\theta})$. An estimator is said to be *efficient* if its covariance matrix is equal to the inverse of the Fisher information matrix.

4.1.3 On the normal distribution case

If the process $\mathbf{y}$ is normally distributed with mean $H\boldsymbol{\theta}$ and covariance $\sigma^2 I$ the LS estimate is efficient and normally distributed with mean $\hat{\boldsymbol{\theta}}_{LS}$ given by equation (4.5) and covariance (4.6) [56]. The efficiency of the LS estimator in the normal case can be proven thanks to the fact that if $\mathbf{y}$ is normal the likelihood function and the Fisher infor-

mation matrix can be calculated explicitly. The fact that the estimate is itself normally distributed follows from the fact that linear functions of normal variables are normal themselves. This last property is very useful as if the parameter vector is known to be normally distributed with known mean and variance the standard Gaussian hypothesis testing technique [59] may be applied to the overfitting or model selection problem. Overfitting of the data by the model can be detected evaluating the variance of the parameter estimate. Roughly speaking, if the parameter variance is too large the parameter itself is said to be *statistically insignificant* and it might just as well be put to zero. More precisely given the two hypothesis h_0 and h_1:

$$\left.\begin{array}{l} h_0 : \theta_i = 0 \\ h_1 : \theta_i \neq 0 \end{array}\right\} \text{such that } p(\text{accept } h_1 |\ h_0 \text{ true}) = \alpha$$

being θ_i normally distributed with standard deviation σ_{θ_i} and α some arbitrary constant (usually 5%), the h_1 hypothesis is accepted if $\frac{|\theta_i|}{\sigma_{\theta_i}} > c(\alpha)$ being $c = 1.96$ if $\alpha = 5\%$[2]. In percentile notation it can be said that if the parameter relative percentile error is larger then 51.02%, i.e.

$$100\frac{\hat{\sigma}_{\theta_i}}{|\hat{\theta}|} > \frac{100}{1.96}\% = 51.02\ \% \tag{4.11}$$

there is a 95% confidence limit that the parameter itself is statistically insignificant and the hypothesis $h_0 : \theta_i = 0$ is better to be accepted. Moreover in the normal case the measurement variance σ^2 normalized sum of the squared residuals (4.4) $\frac{J_{LS}(\hat{\boldsymbol{\theta}}_{LS})}{\sigma^2} = (\mathbf{y} - H\hat{\boldsymbol{\theta}}_{LS})^T(\mathbf{y} - H\hat{\boldsymbol{\theta}}_{LS})/\sigma^2$ has a $\chi^2(\nu)$ distribution of mean ν and standard deviation $\sqrt{2\nu}$ being $\nu \triangleq dim(\mathbf{y}) - dim(\boldsymbol{\theta})$ the number of degrees of freedom of the fit. As a consequence the value of the normalized cost function $J_{LS}(\hat{\boldsymbol{\theta}}_{LS})/\sigma^2$ can be used to measure quantitatively the goodness of the fit: a rule of thumb for a moderately good fit is that $\chi^2 \approx \nu$. Actually the value of $J_{LS}(\hat{\boldsymbol{\theta}}_{LS})/\sigma^2$ is generally used to test for underfitting as if it is larger then some threshold c, fixed so that the area under the χ^2 distribution between c and infinity is more then $\alpha\%$ being usually $\alpha = 1$ or 5, the data is said to be underfitted by the model. Notice that in order to evaluate underfitting the measurement variance σ^2 must be known. On the contrary, if it is not known, then assuming that the fit is good, the value of $J_{LS}(\hat{\boldsymbol{\theta}}_{LS})$ may be used to estimate the measurement variance σ^2 as shown in the following section. In such circumstance one is not allowed to use $J_{LS}(\hat{\boldsymbol{\theta}}_{LS})$ to asses underfitting anymore.

As far as deterministic models are concerned, i.e. $\mathbf{y}$ has a joint Gaussian distribution with mean $H\boldsymbol{\theta}$ and known covariance Σ, the WLS estimate $\hat{\boldsymbol{\theta}}_{WLS}$ (equation (4.8)) is equivalent to the MLE estimate $\hat{\boldsymbol{\theta}}_{MLE}$ (equation (4.2)). This follows from the fact that

[2] If $\alpha = 5\%$ then c is calculated such that if $N(x,0,1)$ is the normal distribution of x having zero mean and unit variance, $\int_{-c}^{c} N(x,0,1)dx = 1 - \alpha = 0.95 \Rightarrow c = 1.96$

in the given hypothesis the likelihood function $\Lambda_{\mathbf{y}}(\boldsymbol{\theta})$ is

$$\Lambda_{\mathbf{y}}(\boldsymbol{\theta}) = p(\mathbf{y}|\boldsymbol{\theta}) = \frac{1}{\sqrt{(2\pi)^n \det \Sigma}} \exp\{-\frac{1}{2}(\mathbf{y} - H\boldsymbol{\theta})^T \Sigma^{-1} (\mathbf{y} - H\boldsymbol{\theta})\}$$

($n \triangleq \dim(\mathbf{y})$) that is maximized minimizing the exponential argument, i.e. J_{WLS} (4.10). The consistency of the LS, WLS and MLE estimators is a known fact a proof of which may be found in any text book on estimation theory. As far as the efficiency of the MLE estimator is concerned the following theorem is reported from [56]: if an efficient unbiased estimator exists, then it is also the maximum likelihood estimator.

4.1.4 Measurement variance estimation

In order to use equation (4.6) in practice the variance σ^2 of the stochastic process $\mathbf{y}$ must be known. As noticed in the previous footnote (1), if the model H is deterministic such variance is the measurement noise variance which is thus usually known. Nevertheless it is not infrequent that such variance is not known, e.g. if $\mathbf{y}$ is calculated through some other model of unknown reliability, and must be estimated as well. An unbiased estimate of σ^2 is provided by [56]:

$$\hat{\sigma}^2 = \frac{J_{LS}(\hat{\boldsymbol{\theta}}_{LS})}{\dim(\mathbf{y}) - \dim(\boldsymbol{\theta})} = \frac{(\mathbf{y} - H\hat{\boldsymbol{\theta}}_{LS})^T(\mathbf{y} - H\hat{\boldsymbol{\theta}}_{LS})}{\dim(\mathbf{y}) - \dim(\boldsymbol{\theta})} \tag{4.12}$$

In the normal case, i.e. if $\mathbf{y}$ is normally distributed with mean $H\boldsymbol{\theta}$ and variance σ^2, such estimator is optimal in the sense that is a *minimum variance unbiased estimator* (MVUE) for σ^2[56].

4.2 On board sensor based ROV identification

As discussed in the first chapter of this work, the navigation and control systems design of variable configuration ROVs are strictly related to the degree of knowledge of the vehicles dynamic model. As these models are subject to mission dependent changes an on board sensor based system identification approach is highly recommended in order to be able to identify the most important dynamic parameters by simple in water tests rather than complex, time consuming and expensive towing tank techniques. Moreover being the ROV models linear in their parameters a least squares technique will be adopted as the LS estimator has been shown to be either the maximum likelihood one in the Gaussian case, or the best linear unbiased estimator in the more general case. Indeed also other estimation techniques as Kalman filter based ones or estimation error minimization by simulated annealing algorithms have been tested by the author as accounted in [60] [61]. The experimental results regard the identification of a simplified model of the heave, surge, sway and yaw axis of the ROMEO ROV of CNR-IAN. ROMEO

which is depicted in figure (4.1) is about $1m$ in height, $0.9m$ in width and $1.3m$ in length and its weight in air is of about $450Kg$. As shown in figure (4.1) the bottom of the vehicle carries a skid frame for payload and 2 cylindrical canisters for batteries while the upper part is made of a cylindrical canister for the electronics, 4 thrusters for propulsion in the horizontal plane, 4 for the vertical one, several instruments and sensors and, on the top, foam for buoyancy. The thrusters, canisters, and instruments are allocated so that the overall structure of the vehicle is symmetric with respect to both the xz and yz planes.

4.2.1 Model structure

The experimental identification of a complete ROV model as the one given by equation (3.52) is not feasible with only standard on board sensors because it would require a complete state knowledge. Indeed it may be performed with more complex and expensive towing tank facilities as described by Goheen et al.[62] or Fryxell [63], but such approach is not indicated for systems having a variable and mission dependent configuration. Moreover in many standard manoeuvreing conditions, e.g. plane surge motion or vertical translation, and generally at low operating speeds, the coupling terms may be reasonably neglected without serious loss of information. As a consequence on board sensor based identification experiments usually refer to a simplified uncoupled model that can be deduced from equation (3.52) neglecting the off diagonal elements of the added mass matrix, the Coriolis and centripetal kinematic coupling terms and the drag ones. This approximation relies on the facts that *(i)* the off diagonal elements of the added mass matrix of a rigid body having three symmetry planes are identically null [34], *(ii)* the off diagonal elements of such positive definite matrix are much smaller than their diagonal counterparts [32], *(iii)* the hydrodynamic damping coupling is negligeable at low speeds. The resulting model structure for a single degree of freedom is:

$$m\dot{\xi} = -k_\xi \xi - k_{\xi|\xi|}\xi|\xi| + \tau_\xi + \varepsilon \tag{4.13}$$

being m the inertia relative to the considered degree of freedom, ξ the $1D$ velocity (surge, sway, heave, yaw, pitch or roll rate) k_ξ and $k_{\xi|\xi|}$ the linear and quadratic drag coefficients, τ_ξ the applied force or torque and ε a disturbance modelling otherwise unmodeled phenomena as cable effects. This kind of uncoupled model structure is certainly one of the most common in the literature of underwater vehicles: as far as identification experiments are concerned it has been adopted, for example, to identify the yaw motion of the IFREMER VORTEX vehicle [64] or the surge motion of the NPS PHOENIX AUV [65]. Equation (4.13) relative to the heave, surge, sway, and yaw axis of the ROMEO ROV has been experimentally identified as described in the following sections. To estimate the parameter vector $\boldsymbol{\theta} = (m, k_\xi, k_{\xi|\xi|})^T$ from equation (4.13) the torque τ_ξ is assumed known and a linear regressor is considered. The knowledge of τ_ξ is actually related to the fact that the relation between applied thruster voltage and torque has been a priori identified for each single thruster in a thrust tunnel as de-

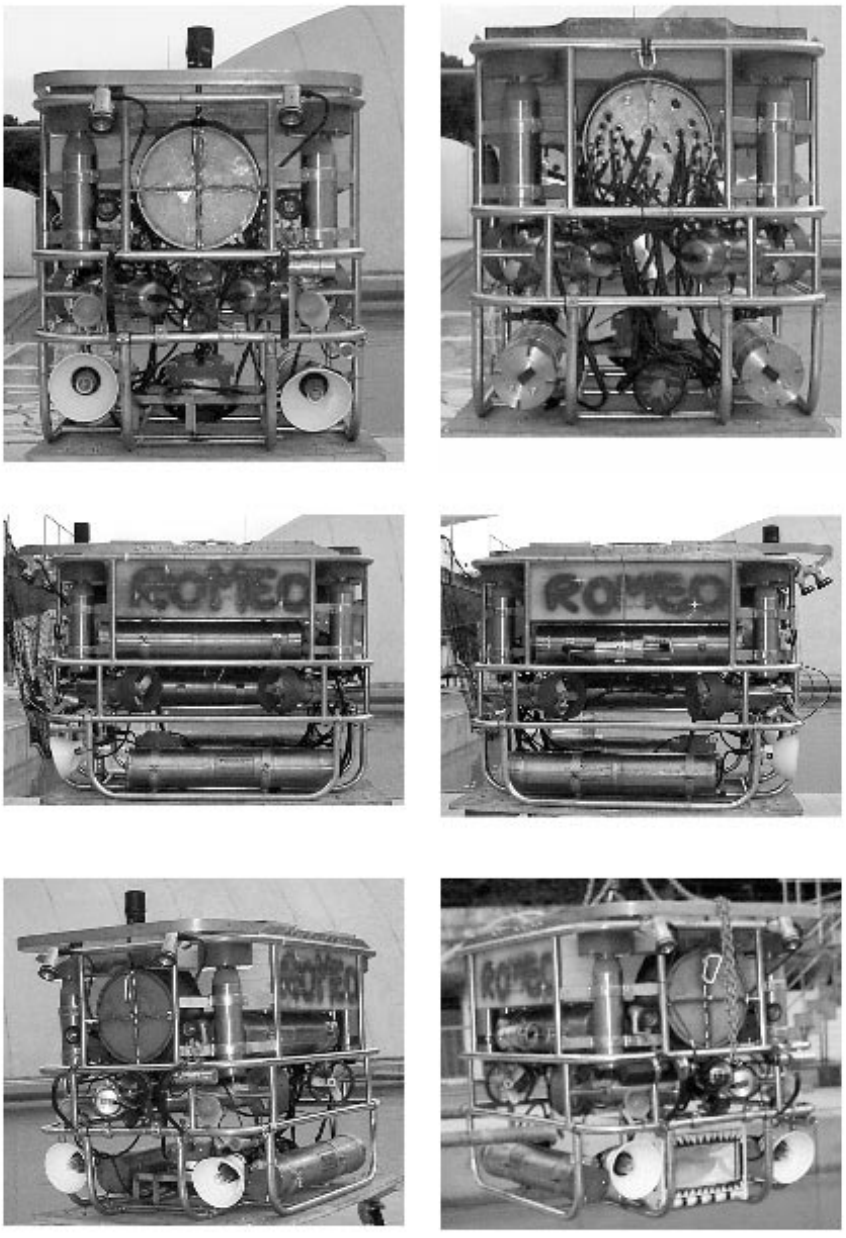

4.1.ROMEO: the bottom right pictures shows a different payload configuration, a palnkton sampling equipment

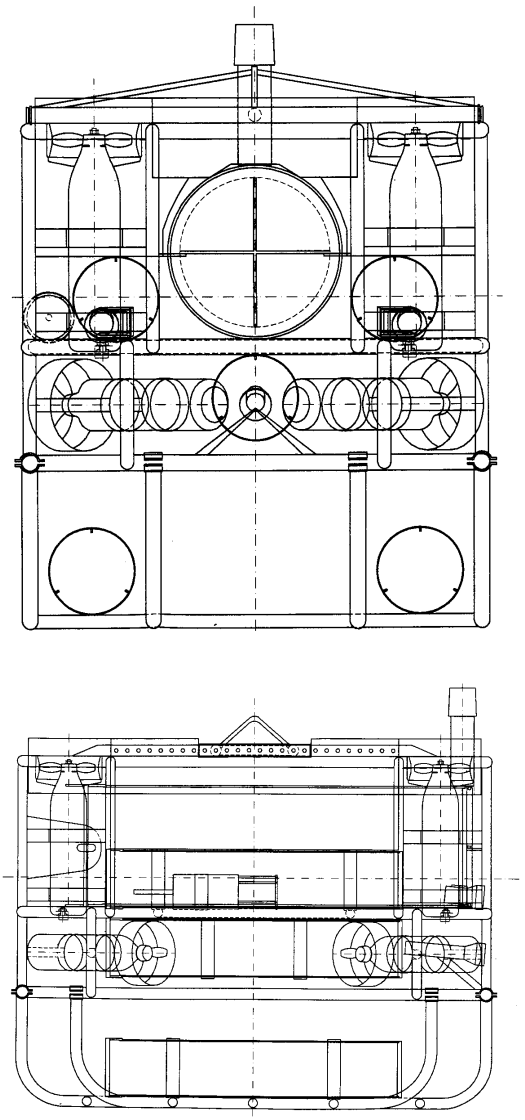

4.2.The ROMEO ROV

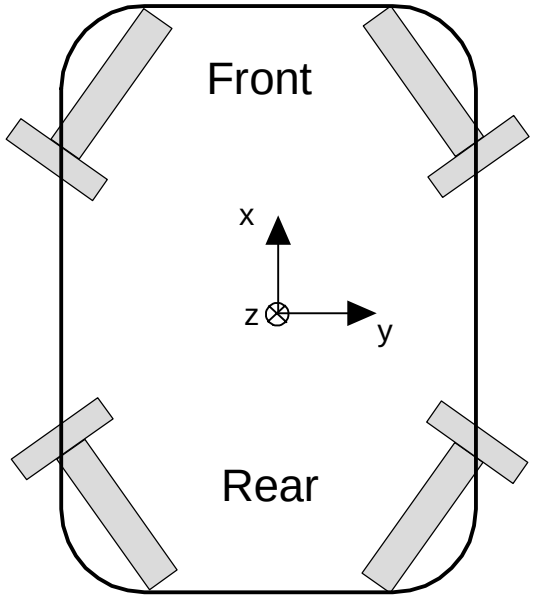

4.3.Sketched top view of ROMEOs horizontal thruster configuration.

scribed in the following section. A potentially serious drawback of such methods could be related to the fact that the identified thruster model does not take into account the propeller-propeller or propeller-hull interactions that occur on the vehicle in the operating conditions. These phenomena are due to the fact that on the great majority of ROVs more thrusters (8 on ROMEO) are present on the vehicle and may thus interfere between themselves or with the hull. As far as the ROMEO ROV is concerned this can be more easily understood with reference to figure (4.3) in which the horizontal thruster disposition is schematically depicted. If all four thrusters operate at the same time, it is reasonable to expect that the front and rear ones on the same side of the vehicle interfere with each other. It is also expected that the front ones will experience a propeller hull interaction pushing backwards as the rear ones pushing forward. As a consequence the efficiency of the thrusters is expected to be less then the one measured in the thrust tunnel. As will be described in the following sections, to model this phenomena an efficiency parameter has been introduced. This technique has been shown to be effective for the modeling of both the propeller-propeller interactions and the propeller hull ones. The experimental results reported in the following show that the propeller-hull and propeller-propeller interactions have indeed a most relevant effect on ROV dynamics. Nevertheless this topic has not been systematically addressed by the underwater robotics scientific community: to the knowledge of the author the only relevant reference to this phenomenon in ROV systems is due Goheen and Jefferys [66] who describe a *thruster installation coefficient*. In their words [66] the installation coefficient takes "*into account the differences in force that the thruster provides when it is operating in the proximity of the ROV, as opposed to when it is tested in open water*".

At last notice that in order to estimate $\boldsymbol{\theta} = (m, k_\xi, k_{\xi|\xi|})^T$ and the eventual efficiency parameters a two step procedure has been implemented: first a the drag and efficiency coefficients are estimated by constant velocity experiments, then with the aid of their knowledge a sinusoidal torque input is designed in order to identify the inertia m.

4.2.2 Thruster model identification

The modelling and control of underwater vehicle thruster systems has received a wide attention in the literature of the last years [45] [46] [44]. As shown by Yoerger et. al.[44], within the theory of ideal fluids a lumped parameter thruster model is given by (section (3.3.1))

$$\begin{aligned} \tau &= C_t n|n| \\ \dot{n} &= \beta T - \alpha n|n| \end{aligned}$$

being τ the output thruster force, C_t, β and α constant parameters, n the propeller revolution rate and T the input torque. Generally the servo velocity loop of the velocity controlled thruster system has a negligible time constant with respect to the overall vehicles' one [19], and thus the thruster dynamics can be neglected. Indeed most often [32]

the applied thrust is modeled as $\tau = C_t|n|n - C_s|n|v$ being v the velocity of the fluid through the thruster (*velocity of advance*) and $-C_s|n|v$ a saturation term. In virtue of the creeping motion of UUVs, this last saturation term can be neglected in many standard operational conditions as widely accepted in the literature [32] [14] [44] [64]. Moreover in steady state conditions the neglected thrust drag term $-C_s|n|v$ will be somehow taken into account by the drag forces considered in the equation of motion (4.13) of the vehicle. Thus, neglecting the motor dynamics, the thruster force may be modelled as

$$\tau = CV|V| \tag{4.14}$$

being C an unknown constant and V the applied control voltage. In many marine applications two different C parameters are requested for the positive and negative propeller revolution rates, as the thrusters do not behave symmetrically in the two directions, but most frequently UUV propellers, as ROMEOs ones, are designed to exhibit a symmetrical behaviour in the two directions. Equation (4.14) has been identified [67] for each of the eight ROMEO thrusters putting the whole thruster (motor and propeller) in a thrust tunnel (figure (4.4)) and measuring the force τ as a function of the input voltage V. Typical results of this measuring and identification method are shown in figure (4.5). It should be noticed that having neglected the velocity of advance, the proposed model is expected to be more accurate far from the propeller revolution rate inversion points. In particular high frequency sign changes of n, that may occur during hovering manoeuvres or would occur with pseudo random binary inputs typical of identification experiments, produce unmodeled turbulence next to the thrusters making the output thrust computed by the standard model less accurate.

4.2.3 Off line velocity estimation

As stated above, the proposed identification scheme consists in two steps: first the drag coefficients are estimated by constant velocity tests, and then their values are adopted to design a suboptimal inertia identification experiment with a sinusoidal input. Both steps are based on position measurements only so that a major issue is velocity estimation. As far as the drag experiments are concerned a simple least squares fitting of the position data is enough, but for the inertia identification tests a different filtering technique is required. More generally the problem of computing the numerical derivative of a signal given noisy samples is posed. Among the many possible signal processing techniques to face this problem attention is focused on the use of the Savitzky-Golay filters [68]. These are low pass filters designed in the time domain rather then in frequency domain. Within a moving window containing n_l points on the left and n_r on the right of the i^{th} data sample, the $n_l + n_r + 1$ points are least squares fitted with a polynomial of degree m and the filtered value of the i^{th} data sample is assumed to be the value of the polynomial in i. The derivative of the given signal in i is thus assumed to be the derivative of the polynomial in i. Notice that the fitted polynomial is adopted in the i^{th} point only, as when the moving window is shifted of one point the whole procedure is

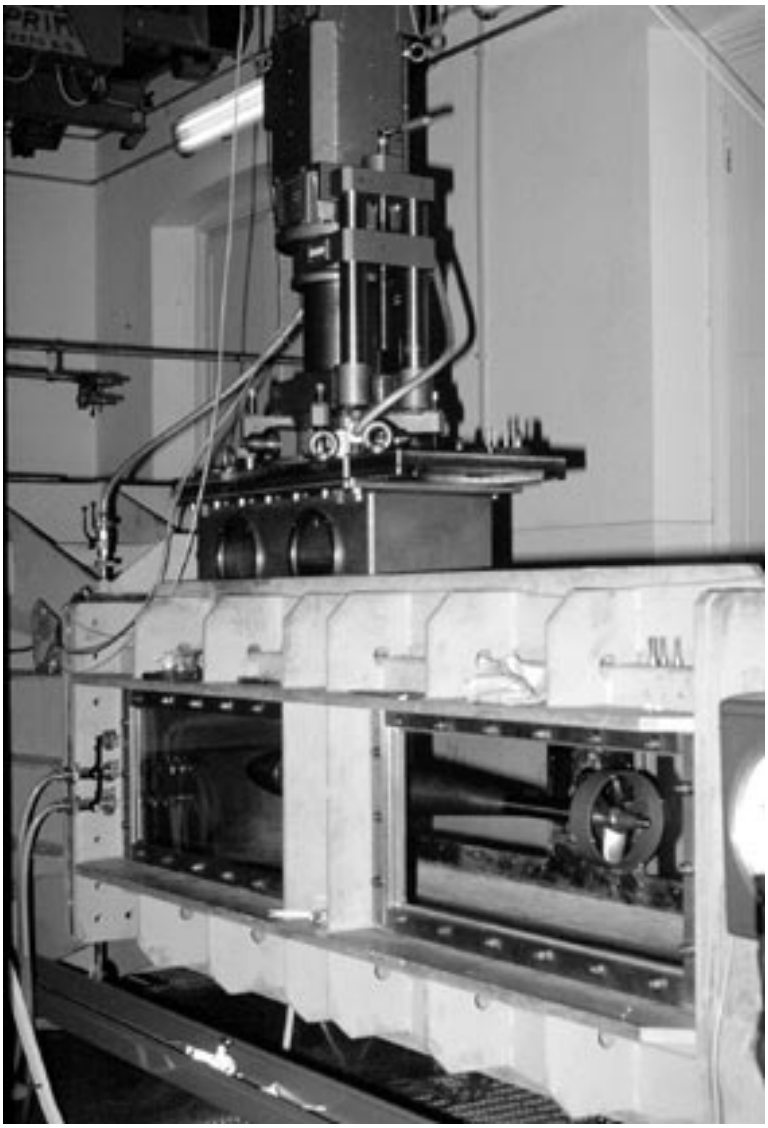

4.4.Cavitation tunnel tests: preliminary propeller test. The thruster identification has been carried out putting the whole thruster in the tunnel.

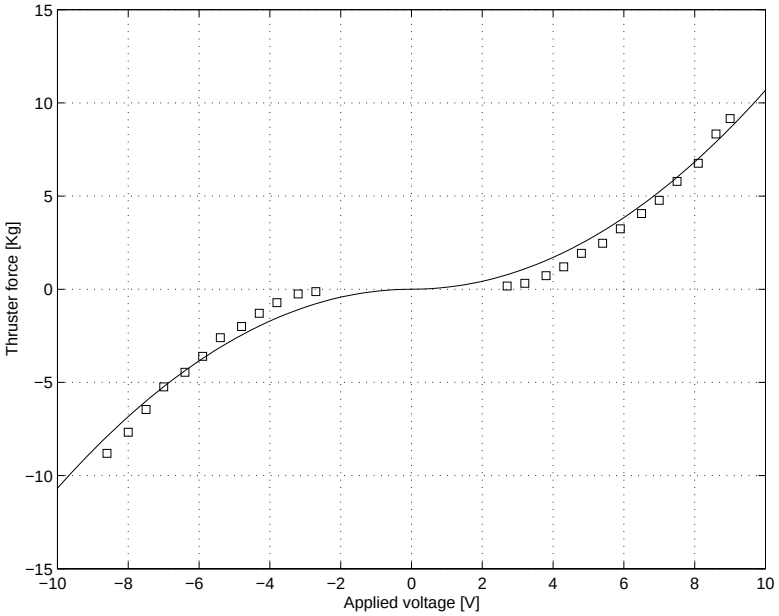

4.5.Cavitation tunnel identification tests.

repeated. In order to design a Savitzky-Golay filter the windows left and right lengths n_l, n_r and the polynomial degree m must be chosen. If the data is processed off line n_r can be chosen to be non null so that the filter is non-causal: as far as the polynomial degree m is concerned it can be chosen adaptively as proposed in [69], but generally [68] m is fixed to 2 or 4. For most applications the moving window can be chosen to be symmetrical ($n_l = n_r$): guidelines for the choice of n_l and n_r may be found in [68]. Savitzky-Golay filters, that are most common among the chemists for noisy spectrometric data analysis, are among the most "natural" tools for derivative estimation. A detailed analysis of their properties goes beyond the scopes of this work, yet to have a qualitative understanding of their performance an example based on the equations of our interest is reported: consider the linear system

$$\begin{aligned} m\ddot{x} &= f - k_l\dot{x} \\ \text{being} \quad &: \quad f = f_0 + \Delta_f \sin(\omega t) \end{aligned}$$

By direct calculation it follows that

$$\begin{aligned} \dot{x} &= x_0 e^{-t/\tau} + \frac{f_0}{k_l}(1 - e^{-t/\tau}) + \frac{\Delta_f}{k_l}\frac{\sin(\omega t) - \omega\tau(\cos(\omega t) - 1)}{(1 + \omega^2\tau^2)} \\ x &= \tau(x_0 - \frac{f_0}{k_l})(1 - e^{-t/\tau}) + \frac{f_0}{k_l}t + \frac{\Delta_f}{k_l}\frac{\omega\tau t - \tau\sin(\omega t) - \frac{1}{\omega}\cos(\omega t) + \frac{1}{\omega}}{(1 + \omega^2\tau^2)} \\ \text{being} \quad &: \quad \tau = m/k_l \end{aligned}$$

Assuming $f_0 = 35$, $\Delta_f = 25$, $\omega = 0.1963$, $m = 500$, $k_l = 170$, $x_0 = 0$, the position x on a $180s$ test evolves as shown in the top plot of figure (4.6) having adopted a $3Hz$ sampling rate, i.e. 540 data samples. Adding to this signal the zero mean normal noise having 0.07 standard deviation shown in the bottom plot of figure (4.6) and filtering the so computed noise corrupted position signal with a 4^{th} order Savitzky-Golay filter having $n_l = n_r = 10$ yields the result displayed in figure (4.7).

4.2.4 Heave model identification

As far as the heave axis is concerned, off-line identification has been performed to estimate linear and quadratic drag coefficients and buoyancy force [70]. The data for the identification experiments consists in depth and thrust measurements collected during up and down motions performed under the Antarctica ice-canopy during the XIII Italian Antarctica Expedition (1997-1998). Depth was measured directly by a depth-meter with a $10Hz$ sampling rate, while thrust was estimated by the thrust-tunnel identified model described in the previous subsection. Five different experiments, in the sequel labelled with numbers 1 to 5, have been performed with inputs of the kind shown in figure (4.8) each with a different vehicle weight. During experiment 1 and 2 the vehicle was positive, during experiment 3 it was roughly neutral and in the last two it was

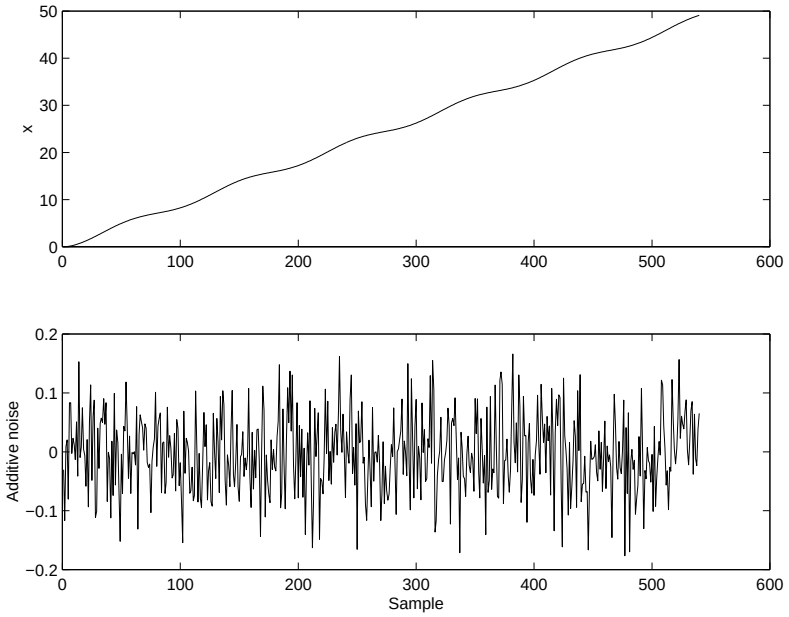

4.6.Above: analytical position signal. Below: additive, zero mean, normal noise having standard deviation 0.07.

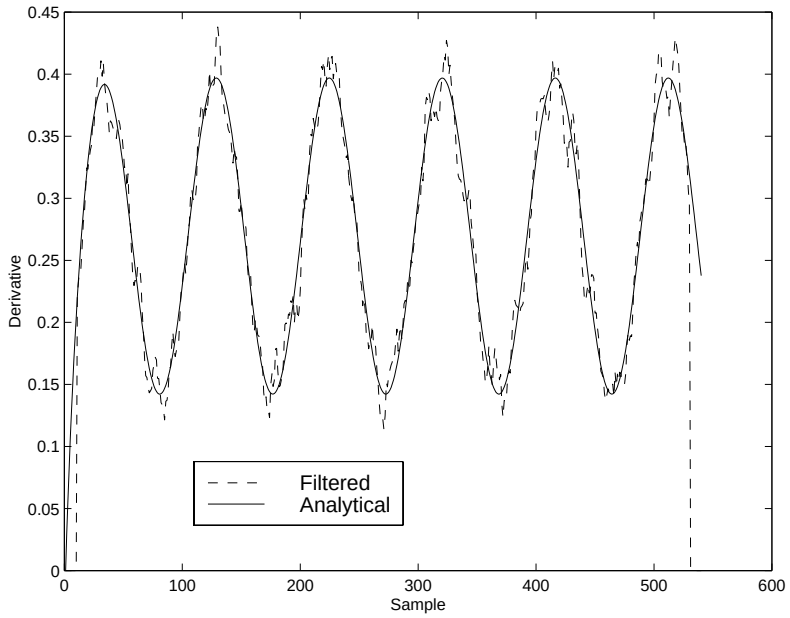

4.7.Estimated and real velocity $\dot{x}$.

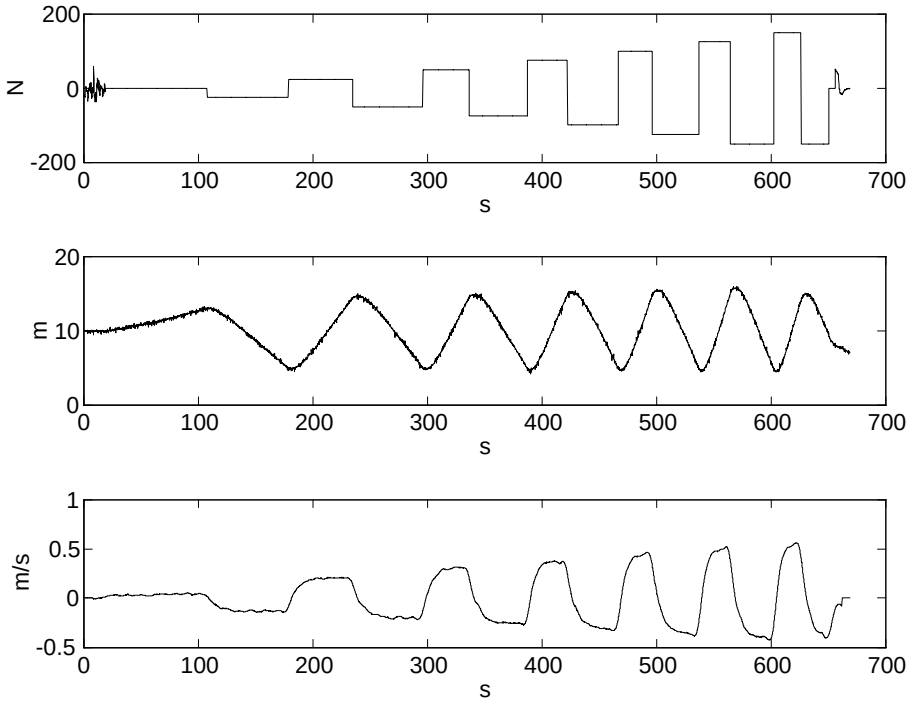

4.8.From top to bottom: Torque, heave position and velocity with respect to time for experiment 3

negative. Weight was changed adding on ROMEOs top, during each experiment, one diver's lead weight which reasonably does not affect the hydrodynamic derivatives but only the overall weight of the system. During all experiments the heading of the vehicle was kept constant by the action of the heading autopilot. This suggests that momentum drag due to the horizontal thrusters could be present and should be taken into account. The heave velocity has been calculated off-line processing the depth signal with a non-causal Savitzky-Golay polynomial [68] filter of fourth order with a symmetric moving window of 141 points. As only the stationary values of the velocities were needed for the identification process, these have been calculated averaging the velocity signal far from the inversion points to exclude the non stationary system response at each inversion on one side, and the last 70 samples of each constant input zone that could introduce bias in the estimated velocity, on the other. The heave motion is described with respect to a body fixed reference frame having its z axis pointing downward; indicating with $\mathbf{w}$ the heave velocity, with $\mathbf{F}$ the thruster applied force, with $\mathbf{W}$ the weight and buoyancy force, with m the sum of inertial and added mass, with $k_{\mathbf{w}}$ and $k_{\mathbf{w}|\mathbf{w}|}$ the linear and quadratic drag coefficients according to subsection (4.2.1) the standard heave model is:

$$m\,\dot{\mathbf{w}} = -k_{\mathbf{w}}\,\mathbf{w} - k_{\mathbf{w}|\mathbf{w}|}\,\mathbf{w}|\mathbf{w}| + \mathbf{F} + \mathbf{W} \tag{4.15}$$

where $\mathbf{w}$ and $\mathbf{F}$ are assumed to be known far from the inversion points, i.e., in stationary conditions $\dot{\mathbf{w}} = 0$. Equation (4.15) is linear in the unknown parameters and, calling $\mathbf{e}_z$ the z axis unit vector, when $\dot{\mathbf{w}} = 0$ it can be written in the more convenient form $\mathbf{y}_s = H_s\,\boldsymbol{\theta}_s + \boldsymbol{\varepsilon}_s$ being $\boldsymbol{\theta}_s = [k_{\mathbf{w}}\ k_{\mathbf{w}|\mathbf{w}|}\ (\mathbf{W}^T\mathbf{e}_z)]^T$ the parameter vector, $\mathbf{y}_s = [\mathbf{F}_1^T\mathbf{e}_z\ \mathbf{F}_2^T\mathbf{e}_z\ \cdots \mathbf{F}_m^T\mathbf{e}_z]^T$ the measurement vector, $H_s = \begin{bmatrix} \mathbf{w}_1^T\mathbf{e}_z & \mathbf{w}_1^T\mathbf{e}_z|\mathbf{w}_1| & -1 \\ \mathbf{w}_2^T\mathbf{e}_z & \mathbf{w}_2^T\mathbf{e}_z|\mathbf{w}_2| & -1 \\ \vdots & \vdots & \vdots \\ \mathbf{w}_m^T\mathbf{e}_z & \mathbf{w}_m^T\mathbf{e}_z|\mathbf{w}_m| & -1 \end{bmatrix}$ the regression matrix and $\boldsymbol{\varepsilon}_s$ the measurement noise. Each stationary velocity $\mathbf{w}_i$ is calculated as described above. As shown in the pictures in figure (4.1) the vertical propellers of the ROMEO ROV are at the very top of the frame in order to avoid large turbulence next to the sea bottom that could limit visibility in the presence of sand or dust. As a consequence when the vertical thrusters push upwards the water flow out of the propellers interferes with the vehicles structure. It is then reasonable to assume that when the thrusters' force is directed upwards the efficiency of the vertical thrusters will be affected by a propeller-hull interaction virtually absent when the force is directed downwards. This suggests to modify equation (4.15) with the introduction of an efficiency parameter η such that in stationary conditions the vehicles model can be written as

$$\begin{aligned} \eta\,\mathbf{F} &= k_{\mathbf{w}}\,\mathbf{w} + k_{\mathbf{w}|\mathbf{w}|}\,\mathbf{w}|\mathbf{w}| - \mathbf{W} \\ &\begin{cases} \eta = 1 \;\forall\, \mathbf{F}^T\mathbf{e}_z \geq 0 \\ \eta < 1 \;\forall\, \mathbf{F}^T\mathbf{e}_z < 0 \end{cases} \end{aligned} \tag{4.16}$$

($\mathbf{e}_z$ is the z-axis unit vector pointing downwards) which will be called *eta* model in the sequel. Indicating with the subscripts d and u forces and velocities in the downward and upward directions, the regression form of equation (4.16) can be written as

$$\mathbf{y}_\eta = H_\eta\,\boldsymbol{\theta}_\eta + \boldsymbol{\varepsilon}_\eta$$

$$\mathbf{y}_\eta = [\mathbf{F}_{d1}^T\mathbf{e}_z\ \mathbf{F}_{d2}^T\mathbf{e}_z\ \cdots\ \mathbf{F}_{dm}^T\mathbf{e}_z\ 0\ 0\ \cdots 0]^T \in \Re^{(m+p)\times 1}$$

$$H_\eta = \begin{bmatrix} \mathbf{w}_{d1}^T\mathbf{e}_z & \mathbf{w}_{d1}^T\mathbf{e}_z|\mathbf{w}_{d1}| & -1 & 0 \\ \vdots & \vdots & \vdots & \vdots \\ \mathbf{w}_{dm}^T\mathbf{e}_z & \mathbf{w}_{dm}^T\mathbf{e}_z|\mathbf{w}_{dm}| & -1 & 0 \\ -\mathbf{w}_{u1}^T\mathbf{e}_z & -\mathbf{w}_{u1}^T\mathbf{e}_z|\mathbf{w}_{u1}| & 1 & \mathbf{F}_{u1}^T\mathbf{e}_z \\ \vdots & \vdots & \vdots & \vdots \\ -\mathbf{w}_{up}^T\mathbf{e}_z & -\mathbf{w}_{up}^T\mathbf{e}_z|\mathbf{w}_{up}| & 1 & \mathbf{F}_{up}^T\mathbf{e}_z \end{bmatrix} = \begin{bmatrix} w_{d1} & w_{d1}^2 & -1 & 0 \\ \vdots & \vdots & \vdots & \vdots \\ w_{dm} & w_{dm}^2 & -1 & 0 \\ w_{u1} & w_{u1}^2 & 1 & -F_{u1} \\ \vdots & \vdots & \vdots & \vdots \\ w_{up} & w_{up}^2 & 1 & -F_{up} \end{bmatrix}$$

$$\boldsymbol{\theta}_\eta = [k_{\mathbf{w}}\ k_{\mathbf{w}|\mathbf{w}|}\ (\mathbf{W}^T\mathbf{e}_z)\ \eta]^T$$

being w and F the norms of vectors $\mathbf{w}$ and $\mathbf{F}$ following the standard notation $a \triangleq \|\mathbf{a}\|$. The third and last considered model takes explicitly into account the momentum drag discussed in section (3.3.1). As during all the experiments the heading of the vehicle was kept constant with the horizontal thrusters, their effect on the heave drag may be modelled by $\mathbf{F}_{md} = -\alpha\ n_h \mathbf{w}$ where n_h is the mean propeller revolution rate modulus of the four horizontal thrusters, α is an unknown constant parameter and $\mathbf{w}$ the heave velocity. Adding $\mathbf{F}_{md}$ in equation (4.16) gives rise to the *eta-md* model which can be written in regression form as

$$\eta\,\mathbf{F} = k_{\mathbf{w}}\,\mathbf{w} + k_{\mathbf{w}|\mathbf{w}|}\,\mathbf{w}|\mathbf{w}| - \mathbf{W} + \alpha\ n_h \mathbf{w} \ : \begin{cases} \eta = 1\ \forall\ \mathbf{F}^T\mathbf{e}_z \geq 0 \\ \eta < 1\ \forall\ \mathbf{F}^T\mathbf{e}_z < 0 \end{cases}$$

$$\mathbf{y}_{md} = H_{md}\boldsymbol{\theta}_{md} + \boldsymbol{\varepsilon}_{md}$$

$$\mathbf{y}_{md} = [\mathbf{F}_{d1}^T\mathbf{e}_z\ \mathbf{F}_{d2}^T\mathbf{e}_z\ \cdots\ \mathbf{F}_{dm}^T\mathbf{e}_z\ 0\ 0\ \cdots 0]^T \in R^{(m+p)\times 1}$$

$$H_{md} = \begin{bmatrix} \mathbf{w}_{d1}^T\mathbf{e}_z & \mathbf{w}_{d1}^T\mathbf{e}_z|\mathbf{w}_{d1}| & -1 & 0 & n_{h1}\mathbf{w}_{d1}^T\mathbf{e}_z \\ \vdots & \vdots & \vdots & \vdots & \vdots \\ \mathbf{w}_{dm}^T\mathbf{e}_z & \mathbf{w}_{dm}^T\mathbf{e}_z|\mathbf{w}_{dm}| & -1 & 0 & n_{hm}\mathbf{w}_{dm}^T\mathbf{e}_z \\ -\mathbf{w}_{u1}^T\mathbf{e}_z & -\mathbf{w}_{u1}^T\mathbf{e}_z|\mathbf{w}_{u1}| & 1 & \mathbf{F}_{u1}^T\mathbf{e}_z & -n_{u1}\mathbf{w}_{u1}^T\mathbf{e}_z \\ \vdots & \vdots & \vdots & \vdots & \vdots \\ -\mathbf{w}_{up}^T\mathbf{e}_z & -\mathbf{w}_{up}^T\mathbf{e}_z|\mathbf{w}_{up}| & 1 & \mathbf{F}_{up}^T\mathbf{e}_z & -n_{up}\mathbf{w}_{up}^T\mathbf{e}_z \end{bmatrix} =$$

$$= \begin{bmatrix} w_{d1} & w_{d1}^2 & -1 & 0 & n_{h1}\,w_{d1} \\ \vdots & \vdots & \vdots & \vdots & \vdots \\ w_{dm} & w_{dm}^2 & -1 & 0 & n_{hm}\,w_{dm} \\ w_{u1} & w_{u1}^2 & 1 & -F_{u1} & n_{u1}\,w_{u1} \\ \vdots & \vdots & \vdots & \vdots & \vdots \\ w_{up} & w_{up}^2 & 1 & -F_{up} & n_{up}\,w_{up} \end{bmatrix}$$

$$\boldsymbol{\theta}_{md} = [k_{\mathbf{w}}\ k_{\mathbf{w}|\mathbf{w}|}\ (\mathbf{W}^T\mathbf{e}_z)\ \eta\ \alpha]^T$$

Typical values of m and p range from 4 to 7. The identification of the above models has been performed by the standard least squares technique described in the previous section. In particular indicating with $\mathbf{y} = H\boldsymbol{\theta} + \boldsymbol{\varepsilon}$ the generic heave model, the covariance matrix Σ of the noise vectors $\boldsymbol{\varepsilon}$ is considered unknown as the measurement vector $\mathbf{y}$ is actually calculated through another identified model. Assuming $\Sigma = \sigma_\varepsilon^2\ I$ being σ_ε an unknown constant and I the identity matrix equations (4.5), (4.6) and (4.12) may be applied. All the parameter values and relative standard deviations presented in

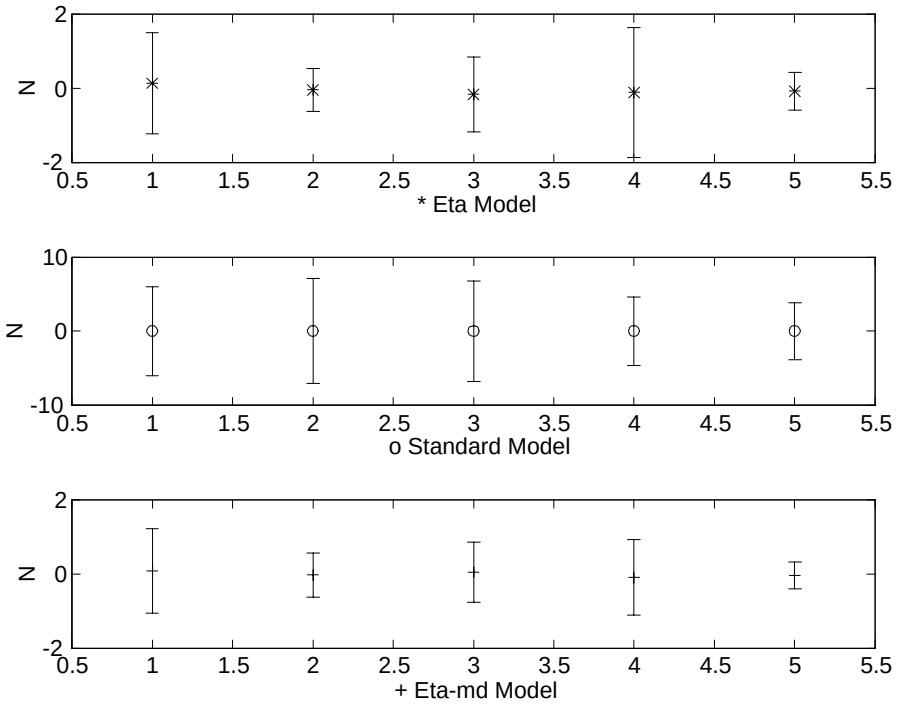

4.9.Model residuals (N) and relative estimated standard deviation for the 5 experiments

following tables and figures have been calculated respectively as $\hat{\boldsymbol{\theta}}_{LS}$ given by equation (4.5), and the square root of the principal diagonal of matrix $(H^T H)^{-1}\hat{\sigma}_\varepsilon^2$, i.e. $\hat{\sigma}_{\boldsymbol{\theta}} = \sqrt{diag((H^T H)^{-1}\hat{\sigma}_\varepsilon^2)}$ being $\hat{\sigma}_\varepsilon^2$ given by equation (4.12). As shown in figure (4.9) all the models perform well as far as the mean value of the residuals $\mathbf{y} - H\hat{\boldsymbol{\theta}}$ is concerned, but indeed the estimated standard deviation $\hat{\sigma}_\varepsilon$ of the standard model residuals is from 3 to 10 times larger then for the eta or eta-md models. In figures (4.10) and (4.11) the linear and quadratic drag coefficients are plotted for the different models and experiments. The extremum values of the coefficients relative to the eta-md model, which has the smallest variation on the 5 tests with respect to the other two models, are reported by dashed lines. The scattered nature of the linear and quadratic drag coefficients shown in figures (4.10) and (4.11) for the standard model suggests a mismodelling error which is partially corrected in the other models that predict much more stable values of $k_{\mathbf{w}}$ and $k_{\mathbf{w}|\mathbf{w}|}$. In figure (4.12) the buoyancy force estimate for the different models is reported. Notice that while the eta-md and eta models are in perfect agreement on $\mathbf{W}$s estimate, the standard model is affected by a bias on $\mathbf{W}$ such that the vehicles results positively buoyant in all 5 tests, which is false[3]. This behaviour of

[3] The vehicle was neutrally buoyant during experiment 3, positive during experiments 1 and 2 and negative during experiments 4 and 5.

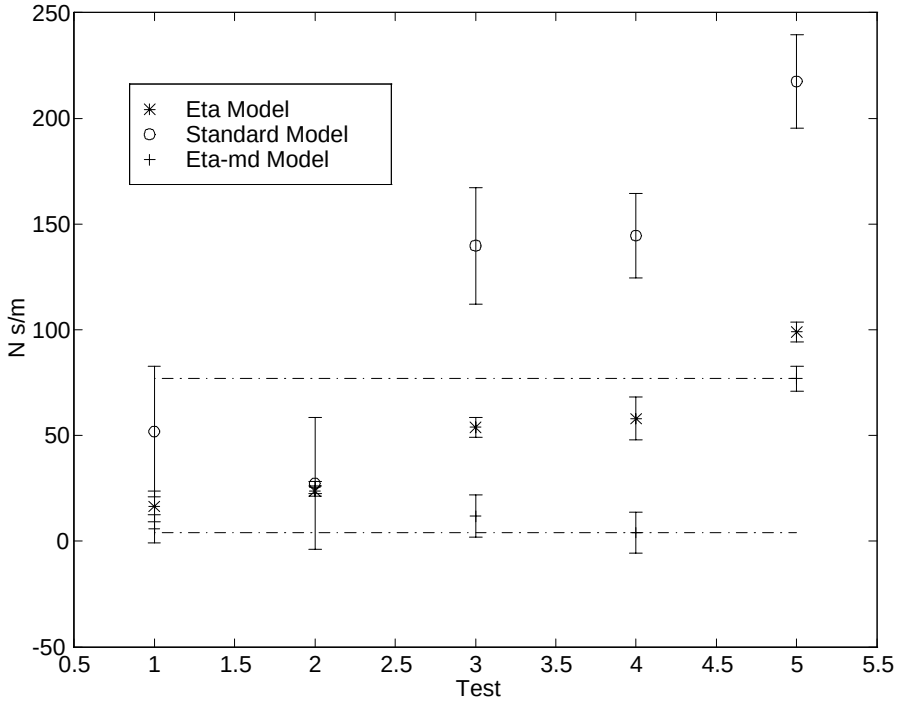

4.10.Linear drag coefficient $k_{\mathbf{w}}(Ns/m)$ for the three models in the five experiments. The dashed lines show the limits of the $k_{\mathbf{w}}$ eta-md estimate on the 5 experiments. The ranges of the other two models are larger.

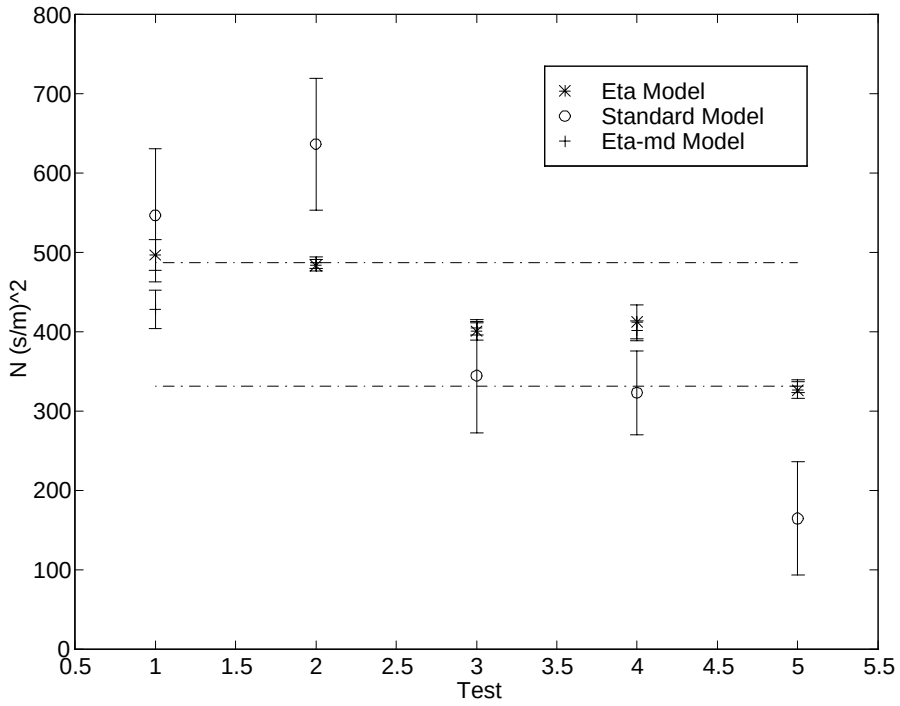

4.11.Quadratic drag coefficient $k_{\mathbf{w}|\mathbf{w}|}\,(Ns^2/m^2)$ for the three models in the five experiments. The dashed lines show the limit of the $k_{\mathbf{w}|\mathbf{w}|}$ eta-md estimate on the 5 experiments. The ranges of the other two models are larger.

the standard model is due to the fact that neglecting the propeller-hull interaction, the standard model over-estimates the applied upward force and tries thus to compensate it with a large weight. Table I reports the maximum and minimum percentile relative error $\frac{\Delta\hat{\theta}}{\theta} \triangleq 100\frac{\hat{\sigma}_\theta}{|\hat{\theta}|}$ of each parameter, for the three suggested models on the 5 tests. Both the estimate of the parameter and its standard deviation have been calculated as described above.

Table I		Standard	Eta	Eta-md
Max	$\frac{\Delta k_{\mathbf{w}}}{k_{\mathbf{w}}}$	$228\ \%$	$87.2\ \%$	$475.1\ \%$
Min	$\frac{\Delta k_{\mathbf{w}}}{k_{\mathbf{w}}}$	$20.3\ \%$	$9.5\ \%$	$15.4\ \%$
Max	$\frac{\Delta k_{\mathbf{w}\|\mathbf{w}\|}}{k_{\mathbf{w}\|\mathbf{w}\|}}$	$86.9\ \%$	$10.3\ \%$	$11.2\ \%$
Min	$\frac{\Delta k_{\mathbf{w}\|\mathbf{w}\|}}{k_{\mathbf{w}\|\mathbf{w}\|}}$	$26.2\ \%$	$2.9\ \%$	$3.1\ \%$
Max	$\frac{\Delta \mathbf{W}}{\mathbf{W}}$	$151\ \%$	$66.4\ \%$	$37.4\ \%$
Min	$\frac{\Delta \mathbf{W}}{\mathbf{W}}$	$8.8\ \%$	$7.6\ \%$	$5.7\ \%$
Max	$\frac{\Delta \eta}{\eta}$	$\diagup$	$10.5\ \%$	$10.9\ \%$
Min	$\frac{\Delta \eta}{\eta}$	$\diagup$	$2.1\ \%$	$3.3\ \%$
Max	$\frac{\Delta \alpha}{\alpha}$	$\diagup$	$\diagup$	$125.7\ \%$
Min	$\frac{\Delta \alpha}{\alpha}$	$\diagup$	$\diagup$	$28\ \%$

Table I shows that the eta model predicts the most stable parameter values of the three. The extremely imprecise estimates of the momentum drag ($\hat{\alpha}$ of test 2 is negative!) and linear drag parameters in the eta-md model indicate that the first and last columns of the regression matrix H_{md} must share large parallel components. This is due to the fact that the modulus of the revolution rate of the horizontal thrusters n_h is very similar at the different speed regimes considered. Moreover, the poor performance of the eta-md model is clearly shown in figure (4.13) by the very scattered estimate of η on the five tests as compared to the eta model. The plane and dashed lines in figure (4.13) represent the mean value of η according to the eta and eta-md models. Concluding, the results reported in Table I and in the above plots suggest that the best model among the three is the eta model. This means that during common slow motion heave maneuvers of the ROMEO open frame ROV momentum drag forces (3.3.1) due to the propeller revolution rate of the horizontal thrusters can be modelled by the standard linear and quadratic drag forces. On the contrary propeller hull interactions are relevant and need to be modeled separately by an efficiency parameter. The above reported experimental results show that the loss of efficiency due to the propeller hull interaction in the heave direction is more then 40% ($\eta_{md} = 0.57$). The numerical values of the estimated parameters and

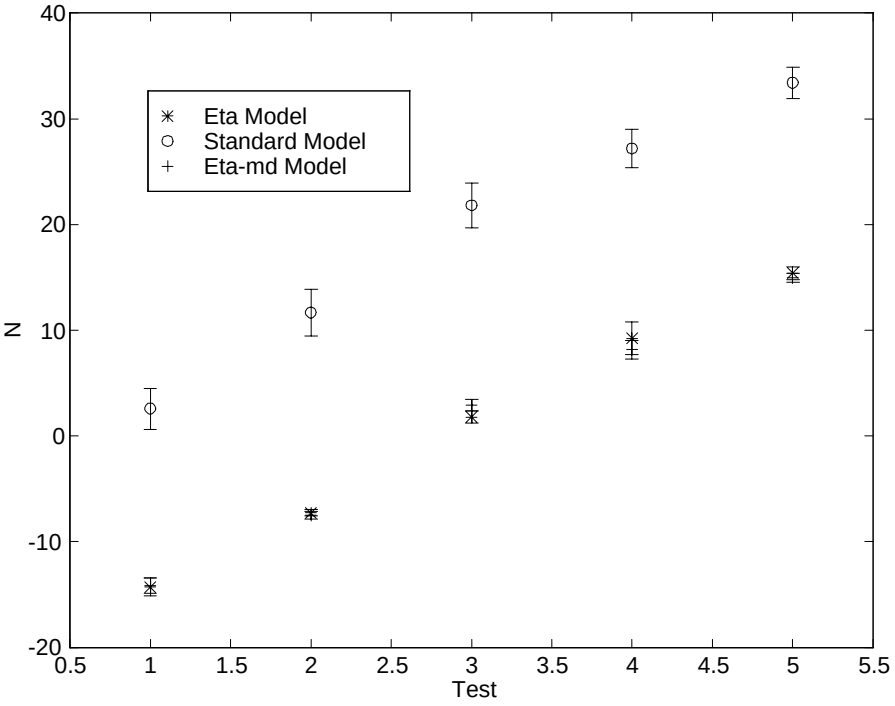

4.12.Buoyancy force $W(N)$ estimate for the three models in the five tests.

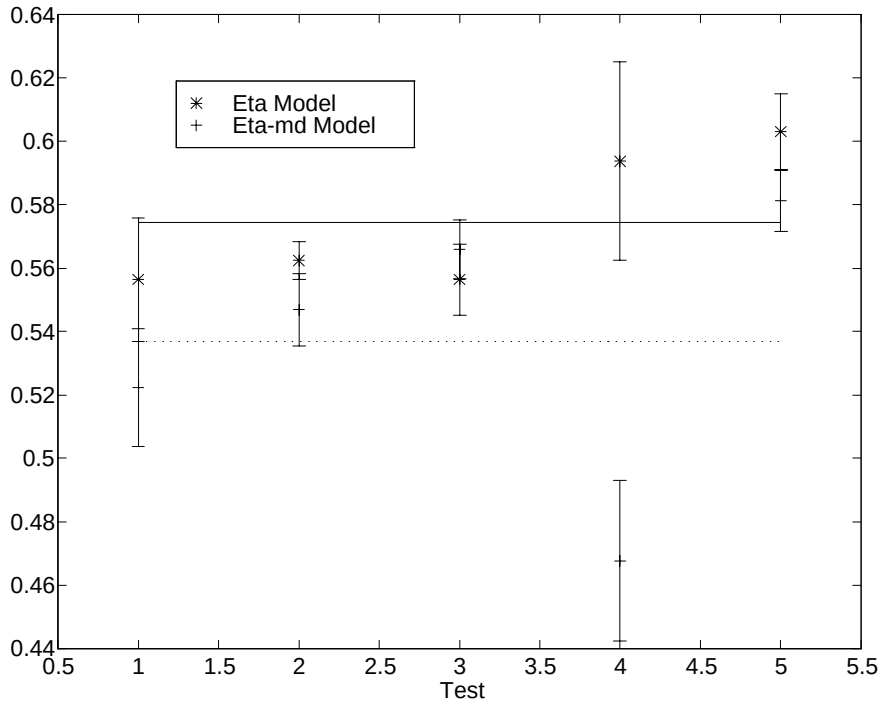

4.13.Efficiency η parameter estimate. The solid and dashed lines are the mean values of η according to the eta and eta-md models.

their standard deviation for the three models are reported in the following:

$$
\begin{array}{ll}
\text{Model type} & \text{Parameter values} \\
\text{Eta} & \left\{ \begin{array}{rr} k_{\mathbf{w}} = & (50 \pm 12)\ Ns/m \\ k_{\mathbf{w}|\mathbf{w}|} = & (424 \pm 28)\ Ns^2/m^2 \\ \eta = & 0.57 \pm 0.03 \end{array} \right. \\
\text{Eta-md} & \left\{ \begin{array}{rr} k_{\mathbf{w}} = & (25 \pm 14)\ Ns/m \\ k_{\mathbf{w}|\mathbf{w}|} = & (411 \pm 24)\ Ns^2/m^2 \\ \eta = & 0.54 \pm 0.03 \\ \alpha = & 15 \pm 8 \end{array} \right. \\
\text{Standard} & \left\{ \begin{array}{rr} k_{\mathbf{w}} = & (116 \pm 53)\ Ns/m \\ k_{\mathbf{w}|\mathbf{w}|} = & (403 \pm 145)\ Ns^2/m^2 \end{array} \right.
\end{array}
\tag{4.17}
$$

At last notice that the value of the eta model heave efficiency parameter estimated by the above described dynamic tests is remarkably similar to the value that has been measured by static tests performed in a swimming pool: ROMEO has been fixed to a dynamometer as shown in figures (4.14) (4.15) and the maximum heave force has been measured in both the positive and negative vertical directions. Figures (4.16) and (4.17) show a zoomed view of the dynamometer showing that the maximum vertical force in the downward direction is almost double then in the upwards one even in static conditions. Indeed this result validates the developed dynamic model.

4.2.5 Yaw model identification

As far as the yaw axis identification is concerned two type of experiments are analyzed. They will be called type A and B. The first consists of constant applied torque by all four horizontal thrusters, the second in constant applied torque by only two horizontal thrusters on the vehicles diagonal. With these kind of tests the loss of thruster efficiency, with respect to the thrust tunnel measured value, due to propeller hull and propeller-propeller interactions, can be estimated. The vehicle performed about one complete circle at each torque value. The angular position measured by a Watson inertial sensor and a Kvh compass has been logged (about 500 points per trial, $10Hz$ sampling frequency). The constant yaw rate has been evaluated by least squares (LS) on the part of signal going from $8s$ after the beginning of the constant torque (to avoid the transient) to its end. For the yaw rate $\dot{\psi}$ estimate the following kinematic model has been assumed

$$
\mathbf{y}(t) \;=\; \dot{\psi}\, t + \psi_{\mathbf{0}} + \boldsymbol{\varepsilon} = H\, \boldsymbol{\theta} + \boldsymbol{\varepsilon} \tag{4.18}
$$

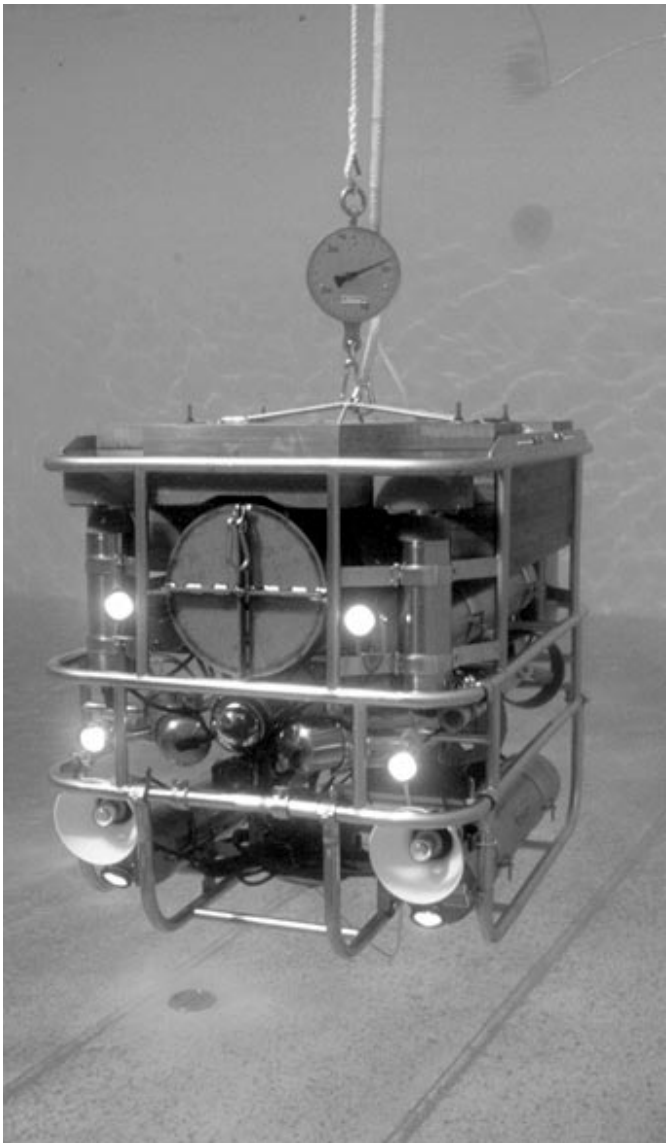

4.14.Maxium static downward thrust

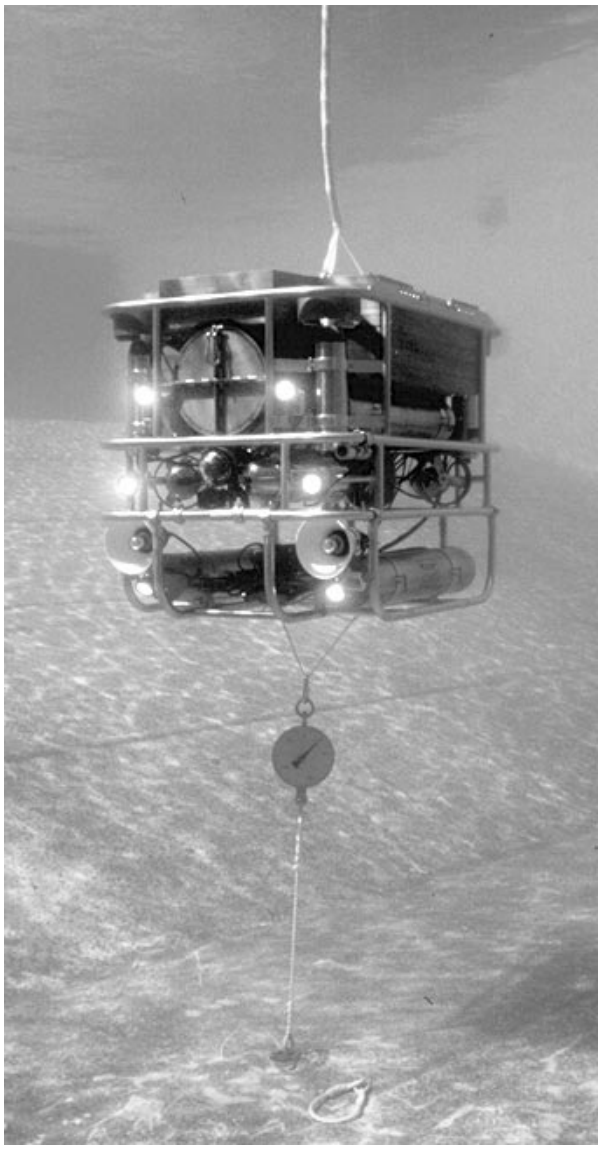

4.15.Maximum upward thrust.

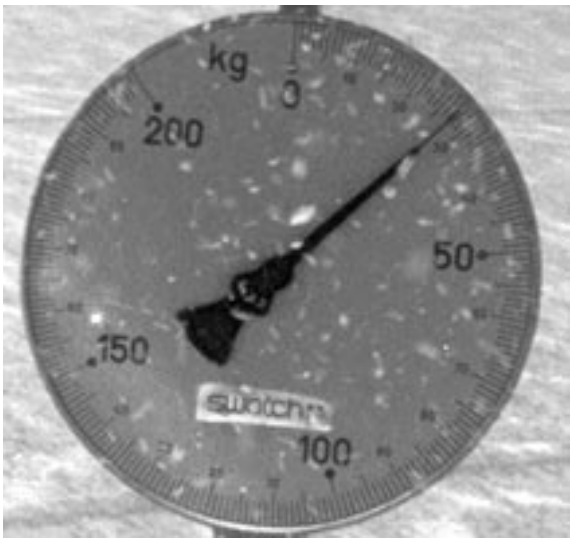

4.16.Zoom of the dynamometer in the static maximum upward thrust

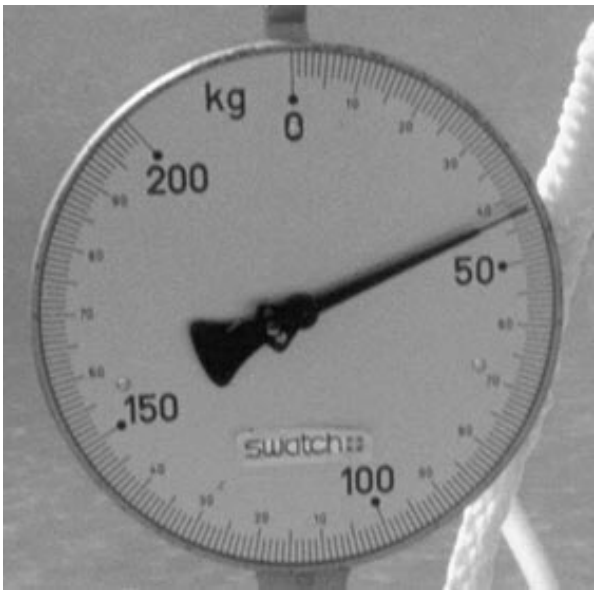

4.17.Zoom of the dynamometer in the static maximum downward thrust

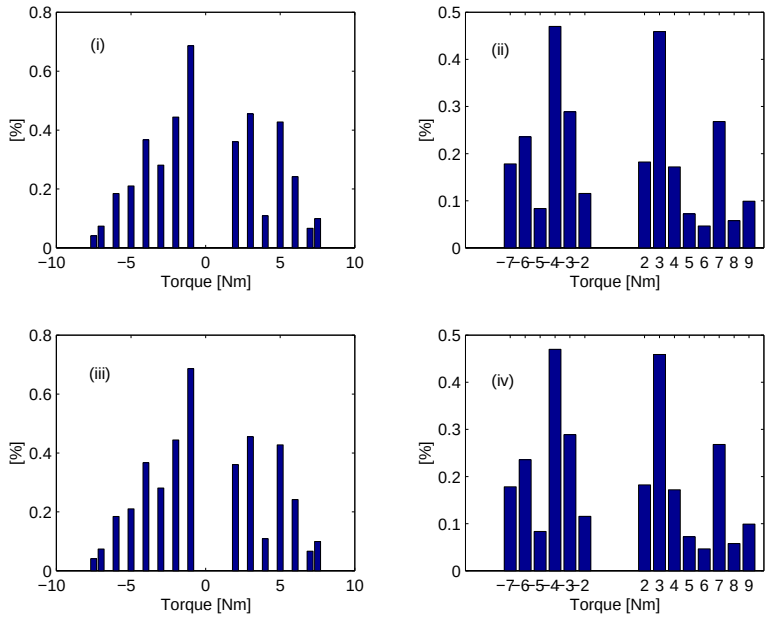

4.18.Percentile yaw rate error for Kvh measurements experiments A (i), B (ii), and for Watson measurements experiments A (iii), B (iv).

$$H \triangleq \begin{bmatrix} t_0 & 1 \\ \vdots & \vdots \\ t_f & 1 \end{bmatrix} ; \boldsymbol{\theta} \triangleq [\dot{\psi}\ \psi_0]^T ; \boldsymbol{\varepsilon} \triangleq noise$$

As the variance of the noise $\boldsymbol{\varepsilon}$ is unknown, the standard LS solution rather then the WLS one, is calculated to estimate the parameter vector

$$\hat{\boldsymbol{\theta}} = (H^T H)^{-1} H^T \mathbf{y}$$

and the $\boldsymbol{\varepsilon}$ noise and $\hat{\boldsymbol{\theta}}$ parameter variances σ^2 and $\sigma^2_{\hat{\theta}}$ are estimated (4.12) (4.6) as

$$\begin{aligned} \hat{\sigma}^2 &= ((\mathbf{y} - H\hat{\boldsymbol{\theta}})^T(\psi - H\hat{\boldsymbol{\theta}}))/(\dim(\mathbf{y}) - \dim(\boldsymbol{\theta})) \\ \hat{\sigma}^2_{\hat{\theta}} &= diag((H^T H)^{-1}\hat{\sigma}^2) \end{aligned}$$

The percentile yaw rate estimated error calculated as $100\frac{\hat{\sigma}_{\hat{\theta}}}{|\hat{\theta}|}$ for experiment A and B for both Kvh and Watson sensors is extremely small for every trial, as shown in figure (4.18) This proofs that the yaw acceleration was indeed negligible during the experimental trials and that the estimated constant yawrate is very precise. Notice that the considered input torques have been chosen to match the typical operating yaw rate range

($\sim [-10 \deg/s, 10 \deg/s]$).

The data of experiment A and B has been fitted with four models derived from the general equation (4.13). They will be denoted as: LQB (linear drag, quadratic drag, bias term), LQNB (linear & quadratic drag and no bias term), LB (linear drag and bias), LNB (linear drag and no bias) for the positive direction, the negative ones and putting positive and negative direction together.

$$\begin{aligned} \tau &= k_r\dot{\psi} + k_{r|r|}\dot{\psi}|\dot{\psi}| + b && \text{LQB Model} \\ \tau &= k_r\dot{\psi} + k_{r|r|}\dot{\psi}|\dot{\psi}| && \text{LQNB Model} \\ \tau &= k_r\dot{\psi} + b && \text{LB Model} \\ \tau &= k_r\dot{\psi} && \text{LNB Model} \end{aligned}$$

The results of the LS fits for both the Kvh and Watson sensors are reported in the following tables:

Exp. A + & - dir	Watson					
Model	LQB +	LB +	LQB -	LB -	LNB -	LNB +
$k_r\ [Nms/rad]$	-1.28	42.613	41.458	33.25	37.498	47.035
$k_{r\|r\|}\ [Nms^2/rad^2]$	241.42	-	-35.32	-	-	-
$b\ [Nm]$	2.05	0.54	-0.3	-0.63	-	-
$100\frac{\sigma_{k_r}}{\|k_r\|}[\%]$	2066	12.3	41.9	12.7	5.7	4.2
$100\frac{\sigma_{k_{r\|r\|}}}{\|k_{r\|r\|}\|}[\%]$	59.43	-	204	-	-	-
$100\frac{\sigma_b}{\|b\|}[\%]$	50.25	109.4	303	87	-	-
$J_{LS}\ [(Nm)^2]$	1.0374	1.7717	3.2592	3.4151	4.1661	2.0681
$\nu\ DOF$	4	5	5	6	7	6

Exp. A + & - dir	Kvh					
Model	LQB +	LB +	LQB -	LB -	LNB -	LNB +
$k_r\ [Nms/rad]$	1	40.41	42.73	32.83	38.966	42.572
$k_{r\|r\|}\ [Nms^2/rad^2]$	191.6	-	-44.38	-	-	-
$b\ [Nm]$	1.89	0.29	-0.53	-0.90	-	-
$100\frac{\sigma_{k_r}}{\|k_r\|}[\%]$	1932	10	33.4	11.26	5.75	3.3
$100\frac{\sigma_{k_{r\|r\|}}}{\|k_{r\|r\|}\|}[\%]$	48.4	-	138.7	-	-	-
$100\frac{\sigma_b}{\|b\|}[\%]$	46	174.3	131.8	51.7	-	-
$J_{LS}\ [(Nm)^2]$	0.58555	1.2105	2.4789	2.7367	4.4423	1.2902
$\nu\ DOF$	4	5	5	6	7	6

Exp. A	Watson			
Model	LQB	LQNB	LB	LNB
$k_r\ [Nms/rad]$	51.723	54.09	41.623	41.22
$k_{r\|r\|}\ [Nms^2/rad^2]$	-66.25	-83.81	-	-
$b\ [Nm]$	0.38	-	0.47	-
$100\frac{\sigma_{k_r}}{\|k_r\|}[\%]$	10.85	11.27	3.96	4.56
$100\frac{\sigma_{k_{r\|r\|}}}{\|k_{r\|r\|}\|}[\%]$	53.5	45.55	-	-
$100\frac{\sigma_b}{\|b\|}[\%]$	50	-	42.8	-
$J_{LS}\ [(Nm)^2]$	6.0436	8.0827	7.8032	11.08
$\nu\ DOF$	12	13	13	14

Exp. A	Kvh			
Model	LQB	LQNB	LB	LNB
$k_r\ [Nms/rad]$	50.59	50.77	40.64	40.62
$k_{r\|r\|}\ [Nms^2/rad^2]$	-63.86	-65.12	-	-
$b\ [Nm]$	0.048	-	0.092	-
$100\frac{\sigma_{k_r}}{\|k_r\|}[\%]$	10.26	9.79	3.56	3.47
$100\frac{\sigma_{k_{r\|r\|}}}{\|k_{r\|r\|}\|}[\%]$	50.52	47.34	-	-
$100\frac{\sigma_b}{\|b\|}[\%]$	341.8	-	197.11	-
$J_{LS}\ [(Nm)^2]$	4.7945	4.8287	6.3599	6.4859
$\nu\ DOF$	12	13	13	14

Exp. B + & - dir	Watson			
Model	LQB +	LB +	LQB -	LB -
$k_r\ [Nms/rad]$	33.042	45.62	-11.04	35.52
$k_{r\|r\|}\ [Nms^2/rad^2]$	41.64	-	223.04	-
$b\ [Nm]$	-0.73	-1.58	-2.53	-0.57
$100\frac{\sigma_{k_r}}{\|k_r\|}[\%]$	87.26	9.92	334	18.92
$100\frac{\sigma_{k_{r\|r\|}}}{\|k_{r\|r\|}\|}[\%]$	226	-	78	-
$100\frac{\sigma_b}{\|b\|}[\%]$	286	46.65	-67	142
$J_{LS}\ [(Nm)^2]$	2.2525	2.3408	1.4136	2.1917
$\nu\ DOF$	5	6	3	4

Exp. B + & - dir	Kvh			
Model	LQB +	LB +	LQB -	LB -
$k_r\ [Nms/rad]$	21.36	42	0.44	34.17
$k_{r\|r\|}\ [Nms^2/rad^2]$	64.12	-	167.24	-
$b\ [Nm]$	-0.0092	-1.49	-2.22	-0.9
$100\frac{\sigma_{k_r}}{\|k_r\|}[\%]$	158.89	11.04	6404	16.32
$100\frac{\sigma_{k_{r\|r\|}}}{\|k_{r\|r\|}\|}[\%]$	162.77	-	81.8	-
$100\frac{\sigma_b}{\|b\|}[\%]$	27754	54.3	55.76	71.39
$J_{LS}\ [(Nm)^2]$	2.6594	2.8602	1.1241	1.68
$\nu\ DOF$	5	6	3	4

Exp. B	Watson			
Model	LQB	LQNB	LB	LNB
$k_r\ [Nms/rad]$	29.34	32.51	38.08	37.39
$k_{r\|r\|}\ [Nms^2/rad^2]$	52.58	28.66	-	-
$b\ [Nm]$	-0.47	-	-0.35	-
$100\frac{\sigma_{k_r}}{\|k_r\|}[\%]$	16.86	17.62	3.48	3.69
$100\frac{\sigma_{k_{r\|r\|}}}{\|k_{r\|r\|}\|}[\%]$	54.95	114	-	-
$100\frac{\sigma_b}{\|b\|}[\%]$	40.1	-	54.53	-
$J_{LS}\ [(Nm)^2]$	4.4195	6.9175	5.75	7.3617
$\nu\ DOF$	11	12	12	13

Exp. B	Kvh			
Model	LQB	LQNB	LB	LNB
$k_r\ [Nms/rad]$	30.57	35.93	37.08	35.7
$k_{r\|r\|}\ [Nms^2/rad^2]$	37.08	-1.26	-	-
$b\ [Nm]$	-0.75	-	-0.64	-
$100\frac{\sigma_{k_r}}{\|k_r\|}[\%]$	15.23	18.16	3.31	4.38
$100\frac{\sigma_{k_{r\|r\|}}}{\|k_{r\|r\|}\|}[\%]$	69.25	2751	-	-
$100\frac{\sigma_b}{\|b\|}[\%]$	25.94	-	29.21	-
$J_{LS}\ [(Nm)^2]$	4.384	10.308	5.2151	10.309
$\nu\ DOF$	11	12	12	13

The parameter variances have been calculated by equation (4.6) having the torque variance been estimated by equation (4.12). The above reported tables are quite significant to understand the most correct way of modelling a pure yaw motion at standard operating velocities: the high value of the percentile relative error of the quadratic drag term indicates that at the considered velocities ($\dot{\psi} \leq 10\ \mathrm{deg}/s$) drag is a linear function of speed. This is also confirmed by the value of the quadratic drag term itself, that is

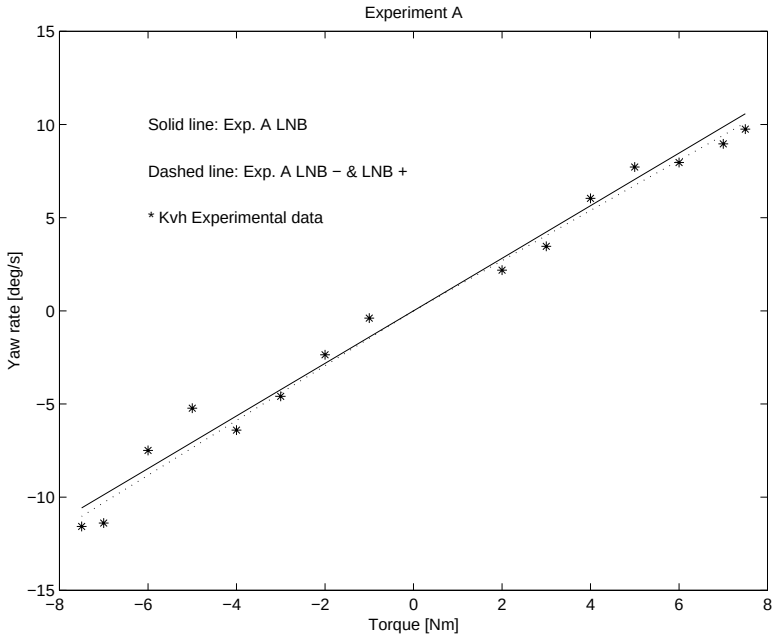

4.19.Yaw rate as a function of applied torque: experiment A, Kvh data

sometimes estimated to be negative, and more intuitively by the plots in figures (4.19) to (4.22). The bias term, introduced to model eventual unmodeled terms, is actually unnecessary as confirmed by the value of its estimated relative percentile error, and the most reliable model is the simple linear no-bias LNB one. The quadratic drag term is expect to become relevant only at higher yaw rates. The plots in figures (4.19), (4.20), (4.21) and (4.22) show also that modeling the right hand side and left hand side turns with different drag coefficients gives only a small fitting improvement that, for the sake of simplicity, can be neglected without serious loss of information.

At last the efficiency loss due to propeller hull and propeller propeller interactions has been considered: propeller hull interactions can be reasonably thought to be responsible of thruster efficiency loss in the B experiment. With reference to figure (4.3) the applied torque and yaw rate relative to the operation of the only front left (FL) and rear right (RR) thrusters are denoted by τ_+ and $\dot{\psi}_+$: notice that when only the FL and RR thrusters apply a right turn torque there is no propeller propeller interaction with the rear left (RL) or front right (FR) thrusters and the outgoing water flow does not interact with the vehicles hull. As a consequence the efficiency of the two operating thrusters is assumed to be equal to the one measured in the thrust tunnel. On the contrary, when the same FL and RR thrusters apply a left hand side yaw rate, i.e. $\dot{\psi}_-$, their efficiency is reasonably thought to be reduced by a propeller-hull interaction due to the thruster disposition. As

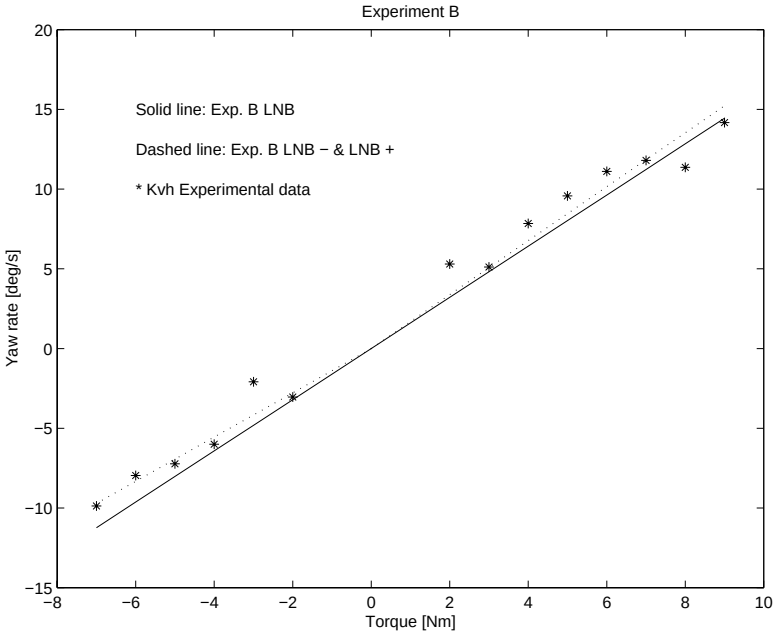

4.20.Yaw rate as a function of applied torque: experiment B, Kvh data

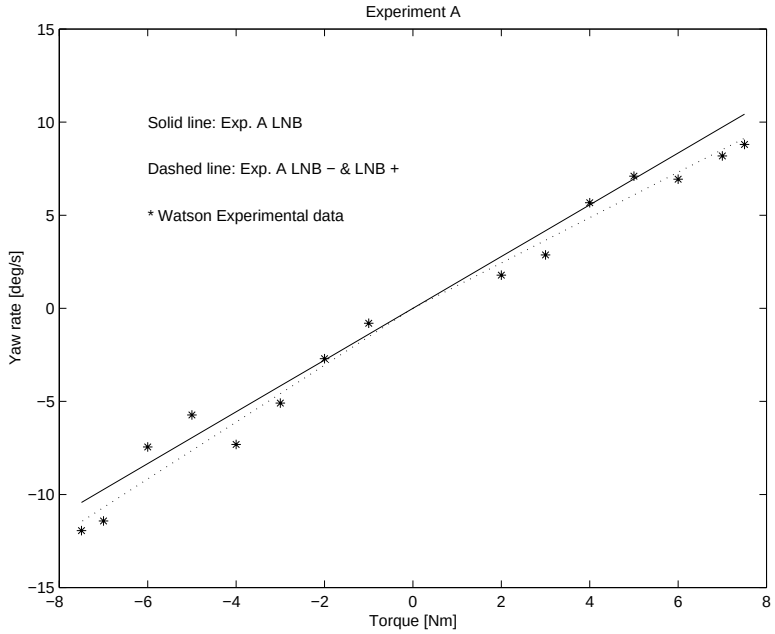

4.21. Yaw rate as a function of applied torque: experiment A, Watson data

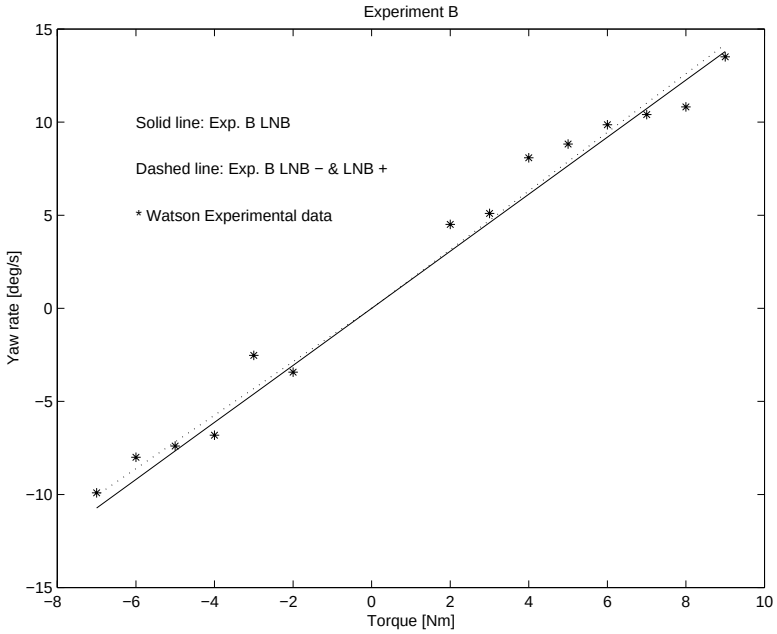

4.22.Yaw rate as a function of applied torque: experiment B, Watson data

a consequence the following *eta-models* are tested and identified:

$$\eta\text{LNB} \quad : \quad \begin{bmatrix} \tau_+ \\ \vdots \\ 0 \end{bmatrix} = \begin{bmatrix} \dot{\psi}_+ & 0 \\ \vdots & \vdots \\ \dot{\psi}_- & -\tau_- \end{bmatrix} \begin{bmatrix} k_r \\ \eta \end{bmatrix} \tag{4.19}$$

$$\eta\text{LB} \quad : \quad \begin{bmatrix} \tau_+ \\ \vdots \\ 0 \end{bmatrix} = \begin{bmatrix} \dot{\psi}_+ & 1 & 0 \\ \vdots & \vdots & \vdots \\ \dot{\psi}_- & 1 & -\tau_- \end{bmatrix} \begin{bmatrix} k_r \\ b \\ \eta \end{bmatrix} \tag{4.20}$$

$$\eta\text{LQNB} \quad : \quad \begin{bmatrix} \tau_+ \\ \vdots \\ 0 \end{bmatrix} = \begin{bmatrix} \dot{\psi}_+ & \dot{\psi}_+|\dot{\psi}_+| & 0 \\ \vdots & \vdots & \vdots \\ \dot{\psi}_- & \dot{\psi}_-|\dot{\psi}_-| & -\tau_- \end{bmatrix} \begin{bmatrix} k_r \\ k_{r|r|} \\ \eta \end{bmatrix} \tag{4.21}$$

$$\eta\text{LQB} \quad : \quad \begin{bmatrix} \tau_+ \\ \vdots \\ 0 \end{bmatrix} = \begin{bmatrix} \dot{\psi}_+ & \dot{\psi}_+|\dot{\psi}_+| & 1 & 0 \\ \vdots & \vdots & \vdots & \vdots \\ \dot{\psi}_- & \dot{\psi}_-|\dot{\psi}_-| & 1 & -\tau_- \end{bmatrix} \begin{bmatrix} k_r \\ k_{r|r|} \\ b \\ \eta \end{bmatrix} \tag{4.22}$$

Exp. B eta-model	Watson			
Model	ηLNB	ηLB	ηLQNB	ηLQB
$k_r\ [Nms/rad]$	36.11	39.23	24.79	27.13
$k_{r\|r\|}\ [Nms^2/rad^2]$	-	-	62.14	57.79
$b\ [Nm]$	-	-0.54	-	-0.27
η	0.89	1.07	0.82	0.92
$100\frac{\sigma_{k_r}}{\|k_r\|}[\%]$	4.29	9.51	23.12	28.38
$100\frac{\sigma_{k_{r\|r\|}}}{\|k_{r\|r\|}\|}[\%]$	-	-	49.16	57
$100\frac{\sigma_b}{\|b\|}[\%]$	-	108.8	-	209
$100\frac{\sigma_\eta}{\|\eta\|}[\%]$	8.06	19.58	8.63	22.9
$J_{LS}\ [(Nm)^2]$	6.13	5.693	4.4542	4.3545
$\nu\ DOF$	12	11	11	10

Exp. B eta-mod	Kvh			
Model	ηLNB	ηLB	ηLQNB	ηLQB
$k_r\ [Nms/rad]$	33.66	38.19	23.08	27.84
$k_{r\|r\|}\ [Nms^2/rad^2]$	-	-	54.07	43.98
$b\ [Nm]$	-	-0.83	-	-0.51
η	0.8	1.07	0.73	0.91
$100\frac{\sigma_{k_r}}{\|k_r\|}[\%]$	4.29	9.01	24.89	28.95
$100\frac{\sigma_{k_{r\|r\|}}}{\|k_{r\|r\|}\|}[\%]$	-	-	52.85	71.08
$100\frac{\sigma_b}{\|b\|}[\%]$	-	69.7	-	117.13
$100\frac{\sigma_\eta}{\|\eta\|}[\%]$	8.70	18.57	10.22	24.59
$J_{LS}\ [(Nm)^2]$	6.1242	5.159	4.6204	4.3066
$\nu\ DOF$	12	11	11	10

The $\hat{\eta} < 1$ value of the η estimate and its very low value of the relative percentile error shows both, that the expected efficiency loss actually takes place, and that it can be correctly modeled by the η parameter. Moreover the simple ηLNB model is confirmed again to be the best one as both the bias and quadratic drag relative errors given by the other models are very large. When experiment A is considered also propeller-propeller interactions among the thrusters on the same vehicle side, i.e. FL-RL and FR-RR, should be also taken into account. As it is not feasible to distinguish, in this case, between the loss of efficiency due to propeller-hull and propeller-propeller interactions, they are modeled by a unique parameter as follows. From the above experimental results and the consequent discussion, the most reliable model is the simple LNB one. Moreover, with reference to the above tables, comparing the residual least squares cost J_{LS} (4.4) of the experiment B LNB model ($J_{LS} = 10.3(Nm)^2$ for the Kvh data and $J_{LS} = 7.36(Nm)^2$ for the Watson data) with the experiment B ηLNB one ($J_{LS} = 6.12(Nm)^2$ for the Kvh data and $J_{LS} = 6.13(Nm)^2$ for the Watson data), the ηLNB model guarantees the best performance. Intuitively the ηLNB model estimate of k_r is the most reliable as the torque values adopted in the ηLNB model are the closest to the thrust tunnel identified ones. Consequently an efficiency parameter modeling both the propeller propeller and propeller hull interactions occurring in experiment A can be introduced as:

$$\eta_A \tau_A = \hat{k}_r \dot{\psi} \tag{4.23}$$

being $\hat{k}_r$ the linear drag ηLNB model estimate, η_A the experiment A efficiency parameter to be identified and τ_A the thrust tunnel model experiment A torque. From the above tables it follows that the $\hat{k}_r$ linear drag ηLNB model estimate is

$$\begin{aligned} \hat{k}_r &= 36.11\ Nms/rad : Watson \\ \hat{k}_r &= 33.66\ Nms/rad : Kvh \end{aligned}$$

As a consequence, the LS estimate of η_A relative to equation (4.23) is:

$$Watson \;:\; \eta_A = 0.85 \pm 0.04 \Rightarrow 100\frac{\sigma_{\eta_A}}{\eta_A} = 4.7\%\ J_{LS} = 8.26Nm$$
$$Kvh \;:\; \eta_A = 0.81 \pm 0.03 \Rightarrow 100\frac{\sigma_{\eta_A}}{\eta_A} = 3.7\%\ J_{LS} = 4.38Nm$$

where the parameter errors have been calculated according to equations (4.12) and (4.6).

In conclusion the yaw motion of the ROMEO ROV vehicle in the velocity range $[-10\,\mathrm{deg}/s, 10\,\mathrm{deg}/s]$ is best modeled by an ηLNB model having a linear drag parameter $k_r = 34 \pm 2\ Nms/rad$ (KVH value). Moreover the above results have shown that modeling the left hand side and right hand side turns with different models is unnecessary and that the propeller hull and propeller propeller interactions may reduce the ideal thruster efficiency of about 15% or 20%.

4.2.6 Surge model identification

The considered surge model is the same simplified uncoupled one (4.13) adopted for the other degrees of freedom, i.e.

$$m_u\dot{u} = -k_u u - k_{u|u|}u|u| + \tau_u + \varepsilon \tag{4.24}$$

The experimental data used to identify this model consists in the applied voltage on the four horizontal thrusters and the vehicles position with respect to the swimming pool wall as measured by a $3.3Hz$ sampling rate sonar profiler. In order to identify the drag coefficients a constant force has been applied to the vehicle and the corresponding regime value of the surge velocity has been estimated fitting by least squares the position measurements. Moreover, to evaluate the loss of efficiency in the surge direction due to propeller propeller and propeller hull interactions, the input force has been applied with three different thrust mappings denoted in the following by A, B and C: with reference to figures (4.1), (4.2), (4.3) the three type of experiments consist in

A Only the front thrusters are used: their efficiency, with respect to the thrust tunnel identified model, is assumed to be 100% when pushing forward and eventually less when pushing backwards due to interference between the thruster outgoing water flow and the vehicles hull.

B All the 4 thrusters are used: their efficiency, with respect to the thrust tunnel identified model, is assumed to be eventually reduced by the interference of the front and rear thruster water flows between each other and with the vehicles hull.

C Only the rear thrusters are used: their efficiency, with respect to the thrust tunnel identified model, is assumed to be 100% when pushing backwards (negative x direction) and eventually less when pushing forward due to interference between the thruster outgoing water flow and the vehicles hull.

The underlying idea is that when the front thrusters push backwards or the rear one

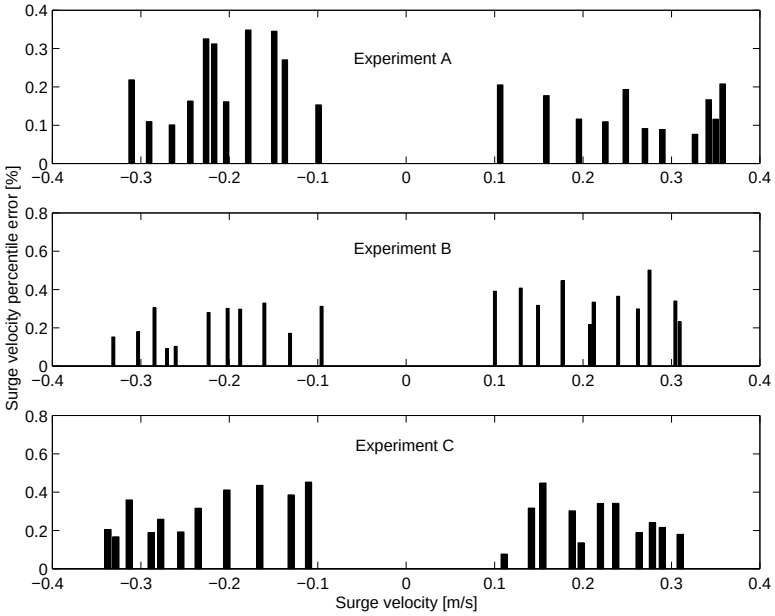

4.23.Surge velocity percentile relative error for experiments A, B and C

push forward, their efficiency may be affected by a propeller hull interaction due to the fact that in such circumstances the outgoing water flow is directed towards the vehicle. Moreover when all 4 thruster operate in the surge direction the outgoing and ingoing flows of the front and rear thrusters may be affected by the presence of each other thus giving rise to a propeller propeller interaction. The estimated velocity for each of the three kind of experiments is very precise as shown in figure (4.23). The relative percentile errors displayed in figure (4.23) have been calculated as $100\hat{\sigma}_{\hat{u}}/\hat{u}$ being $\hat{u}$ the least squares estimate of the surge velocity and $\hat{\sigma}_{\hat{u}}$ its estimated standard deviation as given by the application of equations (4.5), (4.6), (4.12) to the kinematic model

$$\begin{aligned} x &= ut + \varepsilon \\ x &: \text{ sonar measurements} \end{aligned}$$

The *nominal* applied surge forces[4] range from $10N$ to $60N$. Indicating with u_{A+}, u_{B+}, u_{C+}, u_{A-}, u_{B-}, u_{C-}, τ_{A+}, τ_{B+}, τ_{C+}, τ_{A-}, τ_{B-} and τ_{C-} the row vectors containing the norms of each regime surge velocity and corresponding nominal applied thrusts of experiments A, B and C in the positive $(+)$ and negative $(-)$ directions, the consid-

[4] As estimated by the thrust tunnel model

ered surge models are

$$\begin{bmatrix} \tau_{A+} \\ 0 \end{bmatrix} = \begin{bmatrix} u_{A+} & u_{A+}|u_{A+}| & 0 \\ u_{C+} & u_{C+}|u_{C+}| & -\tau_{C+} \end{bmatrix} \begin{bmatrix} k_u^+ \\ k_{u|u|}^+ \\ \eta_u^+ \end{bmatrix} \tag{4.25}$$

$$\begin{bmatrix} \tau_{C-} \\ 0 \end{bmatrix} = \begin{bmatrix} u_{C-} & u_{C-}|u_{C-}| & 0 \\ u_{A-} & u_{A-}|u_{A-}| & -\tau_{A-} \end{bmatrix} \begin{bmatrix} k_u^- \\ k_{u|u|}^- \\ \eta_u^- \end{bmatrix} \tag{4.26}$$

$$\begin{bmatrix} \tau_{A+} \\ \tau_{C-} \\ 0 \\ 0 \end{bmatrix} = \begin{bmatrix} u_{A+} & u_{A+}|u_{A+}| & 0 \\ u_{C-} & u_{C-}|u_{C-}| & 0 \\ u_{A-} & u_{A-}|u_{A-}| & -\tau_{A-} \\ u_{C+} & u_{C+}|u_{C+}| & -\tau_{C+} \end{bmatrix} \begin{bmatrix} k_u \\ k_{u|u|} \\ \eta_u \end{bmatrix} \tag{4.27}$$

being (4.25) relative to the forward direction drag coefficients and the rear thrusters propeller hull interaction efficiency coefficient, (4.26) relative to the backward direction drag coefficients and the front thrusters propeller hull interaction efficiency coefficient and (4.27) relative to a model that does not distinguish the positive and negative directions. Each u and τ vector in the above equations (4.25), (4.26), (4.27) has dimension 11×1. Applying the least squares technique to the three models (4.25), (4.26) and (4.27) yields

$$\begin{array}{lll} k_u^+ = (38 \pm 7) Ns/m & k_{u|u|}^+ = (333 \pm 24) Ns^2/m^2 & \eta_u^+ = (0.72 \pm 0.02) \\ k_u^- = (53 \pm 7) Ns/m & k_{u|u|}^- = (347 \pm 24) Ns^2/m^2 & \eta_u^- = (0.80 \pm 0.02) \\ k_u = (50 \pm 8) Ns/m & k_{u|u|} = (322 \pm 26) Ns^2/m^2 & \eta_u = (0.76 \pm 0.02) \end{array}$$

where the parameter errors are the standard deviations as calculated by equations (4.6) and (4.12). To evaluate the performance of the considered models the residual cost $J_{LS}(\hat{\boldsymbol{\theta}})$ (4.4) and the relative degrees ν of freedom are reported:

$$\begin{array}{lll} J_{LS}^+ = 54.33N^2 & \nu^+ = 22 - 3 = 19 & \frac{J_{LS}^+}{\nu^+} = 2.86N^2 \\ J_{LS}^- = 45.16N^2 & \nu^- = 22 - 3 = 19 & \frac{J_{LS}^-}{\nu^-} = 2.37N^2 \\ J_{LS} = 241.17N^2 & \nu = 44 - 3 = 41 & \frac{J_{LS}}{\nu} = 5.88N^2 \end{array}$$

showing that in the considered thrust and velocity ranges the best performance is achieved distinguishing two different models for the forward and backward motion which is not surprising in consideration of the open frame structure of the vehicle shown in figure (4.1) and (4.2). For a qualitative evaluation of the reliability of the proposed model refer to figure (4.24) where the experimental data of the C experiment is fitted by

$$\begin{aligned} \tau_{C-} &= k_u^- u_{C-} + k_{u|u|}^- u_{C-}|u_{C-}| : \mathbf{u}^T \mathbf{e}_x < 0 \\ \eta_u^+ \tau_{C+} &= k_u^+ u_{C+} + k_{u|u|}^+ u_{C+}|u_{C+}| : \mathbf{u}^T \mathbf{e}_x \geq 0 \end{aligned}$$

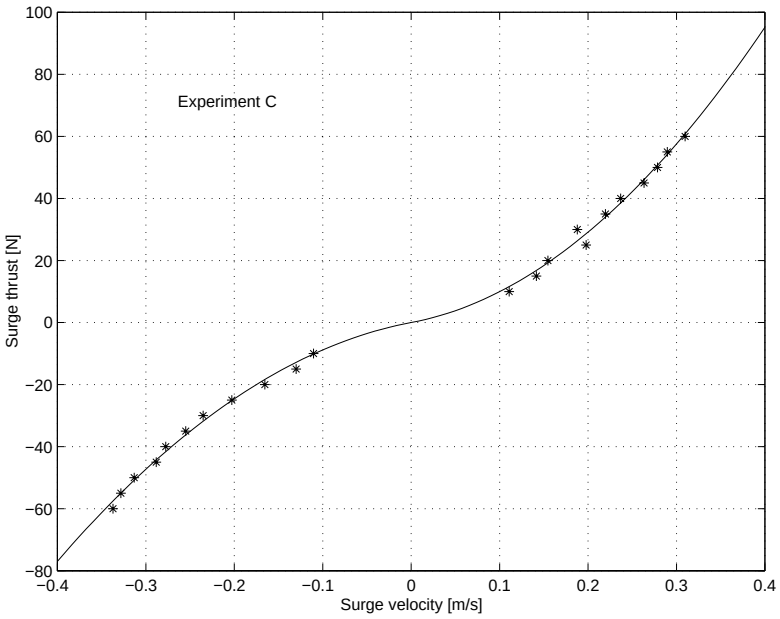

4.24.Experiment C fitted data.

Finally the loss of efficiency related to the propeller propeller and propeller hull interactions occurring when all four thrusters are adopted for a forward motion has been estimated with the data of experiment B: assuming the drag coefficients in the forward direction to be $k_u^+ = (38 \pm 7)Ns/m$ and $k_{u|u|}^+ = (333 \pm 24)Ns^2/m^2$ the least squares fitting of the model

$$k_u^+ u_{B+} + k_{u|u|}^+ u_{B+}|u_{B+}| = \tau_B \eta_{all}$$

yields

$$\eta_{all} = (0.75 \pm 0.01)$$

showing the relevance of the considered phenomenon. The above reported analysis refers to the vehicles configuration shown in the first 5 (from top to bottom and from left to right) pictures in figure (4.1). To evaluate the sensitivity of the drag and efficiency parameters on the vehicles payload configuration, experiments A, B and C described above have been repeated with a plankton sampling equipment mounted on ROMEO as shown in the bottom right picture in figure (4.1). Fitting these data with the models given by equations (4.25) and (4.26) yields

$$\begin{array}{lll} k_u^+ = (40 \pm 12)Ns/m & k_{u|u|}^+ = (305 \pm 38)Ns^2/m^2 & \eta_u^+ = (0.68 \pm 0.03) \\ k_u^- = (25 \pm 7)Ns/m & k_{u|u|}^- = (405 \pm 24)Ns^2/m^2 & \eta_u^- = (0.61 \pm 0.02) \end{array}$$

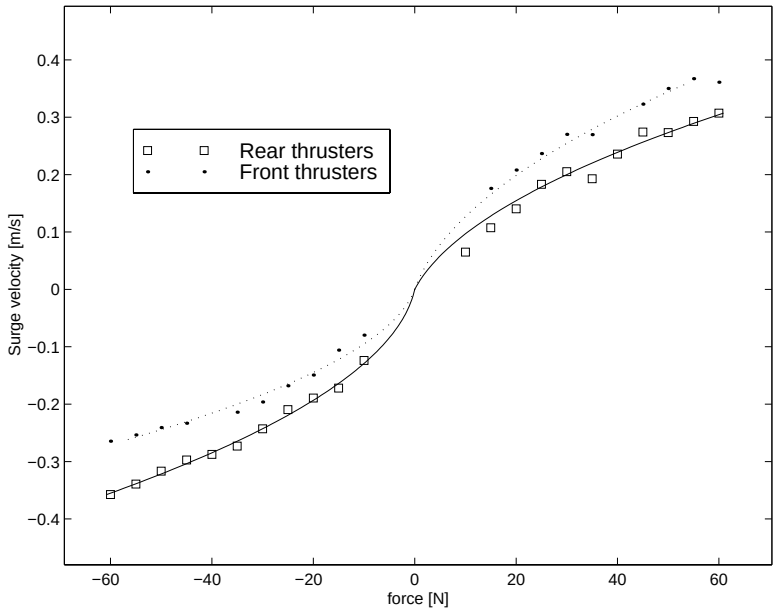

4.25.Estimated surge velocity versus the nominal, i.e. thrust tunnel model, applied force with the plankton sampling payload configuration.

and

$$J_{LS}^{+} = 109.6N^2 \quad \nu^{+} = 20 - 3 = 17 \quad \frac{J_{LS}^{+}}{\nu^{+}} = 6.4N^2$$
$$J_{LS}^{-} = 39.6N^2 \quad \nu^{-} = 21 - 3 = 18 \quad \frac{J_{LS}^{-}}{\nu^{-}} = 2.2N^2$$

showing that the considered payload indeed has an important, although not dramatic, influence of the dynamics of the vehicle. The importance of the efficiency parameter role may be better understood plotting the estimated regime velocities versus the nominal applied thruster forces relative to the experiments A (only front thrusters) and C (only rear thrusters) as shown in figure (4.25). The solid line in figure (4.25) refers to the model

$$\begin{aligned} \tau_{C-} &= k_u^{-} u_{C-} + k_{u|u|}^{-} u_{C-} |u_{C-}| : \mathbf{u}^T \mathbf{e}_x < 0 \\ \eta_u^{+} \tau_{C+} &= k_u^{+} u_{C+} + k_{u|u|}^{+} u_{C+} |u_{C+}| : \mathbf{u}^T \mathbf{e}_x \geq 0 \end{aligned}$$

and the dashed one to the model

$$\begin{aligned} \eta_u^{-} \tau_{A-} &= k_u^{-} u_{A-} + k_{u|u|}^{-} u_{A-} |u_{A-}| : \mathbf{u}^T \mathbf{e}_x < 0 \\ \tau_{A+} &= k_u^{+} u_{A+} + k_{u|u|}^{+} u_{A+} |u_{C+}| : \mathbf{u}^T \mathbf{e}_x \geq 0 \end{aligned}$$

4.2.7 Sway model identification

The considered sway axis model is

$$m\dot{v} = k_v v + k_{v|v|} v|v| + \tau_v + \varepsilon$$

in accordance with equation (4.13). As for the surge motion, the sway drag coefficients have been estimated by constant applied thrust in 3 different thrust mapping configurations:

A With reference to figure (4.3), only the left thrusters are used: their efficiency, with respect to the thrust tunnel identified model, is assumed to be 100% when pushing right (positive y direction) and eventually less when pushing left (negative y direction) due to interference between the thruster outgoing water flow and the vehicles hull.

B With reference to figure (4.3), only the right thrusters are used: their efficiency, with respect to the thrust tunnel identified model, is assumed to be 100% when pushing left (negative y direction) and eventually less when pushing right (positive y direction) due to interference between the thruster outgoing water flow and the vehicles hull.

C All the 4 thrusters are used: their efficiency, with respect to the thrust tunnel identified model, is assumed to be eventually reduced, in both y directions, by the interference of the left and right thruster water flows between each other and with the vehicles hull.

The measured data consists in the thruster applied voltage and the vehicles position as measured by a $3.3Hz$ sampling rate sonar profiler with respect to the swimming pool wall. The sway velocity is estimated applying least squares to the position measurements giving rise to very precise estimates (less then a 3% error) as shown by the plots in figure (4.26).

The velocity standard deviation has been calculated according to equations (4.6) and (4.12). Given these data and in accordance with the surge case, the following 3 models have been considered:

$$\begin{bmatrix} \tau_{A+} \\ 0 \end{bmatrix} = \begin{bmatrix} v_{A+} & v_{A+}|v_{A+}| & 0 \\ v_{B+} & v_{B+}|v_{B+}| & -\tau_{B+} \end{bmatrix} \begin{bmatrix} k_v^+ \\ k_{v|v|}^+ \\ \eta_v^+ \end{bmatrix} \tag{4.28}$$

$$\begin{bmatrix} \tau_{B-} \\ 0 \end{bmatrix} = \begin{bmatrix} v_{B-} & v_{B-}|v_{B-}| & 0 \\ v_{A-} & v_{A-}|v_{A-}| & -\tau_{A-} \end{bmatrix} \begin{bmatrix} k_v^- \\ k_{v|v|}^- \\ \eta_v^- \end{bmatrix} \tag{4.29}$$

$$\begin{bmatrix} \tau_{A+} \\ \tau_{B-} \\ 0 \\ 0 \end{bmatrix} = \begin{bmatrix} v_{A+} & v_{A+}|v_{A+}| & 0 \\ v_{B-} & v_{B-}|v_{B-}| & 0 \\ v_{A-} & v_{A-}|v_{A-}| & -\tau_{A-} \\ v_{B+} & v_{B+}|v_{B+}| & -\tau_{B+} \end{bmatrix} \begin{bmatrix} k_v \\ k_{v|v|} \\ \eta_v \end{bmatrix} \tag{4.30}$$

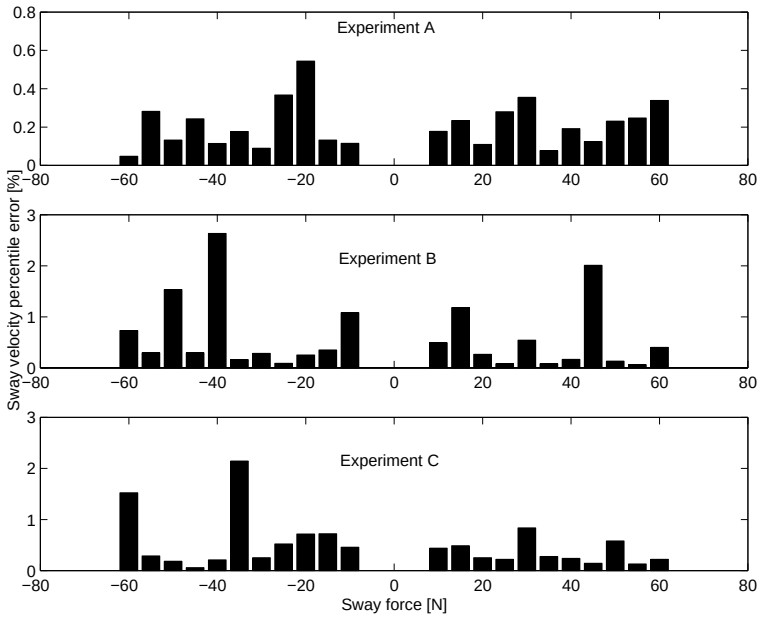

4.26.Relative percentile sway velocity error.

being τ_{A+}, τ_{A-}, v_{A+}, v_{A-}, v_{B+}, v_{B-}, τ_{B+} and τ_{B-} vectors whose components are the norms of the thrust tunnel model calculated thrust and the norms of the least squares estimated sway velocities. As the experimental data has been acquired for nominal applied thrusts of norms ranging from $10N$ to $60N$ with $5N$ increments, each of the above τ and v vector has dimension 11×1. Equations (4.28) and (4.29) assume different drag coefficients in the positive and negative y direction, while equation (4.30) assumes full symmetry with respect to the x axis. The resulting parameter vector estimates according to the three models are:

$$\begin{array}{lll} k_v^+ = (148 \pm 27)Ns/m & k_{v|v|}^+ = (302 \pm 127)Ns^2/m^2 & \eta_v^+ = (0.87 \pm 0.05) \\ k_v^- = (104 \pm 22)Ns/m & k_{v|v|}^- = (735 \pm 121)Ns^2/m^2 & \eta_v^- = (0.95 \pm 0.04) \\ k_v = (150 \pm 20)Ns/m & k_{v|v|} = (363 \pm 101)Ns^2/m^2 & \eta_v = (0.90 \pm 0.04) \end{array}$$

and the residual least squares cost $J_{LS}(\hat{\boldsymbol{\theta}})$ (4.4) is:

$$\begin{array}{lll} J_{LS}^+ = 370.89N^2 & \nu^+ = 22 - 3 = 19 & \frac{J_{LS}^+}{\nu^+} = 19.5N^2 \\ J_{LS}^- = 194.87N^2 & \nu^- = 22 - 3 = 19 & \frac{J_{LS}^-}{\nu^-} = 10.26N^2 \\ J_{LS} = 877.6N^2 & \nu = 44 - 3 = 41 & \frac{J_{LS}}{\nu} = 21.4N^2 \end{array}$$

The performance of these models can be graphically evaluated by the plots of the experiment A and B data fitted as follows:

$$\begin{aligned} \tau_A &= k_v^+ v + k_{v|v|}^+ v|v| : \boldsymbol{\tau}_A^T \mathbf{e}_y > 0 \\ \eta_v^- \tau_A &= k_v^- v + k_{v|v|}^- v|v| : \boldsymbol{\tau}_A^T \mathbf{e}_y < 0 \end{aligned}$$

in figure (4.27),

$$\begin{aligned} \tau_B &= k_v^- v + k_{v|v|}^- v|v| : \boldsymbol{\tau}_B^T \mathbf{e}_y < 0 \\ \eta_v^+ \tau_B &= k_v^+ v + k_{v|v|}^+ v|v| : \boldsymbol{\tau}_B^T \mathbf{e}_y > 0 \end{aligned}$$

in figure (4.28). As far as the experiment C (all four thrusters) is concerned, its data can be fitted with a model that takes into account the propeller propeller and propeller hull interactions of the horizontal thrusters, and assumes the drag coefficients in the two directions to be k_v^+, $k_{v|v|}^+$, k_v^- and $k_{v|v|}^-$ previously identified by experiment A (only left thrusters) and B (only right thrusters) as described above. In particular the following is considered:

$$\eta_C^+ \tau_{C+} = k_v^+ v + k_{v|v|}^+ v|v| : \boldsymbol{\tau}_C^T \mathbf{e}_y > 0 \quad (4.31)$$

$$\eta_C^- \tau_{C-} = k_v^- v + k_{v|v|}^- v|v| : \boldsymbol{\tau}_C^T \mathbf{e}_y < 0 \quad (4.32)$$

and with the usual least squares technique the efficiency parameters η_C^+ and η_C^- are found

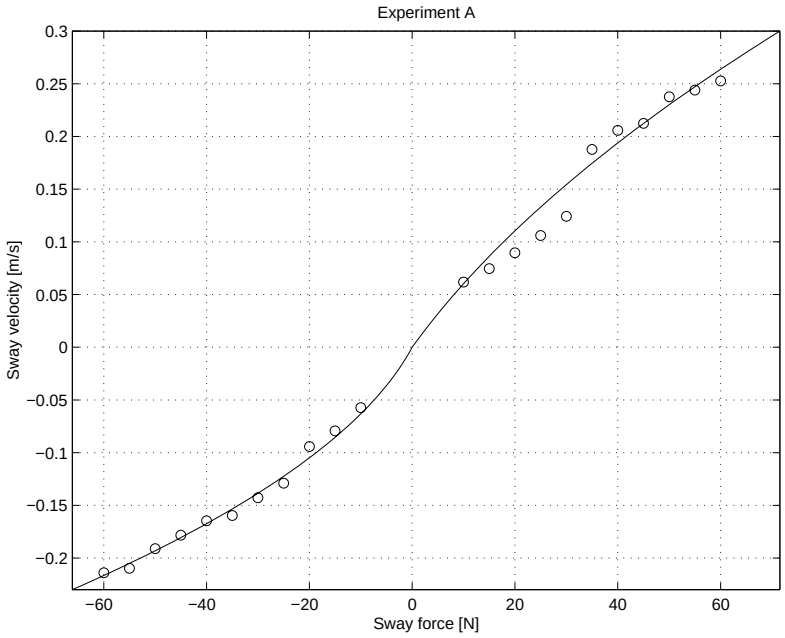

4.27.Experiment A fitted data.

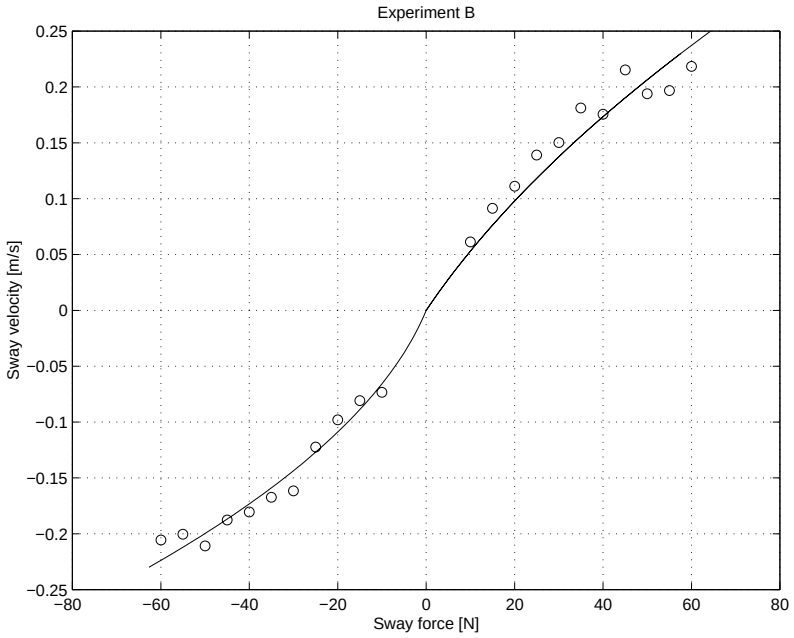

4.28.Experiment B fitted data.

to be:

$$\begin{aligned} \eta_C^+ &= (0.78 \pm 0.02) \\ \eta_C^- &= (0.76 \pm 0.03) \end{aligned}$$

The performance of the model taking into account the propeller propeller and propeller hull interactions of the four thrusters as described by equations (4.31) and (4.32) is graphically shown in figure (4.29) where the model calculated sway velocity is plotted with the experimental data of experiment C.

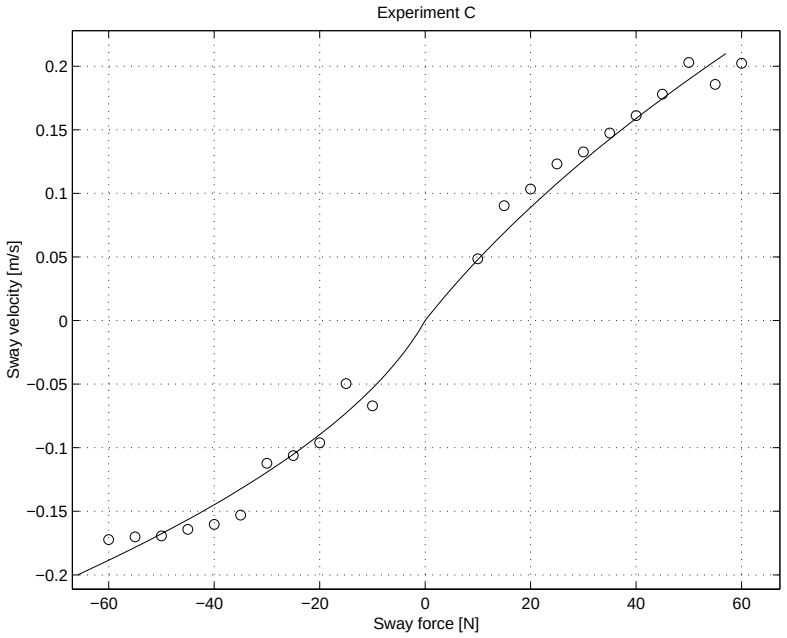

4.29.Experiment C fitted data.

4.2.8 Inertia parameters identification

An identification procedure of the inertial parameter of a decoupled model of an UUV is proposed. The main idea is to consider the drag parameters known and use this knowledge to design a sub-optimal experiment for the identification of the inertial quantities. The model to identify is given by equation (4.13) here reported for reference

$$m\dot{\xi} = -k_\xi \xi - k_{\xi|\xi|}\xi|\xi| + \eta_\xi \tau_\xi + \varepsilon \tag{4.33}$$

where m is the inertial parameter, ξ is the velocity, $\dot{\xi}$ the acceleration, τ_ξ the nomi-

nal cavitation tunnel identified force (or torque), η_ξ the propeller interaction efficiency parameter, k_ξ, $k_{\xi|\xi|}$ the linear and quadratic drag coefficients and ε the noise. τ_ξ is considered known as the propulsion system has been modeled and identified as shown in section (4.2.2). The drag and efficiency coefficients are also assumed known from the identification experiments described above. Within this framework the design of the inertia parameter identification experiment has to take into account some important constraints: due to the absence of accelerometers the identification process must be performed with the only velocity and position measurements and force estimate. Moreover the adopted propulsion model is known to be very accurate when the propellers do not suddenly change revolution direction so a second constraint on the experiment design is to keep constant τ_ξs sign during the whole experiment. Supposing ξ to be

$$\xi = \xi_0 + \Delta_\xi \sin(\omega t) \tag{4.34}$$

with ξ_0, Δ_ξ constants and $\Delta_\xi << \xi_0$ equation (4.33) can be linearized to

$$m\,\dot{\xi} = \tilde{\tau}_\xi - k_l\,\xi \tag{4.35}$$

being $k_l = k_\xi + 2|\xi_0|\ k_{\xi|\xi|}$ and $\tilde{\tau}_\xi = \eta_\xi \tau_\xi + k_{\xi|\xi|}|\xi_0|\xi_0$. Equation (4.35) corresponds to a first order system

$$V(s) = \frac{k_l^{-1}}{\tau s + 1}\,(F(s) + m\xi_0) \tag{4.36}$$

with time constant

$$\tau = m/k_l = \frac{m}{k_\xi + 2|\xi_0|\ k_{\xi|\xi|}}. \tag{4.37}$$

The linear system (4.36) will have an output as equation (4.34) if the input $\tilde{\tau}_\xi$ is the sum of a constant and a sinusoidal wave of frequency ω. Notice that as m is the sum of inertia (known) and added mass (always positive) and k_ξ, $k_{\xi|\xi|}$, ξ_0 are known, a lower bound of the time constant τ is known. Moreover as added mass is expected to be at most 100% of the inertial mass, also an upper bound of τ is given. This estimate can be very useful to choose the exiting frequency ω of the input force. A common criterion [58] [56] for choice of the inputs is to maximize the cost function

$$J = -\log\det M \tag{4.38}$$

being M Fisher's information matrix which depends on the adopted inputs. In robotic applications this criterion (*d-optimal criterion*) has been successfully adopted by Swevers et al. [71] [72] for the identification of an industrial arm. Classical identification theory [56] states that a first order system as (4.36) can be optimally identified (according to criterion (4.38)) with a single sine input of frequency

$$\omega_{opt} = \frac{1}{\sqrt{3}\tau}. \tag{4.39}$$

The input force for the inertia identification experiments is thus chosen to be of the

form:

$$f(t) = f_0 + \Delta_f \sin(\omega_{opt} t) \tag{4.40}$$

The f_0 constant is selected so that its corresponding regime velocity ξ_0 is in the standard operating range, Δ_f is selected to be $\Delta_f \leq f_0$ so that force inversions are avoided and the d-optimal frequency ω_{opt} is selected in accordance to equation (4.39). The system time constant τ needed to compute ω_{opt} is *a priori* estimated by equation (4.37) as the drag coefficients are known and m is supposed to be equal to the inertia in air m_{air} plus a term ranging from 10% to 100% of m_{air} that models added mass. The output $\xi(t)$ of the linear system (4.35) with input $\tilde{\tau}_\xi = f(t)$ given by equation (4.40) is reported for reference:

$$\xi(t) = \xi_0 e^{-t/\tau} + \frac{f_0}{k_l}\left(1 - e^{-t/\tau}\right) + \frac{\Delta_f}{k_l}\frac{\sin(\omega_{opt} t) - \omega_{opt}\tau(\cos(\omega_{opt} t) - 1)}{1 + \omega_{opt}^2 \tau^2}$$

being τ given by equation (4.37).

To cope with the absence of an acceleration measurement, equation (4.13) must be integrated giving

$$m\,\xi(t) - m\,\xi_0 = \varphi(t) - k_\xi\,(\zeta(t) - \zeta_0) - k_{\xi|\xi|}\,I(t) + bt \tag{4.41}$$

$$m\,\xi(t) - m\,\xi_0 - k_\xi \zeta_0 - bt = y$$

$$y \triangleq \varphi(t) - k_\xi\,\zeta(t) - k_{\xi|\xi|}\,I(t) \tag{4.42}$$

being $\varphi(t) = \int_0^t \tau_\xi(\psi) d\psi$, $\zeta(t)$ the position, $I(t) = \int_0^t \xi(\psi)|\xi(\psi)| d\psi$, and b an eventual bias due to the mean of ε and to the numerical integrations performed to calculate φ and I. Notice that the integration process does not affect the d-optimal frequency choice as the integral of equation (4.35) has its same structure, in particular the same time constant. As the drag constants, velocity and position are known equation (4.41) can be written in discrete-time regression form $y = H\boldsymbol{\theta}$ being

$$y = \begin{bmatrix} \varphi_1 - k_\xi \zeta_1 - k_{\xi|\xi|} I_1 \\ \varphi_2 - k_\xi \zeta_2 - k_{\xi|\xi|} I_2 \\ \vdots \\ \varphi_N - k_\xi \zeta_N - k_{\xi|\xi|} I_N \end{bmatrix} \tag{4.43}$$

$$H = \begin{bmatrix} \xi_1 & -1 & -t_1 \\ \xi_2 & -1 & -t_2 \\ \vdots & \vdots & \vdots \\ \xi_N & -1 & -t_N \end{bmatrix} \tag{4.44}$$

$$\boldsymbol{\theta} = [m, (m\,\xi_0 + k_\xi \zeta_0), b]^T \tag{4.45}$$

and N the number of samples. Notice that the linearized system frequency related to equation (4.37) for the translational DOFs is below the Nyquist frequency ($1.65 Hz$)

relative to the slowest on-board sensors ($3.3Hz$ for sonars). For surge $k_u \simeq 38Ns/m$, $k_{u|u|} \simeq 333Ns^2/m^2$ assuming $m \simeq 675Kg$ and $u_0 = 0.2\ m/s$, $\nu = 1/\tau = k_l/m = \frac{k_u + 2u_0\ k_{u|u|}}{m} = 0.25Hz$.

Within this approach the uncertainty on the inertia parameter estimate is expected to be at least of the same order of magnitude of the drag parameter uncertainty. As estimating the inertia m is somehow equivalent to estimating the systems time constant $\tau = m/k_l$, by standard error analysis it follows that $\delta\tau/\tau = \delta k_l/k_l \approx 10\%$. Moreover the applied force τ_ξ, assumed to be known perfectly, will be actually affected by some error that must be reasonable thought to be of about 10%. Numerical errors will be also introduced in the computation of y as due to the absence of a velocity measurement the I quantity is calculated filtering the acquired position signal with an off line Savitzky-Golay polynomial filter to evaluate the velocity ξ and then integrating numerically $\xi|\xi|$ over time. Numerical integrations must be also performed on the position signal and on the applied fore in order to compute y. These considerations and the fact that the sampling rate of the position measurements is very low ($3.3Hz$ for sonars used for the linear DOFs and $10Hz$ for the yaw) suggests that the inertia parameter identification by only on board position measurements can not be expected to be very precise. Nevertheless the estimated value is generally good enough to provide reliable and useful models for modeling and control purposes.

4.2.9 Surge inertia parameter identification

The above described technique has been experimentally implemented on the surge and yaw axis of the ROMEO ROV. The surge experiments have been performed applying an input force as the one given by equation (4.40) with the only front thrusters: with reference to figure (4.3) and to section (4.2.6) this means that the drag coefficients are assumed to be $k_u = (38 \pm 7)Ns/m$, $k_{u|u|} = (333 \pm 24)Ns^2/m^2$ and the efficiency parameter 1. The results of three different experiments labeled SUI1 (SUrge Inertia), SUI2 and SUI3 are reported. In accordance with the input design criteria described in the previous section the applied force, in $Newton$, in each experiments is:

$$f_u = 35 + 25\sin(\frac{2\pi t}{T})$$

being $T = T_1 = 26.8s$, $T_2 = 40.2s$ and $T_3 = 53.6s$ in the SUI1, SUI2 and SUI3 experiments corresponding to frequencies $\upsilon_1 = 0.23Hz$, $\upsilon_2 = 0.16Hz$, $\upsilon_3 = 0.12Hz$. With reference to section (4.2.6) the regime velocity u_0 corresponding to the constant surge force $f_0 = 35N$ can be estimated to be $u_0 \approx 0.2m/s$ so that assuming the drag coefficients to be $k_u = 38Ns/m$ and $k_{u|u|} = 333Ns^2/m^2$ as stated above and the inertia $m \approx 450 + 50\%(450) = 675Kg$ equations (4.37) and (4.39) suggest an optimal input frequency $\omega_{opt} \approx 0.15Hz$. Figure (4.30) shows the data relative to the SUI1 experiment. From the top left plot in clock wise direction the following are displayed: the input force, the $3.3Hz$ sampling rate sonar profiler position measurement, the difference between

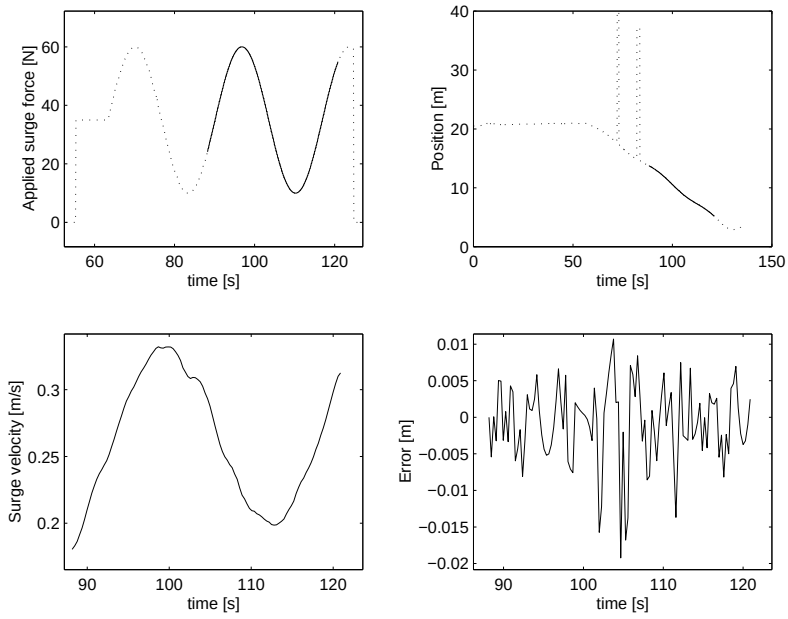

4.30.Surge inertia parameter estimation experimen. For a detailed describiton of the plots refer to the text.

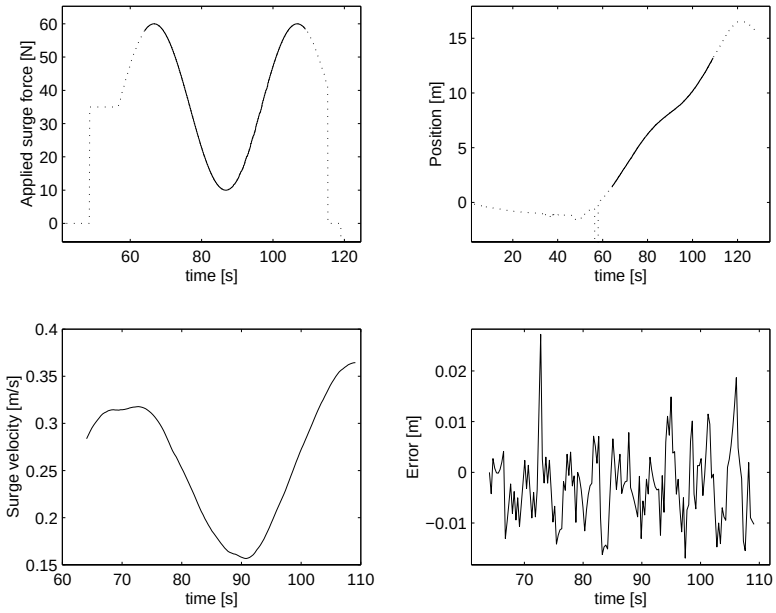

4.31.Surge inertia parameter identification experiment.

the trapezoidal rule numerical integral of the velocity signal (last plot) and the measured position and the velocity signal computed with a Savitzky-Golay off line 4^{th} order filter having a symmetrical window of 21 points. The solid curves in the position and force plots refer to the data actually adopted for the identification process while the dashed ones show the whole batch of data. Notice in the sonar measurement data the presence of two multiple echoes at the beginning of the batch. Applying the LS estimation technique outlined in the previous section to the data of the SUI1 experiment, the inertia parameter is estimated to be

$$\text{SUI1 experiment: } m = (884 \pm 55)Kg$$

being the estimation error computed on the basis of equations (4.12) and (4.6). It is worthwhile remembering that this estimation error calculation method is approximated as the measurement variance σ^2 in equation (4.6) is replaced by its estimated value given by equation (4.12). This is equivalent to the tacit assumption [68] that the fit is "good", i.e. $J_{LS}(\hat{\boldsymbol{\theta}})/\nu \approx 1$ being ν the number of degrees of freedom of the fit. In the present situation the fit is actually quite poor as $J_{LS}(\hat{\boldsymbol{\theta}})/\nu = 687N^2s^2$. As a consequence, and on the basis of the considerations developed in the previous section, the above reported inertia parameter estimation error must be underestimated. This is also confirmed by the scattered values of m obtained processing the data of experiments SUI2 and SUI3:

$$\text{SUI2 experiment} \quad : \quad m = (554 \pm 31)Kg$$

$$\text{SUI3 experiment} \quad : \quad m = (632 \pm 39)Kg$$

and by the large values of the residual costs $J_{LS}(\hat{\boldsymbol{\theta}})/\nu = 676N^2s^2$ (SUI2) and $J_{LS}(\hat{\boldsymbol{\theta}})/\nu = 1032N^2s^2$ (SUI3). Figure (4.31) shows the data relative to the SUI2 experiment. From the top left plot in clock wise direction the following are displayed: the nominal input force, the $3.3Hz$ sampling rate sonar profiler position measurement, the difference between the trapezoidal rule numerical integral of the velocity signal (shown in the last plot) and the measured position and the velocity signal computed with a Savitzky-Golay off line 4^{th} order filter having a symmetrical window of 41 points. The solid curves in the position and force plots refer to the data actually adopted for the identification process while the dashed ones show the whole batch of data.

As pointed out in the previous section the proposed methodology for ROVs inertia parameter identification is very simple, low cost, reasonably fast and based only on standard on board sensors: the major drawback being a relatively large estimation error. Nevertheless as standard ROV manoeuvres are performed with very limited accelerations, the above estimated values of the inertia parameters, although affected by an apparently large estimation error, can be successfully adopted to model the system for filtering and control purposes. To quantitatively evaluate the reliability of the estimated surge model the position measurement data of experiments SUI1 and SUI2 has been compared with the model predicted position relative to the same input forces. In figure (4.32) the position measurement of experiment SUI1 has been plotted with the position predicted by two models having inertias $m = 550Kg$ and $m = 860Kg$ and the drag coefficients fixed to their nominal values $k_u = 38Ns/m$ and $k_{u|u|} = 333Ns^2/m^2$. while in figure (4.33) the position measurement of experiment SUI2 has been plotted with the position predicted by two models having inertias $m = 705Kg$ ($\sim$ mean of $550Kg$ and $860Kg$) and drag coefficients $k_u = 38Ns/m$, $k_{u|u|} = 333Ns^2/m^2$ and $k_u = (38 + 7)Ns/m$, $k_{u|u|} = (333 + 24)Ns^2/m^2$. The position error between the model and the experimental data is remarkably small during the whole length of the trials for both experiments.

4.2.10 Yaw inertia parameter identification

In order to implement the above described methodology for the yaw axis the system time constant τ must be a priori estimated to compute the input torque frequency ω_{opt}. As described in section (4.2.5), the yaw model in the standard yaw rate operating range is linear. Moreover the yaw inertia identification experiments have been performed applying the input torque with a thruster mapping having unit efficiency, i.e., with reference to figure (4.3), the front left (FL) and rear right (RR) thrusters have been used for positive torques and the front right (FR) and rear left (RL) ones have been used for negative torques. As a consequence the considered yaw model is

$$I_z\dot{r} = f - k_r r \tag{4.46}$$

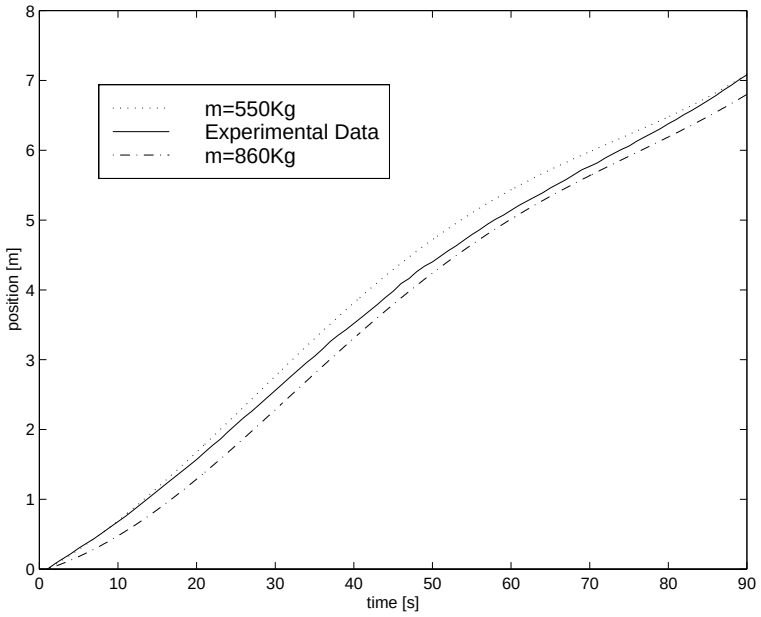

4.32.Experimnetal and simulated data relative to the input force of experiment SUI1. Simulated data refers to the m displayed and $k_u = 38Ns/m$, $k_{u|u|} = 333Ns^2/m^2$.

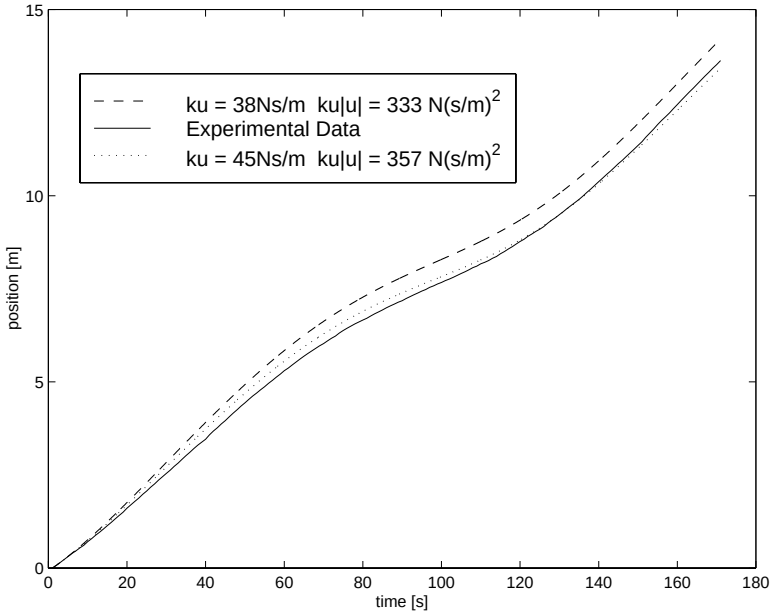

4.33.Experimnetal and simulated data relative to the input force of experiment SUI2. Simulated data refers to $m = 705Kg$ and to the displayed drag coefficients.

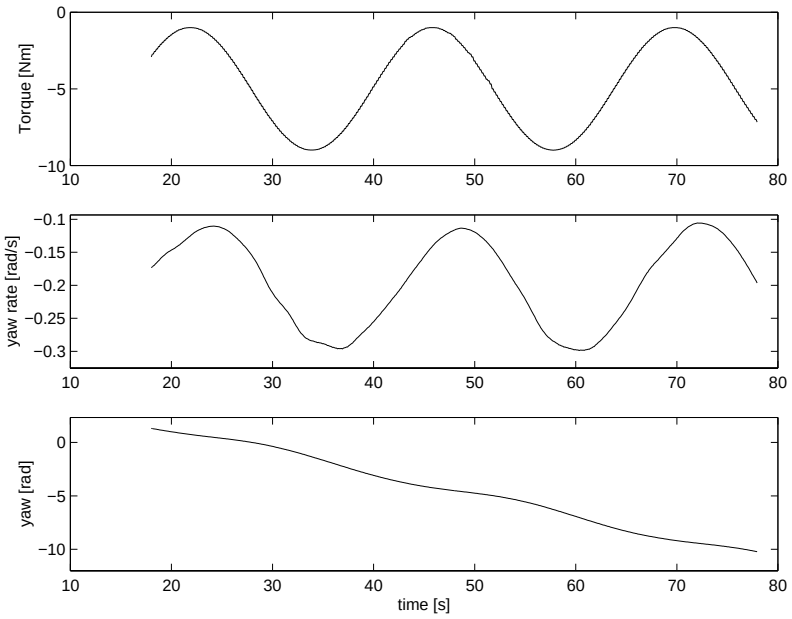

4.34.Yaw inertia parameter identification experimentYAI1.

being I_z ROMEOs z-axis moment of inertia, f the applied torque as given by equation (4.40) and k_r the full efficiency yaw drag coefficient $k_r = 35Nms/rad$. The time constant $\tau = I_z/k_r$ of equation (4.46) can be a priori estimated replacing for I_z the moment of inertia, along the its height, of a parallelepiped having a uniformly distributed $450Kg$ mass, width $1.3m$, length $0.8m$, i.e. $I_z = \frac{1}{12}450(0.8^2 + 1.3^2) \simeq 87.38Kgm^2$. The corresponding input frequency, according to equation (4.39), is

$$\omega_{opt} = \frac{k_r}{\sqrt{3}I_z} \simeq 0.23Hz \tag{4.47}$$

Two different experiments, labeled YAI1 (YAw Inertia) and YAI2, will be considered. During the YAI1 experiment the input torque was provided by the only rear left and front right thrusters (figure (4.3)), so that unit efficiency is assumed to hold for negative velocity and torques. In accordance with equation (4.47), the input torque frequency during the YAI1 experiment has been chosen to be $\omega = 0.26Hz$ and the applied torque f in Nm was

$$f = -5 + 4\sin(0.26t)$$

in order to avoid propeller inversions. The position was measured with a $10Hz$ sampling rate compass and the velocity has been computed with an off line 4^{th} order Savitzky-Golay filter having a symmetric window of full length 41 points. The input torque,

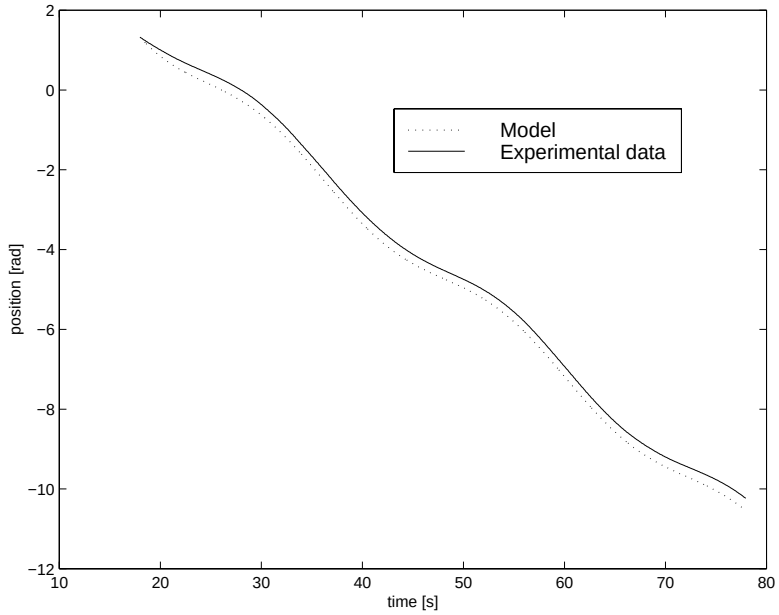

4.35.Experiment YAI1 measured position and expected model position with $k_r = 35Nms/rad$, $I_z = 93Kgm^2$.

the filtered yaw rate and the yaw measurement of the YAI1 experiment are reported in figure (4.34). Implementing the estimation algorithm described in section (4.2.8) yields

$$\text{YAI1 experiment: } I_z = (93.0 \pm 0.6)Kgm^2$$

being the estimation error computed with the usual technique based on equations (4.12) and (4.6) probably underestimated for the reasons outlined in the previous two sections. Nevertheless the identified model performance is acceptable, as shown in figure (4.35) where the experimental position data of experiment YAI1 are compared with the model predicted position. The YAI2 experiment refers to an input torque signal of frequency $\omega = 0.39Hz$ provided by the front left and rear right thrusters. Torque unit efficiency is assumed for positive torques and velocities, so the input torque signal was

$$f = 5 + 4\sin(0.39t)$$

The angular (yaw) position was measured with a $10Hz$ sampling rate compass and, as for the YAI1 experiment, yaw rate has been computed with an off line 4^{th} order Savitzky-Golay filter having a symmetric window of full length 41 points. Applied torque, computed velocity and measured position of experiment YAI2 are reported in figure (4.36). The resulting estimated value of the inertia I_z according to the experiment

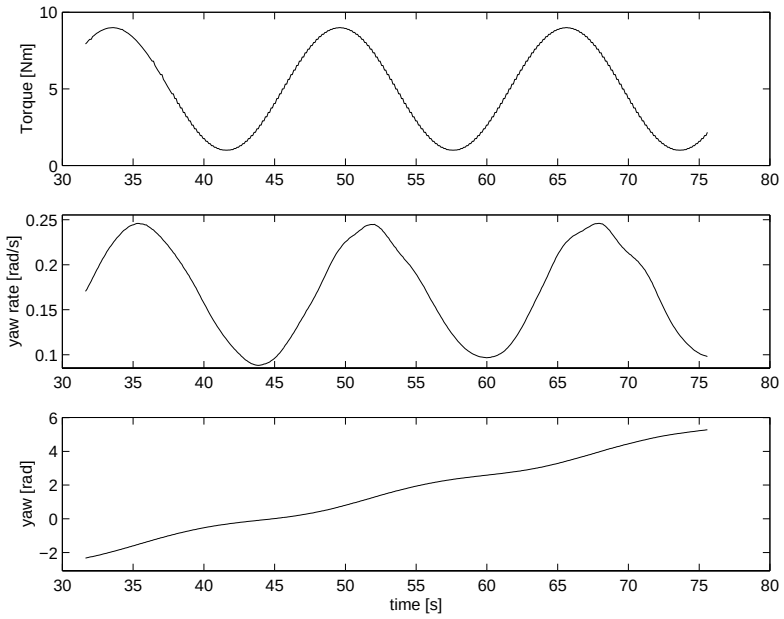

4.36.Yaw inertia parameter identification experimentYAI2.

YAI2 is

$$\text{YAI2 experiment: } I_z = (100.0 \pm 0.7) Kgm^2$$

4.3 Summary

Within this chapter an identification procedure for the drag and inertia parameters of an open frame ROV and the results of its implementation on a real system have been presented. The identification procedure is based on on-board sensor data rather then towing tank experiments. Although in principle towing tank methods allow a better estimation accuracy (in particular of the inertia coefficients), they are usually performed on a scaled model of the vehicle rather then on the real system [73] with all the related drawbacks. Moreover such towing tank methods are much more expensive, complex and time consuming. A simple set of inputs and the relative model fitting technique have been defined for the on board sensor based estimation of drag and inertia coefficients of a decoupled ROV model: the major advantage of the proposed approach consists in the possibility of estimating the propeller-hull and propeller-propeller efficiency parameters that would be otherwise unobservable. Moreover thanks to their simple nature the tests may be repeated when the vehicle changes configuration in or-

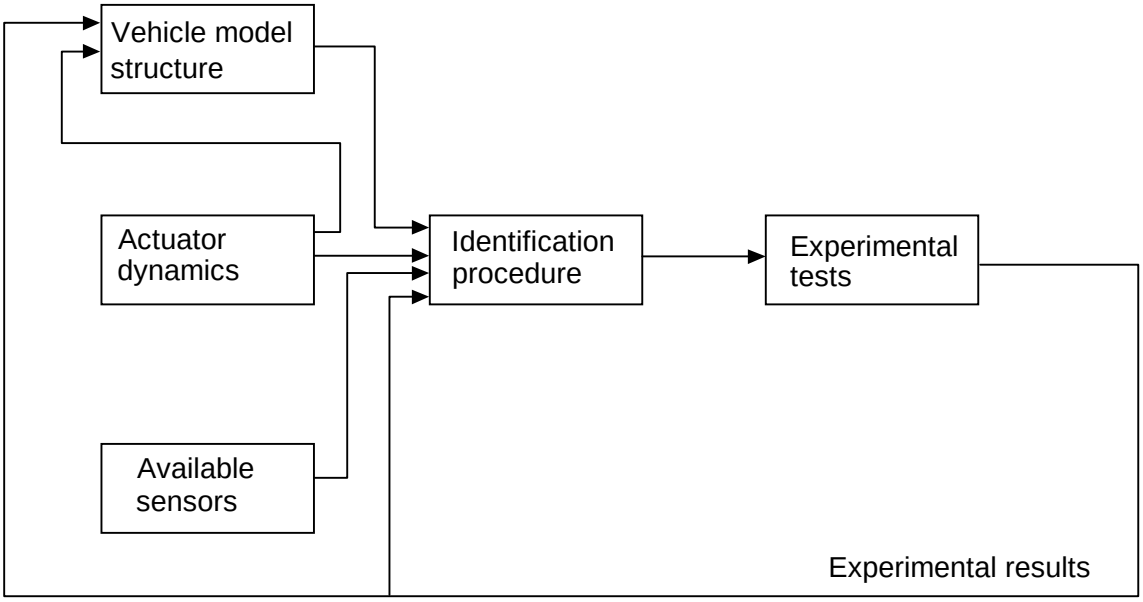

4.37.Rationale of the identification procedure design.

der to tune the control and navigation systems when required. It is worthwhile pointing out that the identification procedure has been designed taking into account the vehicle model structure, the type of available sensors and the actuator dynamics. Moreover during the experimental implementation of such procedure on the ROMEO ROV both the system model and the identification procedure itself have been "tuned" on the basis of the experimental results. The logical flow chart of the work described in this chapter is reported in figure (4.37). The developed procedure has been adopted to estimated the drag and inertia coefficients and their variances for the surge, sway, heave and yaw axis of the ROMEO ROV: the data relative to numerous experimental trials has been processed and the results are reported in detail. It has been shown that yaw drag in the typical operating yaw rate range, i.e. $|\dot{\psi}| \leq 10\,\mathrm{deg}/s$, is better modeled by an only linear term rather then both a linear and quadratic one: this is important as it suggests that as far as the yaw axis is concerned linear control techniques may be successfully adopted. At last it has been shown that the propeller-hull and propeller-propeller interactions may have a most important relevance in the dynamics of open frame ROVs and should thus be taken explicitly into account. To this extent an efficiency parameter, closely related to the thruster installation coefficient described by Goheen et al.[66], has been introduced and its value and variance have been estimated in all the cases of interest.

Chapter 5
Motion control and path planning

In this chapter some original results regarding the motion control and path planning of nonholonomic systems with reference to underwater vehicles will be outlined.

5.1 2D motion control of a nonholonomic vehicle

Three major issues of robot motion control are the state stabilization problem, the path generation problem and the path tracking problem. If the system at hand has nonholonomic constraints, as for wheeled vehicles or under-actuated underwater vehicles, these problems are particularly challenging. The literature regarding the stabilization of nonholonomic systems is very large and, as a detailed overview of the topic goes beyond the possibilities of this work, only the results of interest will be here reported. For a wider discussion of the current state of the art in the control of nonholonomic systems refer to [74] [75] [76]. The main difficulty in the stabilization of nonholonomic systems is related to the theorem of Brockett [77]:

Theorem (Brockett, 1983) *Given* $\dot{q} = G(q)u$ *with* $g(q_0)u_0 = 0$ *and* $g(\cdot)$ *continuously differentiable in a neighborhood of* q_0*, then there exists a time invariant continuously differentiable control law which makes* (q_0, u_0) *asymptotically stable if and only if* $\dim(q) = \dim(u)$.

Indeed many systems of practical interest may not be asymptotically stabilized via smooth time invariant feedback due to this result. Among these the unicycle kinematic model:

$$\begin{aligned} \dot{x} &= u\cos\phi \\ \dot{y} &= u\sin\phi \\ \dot{\phi} &= \omega \end{aligned} \tag{5.1}$$

being x, y the Cartesian coordinates with respect to the inertial frame $< 0 >$, u the linear velocity, ϕ the orientation with respect to the x-axis and ω the angular velocity as shown in figure (5.1). To tackle this difficulty most authors have focused their attention either on smooth but time varying state feedback approaches, or on time independent but noncontinuous state feedback approaches. As far as underwater vehicles are concerned examples of such control laws are provided by Egeland et al.[78] and Pettersen et al.[79]. A most interesting way of analyzing the asymptotic stabilization of the unicycle model given by equation (5.1) is related to a remark of the above cited Brockett Theorem given

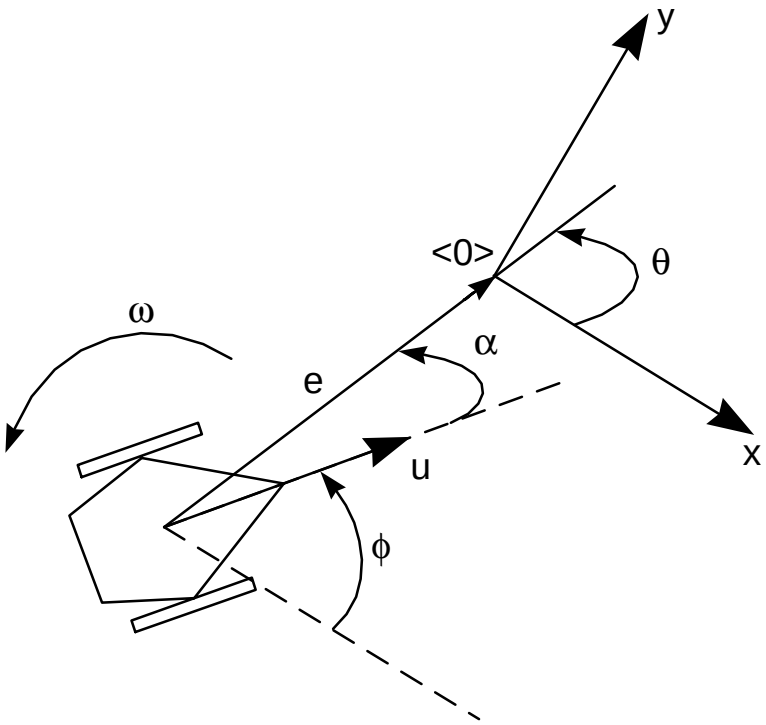

5.1.Unicycle kinematics

by the same Brokcett [77]: *"If we have*

$$\dot{q} = \sum_{i=1}^{m} g_i(q) u_i : q(t) \in \Re^n$$

with the vectors $g_i(q)$ *being linearly independent at* q_0 *then there exists a solution to the stabilization problem if and only if* $m = n$*. In this case we must have as many control parameters as we have dimensions of* q*. Of course the matter is completely different if the set* $\{g_i(q_0)\}$ *drops dimension precisely at* q_0*."* As shown by the works of Casalino et al.[1] and Badreddin et al.[80] , this last observation plays a key role in the solution of the unicycle stabilization problem: if the unicycle kinematics is represented in polar-like coordinates

$$\begin{aligned} e &\triangleq \sqrt{x^2 + y^2} \\ \theta &\triangleq ATAN2(-y, -x) \\ \alpha &\triangleq \theta - \phi \end{aligned} \tag{5.2}$$

as shown in figure (5.1) Brocketts Theorem does not hold anymore as the state itself is not defined for $e = 0$. With this choice of the state variables the state equations are

$$\begin{aligned} \dot{e} &= -u \cos\alpha \\ \dot{\alpha} &= -\omega + u\frac{\sin\alpha}{e} \\ \dot{\theta} &= u\frac{\sin\alpha}{e} \end{aligned} \tag{5.3}$$

and a smooth time invariant state feedback law for global asymptotic stability is not prevented by Brocketts result. Examples of such possible control laws are reported in [1] [2] and [80]. Indeed the idea of simply adopting a different state representation in which Brocketts Theorem does not hold to solve the smooth state feedback global stability problem for general models of nonholonomic systems is very appealing and has been dealt by A. Astolfi [81].

5.1.1 A state feedback solution for the unicycle model

Casalino et al.[1] presented the smooth feedback law

$$u = \gamma\, e \cos\alpha : \gamma > 0 \tag{5.4}$$

$$\omega = k\alpha + \gamma \cos\alpha \frac{\sin\alpha}{\alpha}(\alpha + h\theta) : k, h > 0 \tag{5.5}$$

that globally stabilizes the unicycle system given by equation (5.3) in the origin. A major draw back of this result that prevents its straightforward application to the control of the planar motion of real systems as underwater or air vehicles equipped with actuators

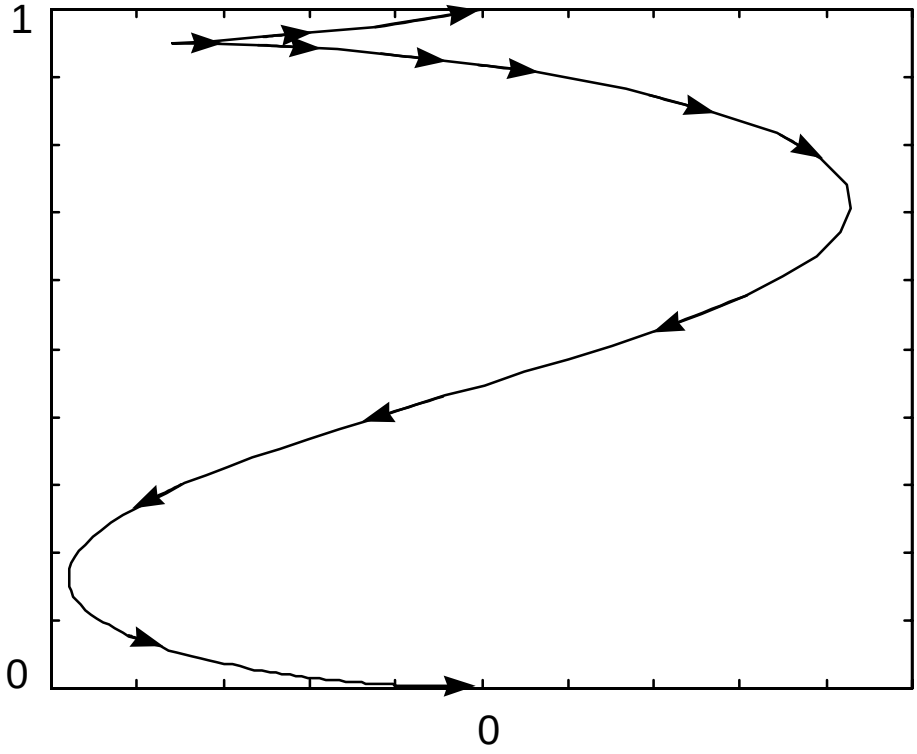

5.2.Initial position $(0, 1)$ with orientation $\phi = \pi/4$.

in only one direction is the unicycle-like nonholonomic constraint according to which angular velocity can be assigned independently. This is equivalent to the obvious statement that a unicycle-like vehicle can turn on itself thus moving on an infinite curvature trajectory, while a wider class of moving systems (like bicycles, cars, torpedoes or airplanes) can only move on bounded curvature paths. To have a qualitative understanding of the behaviour of the above algorithm (equations (5.4) and (5.5)) refer to figures (5.2) and (5.3). Notice that within the unicycle-like approach of Casalino et al.[1] given by equations (5.4) and (5.5) the velocity u can take both positive and negative signs: indeed the resulting path inversion points correspond to null linear velocity u. Moreover the closed loop equation for the position error e is

$$\dot{e} = -\gamma e \cos^2 \alpha$$

showing that e is always decreasing. This is certainly a most interesting aspect of the above outlined algorithm as it guarantees exponential convergence of e. As described in the papers of Caccia et al.[28] [30] and Casalino et al.[82] the control strategy given by equations (5.4) and (5.5) can be successfully adopted for the planar motion control of underwater vehicles that can steer having null surge velocity ($\omega \neq 0, u = 0$), but in

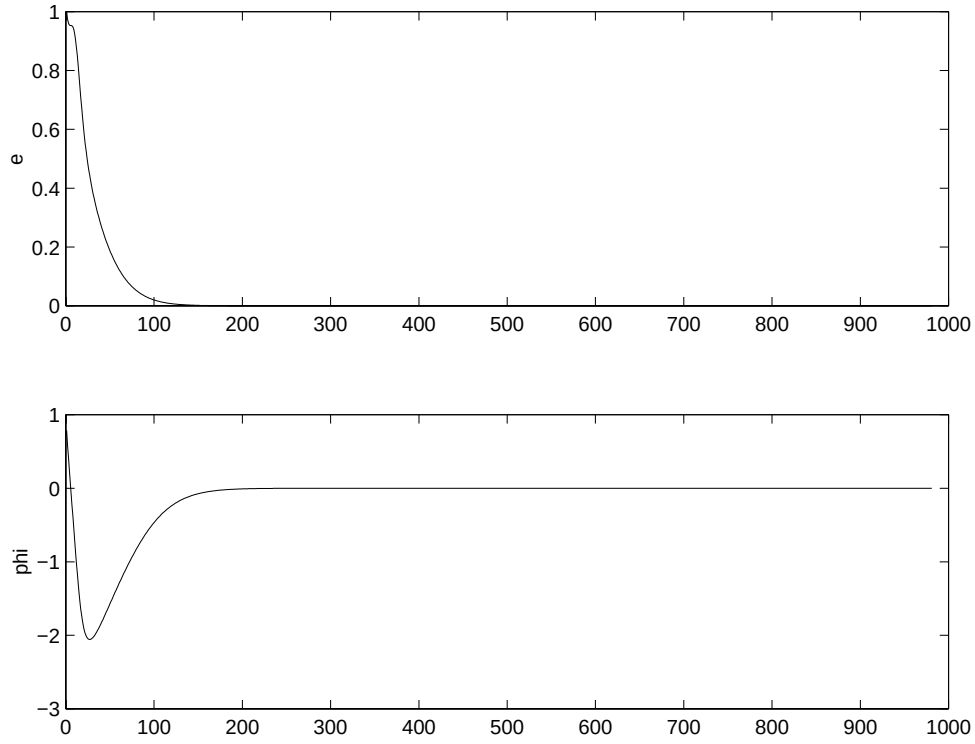

5.3.Errror e and orientation ϕ with respect to time relative to the previous figure.

many underwater vehicle applications the system can (or is preferred to) move in the only forward direction and can not turn with $u = 0$. With these ideas in mind the above outlined approach can be modified to introduce the (bounded) curvature explicitly in the model and to prevent inversions in the sign of the linear velocity u.

5.1.2 A state feedback solution for a more general model

A simple way to introduce the curvature in the unicycle model is to consider the bicycle-like kinematics given, in Cartesian coordinates, by

$$\begin{aligned} \dot{x} &= u\cos\phi \\ \dot{y} &= u\sin\phi \\ \dot{\phi} &= uc \end{aligned} \tag{5.6}$$

being the control signals u and the curvature c. With the polar-like variable choice given in equation (5.2) this model is transformed in the following:

$$\begin{aligned} \dot{e} &= -u\cos\alpha \\ \dot{\alpha} &= -u\left(c - \frac{\sin\alpha}{e}\right) \\ \dot{\theta} &= u\frac{\sin\alpha}{e} \end{aligned} \tag{5.7}$$

Notice that within this model the linear velocity u can not change sign, as when $u = 0$ the state stops moving. Thus in order to converge to the origin of the state space, u can take the null value only in the target state $(0, 0, 0)$. In order to design a globally stable smooth state feedback control law for the system given by equation (5.7) a Lyapunov-like based approach will be followed. The control law synthesis method is inspired by and closely related to the previous works of Casalino et al.[1] and Aicardi et al.[2]. Having noticed that the state equation (5.7) derivative is identically null when $u = 0$ suggests to try the control law

$$u = \gamma e : \gamma > 0 \tag{5.8}$$

The point is now to guarantee, by a suitable choice of c, that within some finite time $\cos\alpha < 0$ (so that e starts decreasing) and asymptotically $(e, \alpha, \theta) \rightarrow (0, 0, 0)$. To calculate c consider the state equation (5.7) given (5.8), i.e.,

$$\begin{aligned} \dot{e} &= -\gamma e\cos\alpha \\ \dot{\alpha} &= -\gamma e\left(c - \frac{\sin\alpha}{e}\right) \\ \dot{\theta} &= \gamma\sin\alpha \end{aligned} \tag{5.9}$$

and the quadratic Lyapunov candidate function

$$V = \frac{1}{2}(\alpha^2 + h\theta^2) : h > 0 \tag{5.10}$$

having time derivative

$$\dot{V} = \alpha\dot{\alpha} + h\theta\dot{\theta} = \gamma(\alpha \sin\alpha + h\theta \sin\alpha - \alpha ec) \tag{5.11}$$

This last equation suggests the choice of c as:

$$c = \frac{\sin\alpha}{e} + h\frac{\theta}{e}\frac{\sin\alpha}{\alpha} + \beta\frac{\alpha}{e} : \beta > 0 \tag{5.12}$$

so that the time derivative of the candidate Lyapunov function V becomes

$$\dot{V} = -\gamma\beta\alpha^2 \leq 0 \tag{5.13}$$

As in the model of Casalino et al. [1] and as will be shown in the sequel, the h parameter in equation (5.10) is needed to guarantee that $\lim_{(e,\alpha)\to(0,0)} c = 0$. Moreover being V positive and radially unbounded equation (5.13) implies that it tends towards a non-negative finite limit, thus

$$\begin{aligned} \lim_{t\to\infty} \alpha &= \bar{\alpha} \\ \lim_{t\to\infty} \theta &= \bar{\theta} \end{aligned}$$

The above and the fact that $\dot{V}$ is uniformly continuous[5] imply by Barbalat's Lemma that $\dot{V}$ tends to zero, so that $\bar{\alpha} = 0$. Substituting equation (5.12) in (5.9) gives:

$$\begin{aligned} \dot{e} &= -\gamma e \cos\alpha \\ \dot{\alpha} &= -\gamma\left(\beta\alpha + h\theta\frac{\sin\alpha}{\alpha}\right) \\ \dot{\theta} &= \gamma \sin\alpha \end{aligned} \tag{5.14}$$

From the facts that $\alpha \to 0$, $\theta \to \bar{\theta}$, and that $\dot{\alpha}$ is uniformly continuous, again by Barbalat's Lemma it follows that the limit

$$\lim_{t\to\infty} \dot{\alpha} = -\gamma h\bar{\theta} = 0$$

and thus the limit value $\bar{\theta}$ of θ must be zero. Moreover notice from the last of equations (5.14) that given the above results also $\dot{\theta}$ tends asymptotically towards zero. The above

[5] $\ddot{V} = -2\gamma\beta\alpha\dot{\alpha}$ is bounded.

results show that

$$\begin{aligned} \alpha &\rightarrow 0 \; ; \dot{\alpha} \rightarrow 0 \\ \theta &\rightarrow 0 \; ; \dot{\theta} \rightarrow 0 \end{aligned}$$

so as $t \rightarrow \infty$ there must be some finite value of t, say t^*, starting from which $\cos\alpha < 0$ and thus

$$\dot{e} \rightarrow -\gamma e < 0 \Rightarrow e \rightarrow 0$$

The behaviour of the above developed closed loop control, i.e.,

$$\begin{cases} u = \gamma e : \gamma > 0 \\ c = \dfrac{\sin\alpha}{e} + h\dfrac{\theta}{e}\dfrac{\sin\alpha}{\alpha} + \beta\dfrac{\alpha}{e} : \beta, h > 0 \end{cases} \tag{5.15}$$

depends on the choice of the parameters γ, β, h. In particular while u is obviously limited as long as e and γ are finite, the limit $\lim_{(e,\alpha,\theta)\rightarrow(0,0,0)} c$ must be analyzed: when the state (e, α, θ) approaches the origin $(0, 0, 0)$ the state equations (5.14) can be approximated by the linear system

$$\begin{pmatrix} \dot{\alpha} \\ \dot{\theta} \end{pmatrix} = \begin{bmatrix} -\gamma\beta & -h\gamma \\ \gamma & 0 \end{bmatrix} \begin{pmatrix} \alpha \\ \theta \end{pmatrix} \tag{5.16}$$

$$\dot{e} = -\gamma e \tag{5.17}$$

and

$$c = \frac{\alpha}{e}(1+\beta) + h\frac{\theta}{e}$$

so that in order to reach the target $(0, 0, 0)$ on a straight line (i.e. with null curvature) the real part of the dominant pole of equation (5.16) must be strictly larger then γ. By direct calculation the eigenvalues of the system matrix of equation (5.16) are

$$\lambda_{\pm} = \frac{1}{2}\left(-\gamma\beta \pm \sqrt{\gamma^2\beta^2 - 4h\gamma^2}\right) \tag{5.18}$$

so the requested condition $|\,\mathrm{Re}(\lambda_+)| > \gamma$ is equivalent to

$$h > 1 \; ; \; 2 < \beta < h + 1$$

Moreover by direct analysis of equation (5.18) it follows that if $h > 1$

$$\Delta \leq 0 \Longleftrightarrow \beta \leq 2\sqrt{h}$$

being $\Delta = \gamma^2\beta^2 - 4h\gamma^2$ so that the system is stable and under damped for $2 < \beta < 2\sqrt{h}$, stable and critically damped for $2 < \beta = 2\sqrt{h}$, stable and over damped for $2\sqrt{h} < \beta < h + 1$. If $h > 1$ and $\beta < 2 \cup \beta > h + 1$ or if $h = 1 \; \forall \; \beta$ the curvature diverges as the target state is approached, thus the importance of the h parameter in equation (5.10).

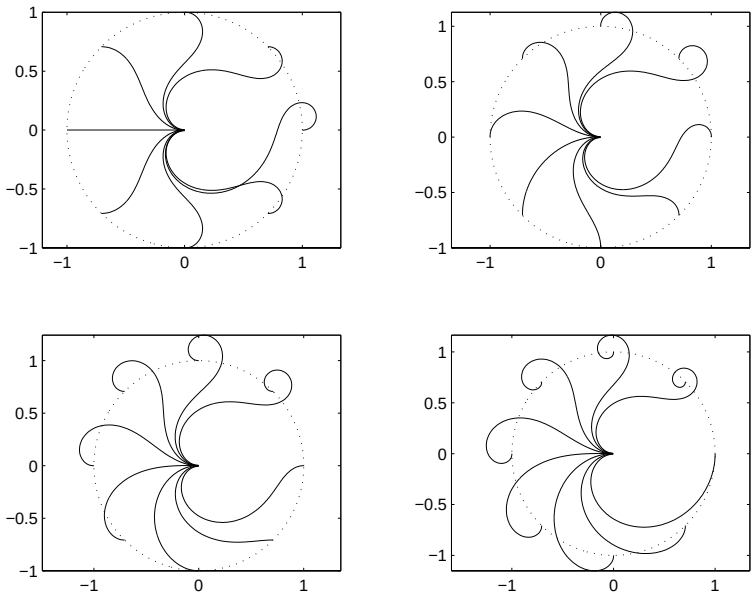

5.4.Paths starting on the unit circle with gains $\gamma = 1,\ h = 2,\ \beta = 2.91$. From left to right and from top to bottom the starting orientation ϕ_0 is: 0, $\pi/2$, π, $3\pi/2$.

A most important property of the proposed algorithm is the boundedness of the control input c. Equation (5.15) shows that $|c| \leq \frac{h\pi+1+\beta|\alpha_{max}|}{e_{min}}$ and that c tends to zero as e grows. The above linear analysis shows that if the gains β and h are suitably chosen c tends to zero also as (e, α, θ) tends to zero. Moreover notice that the linearized system given by equations (5.16) and (5.17) actually holds for small values of α and whatever e and θ are, as the only adopted approximation has been $\sin\alpha \simeq \alpha$ and $\cos\alpha \simeq 1$. As a consequence the only requirement necessary for c to be minor than a prescribed upper bound during the whole state trajectory, is that during the convergence of α in the state space region where $\sin\alpha \simeq \alpha$, the error e is kept larger then some limit value e_{min}. Intuitively this means that if an upper bound $\bar{c}$ is given on c, as in most real systems, the initial error e_0 must be larger then some limit value $e^*(\alpha_0, \theta_0, \bar{c})$ depending on the initial values of α and θ and on $\bar{c}$.

For a qualitative understanding of the resulting paths refer to figures (5.4) and (5.5). In figure (5.4) various paths starting on the unit circle with different orientation are displayed, while figure (5.5) shows the influence of a 2π difference on the initial angular position ϕ_0 on the path. With reference to the above reported stability analysis, all the simulations reported in figures (5.4) and (5.5) are relative to gain values that guarantee a stable and over damped convergence of c to zero, in particular $\gamma = 1$, $h = 2$, $\beta = 2.91$.

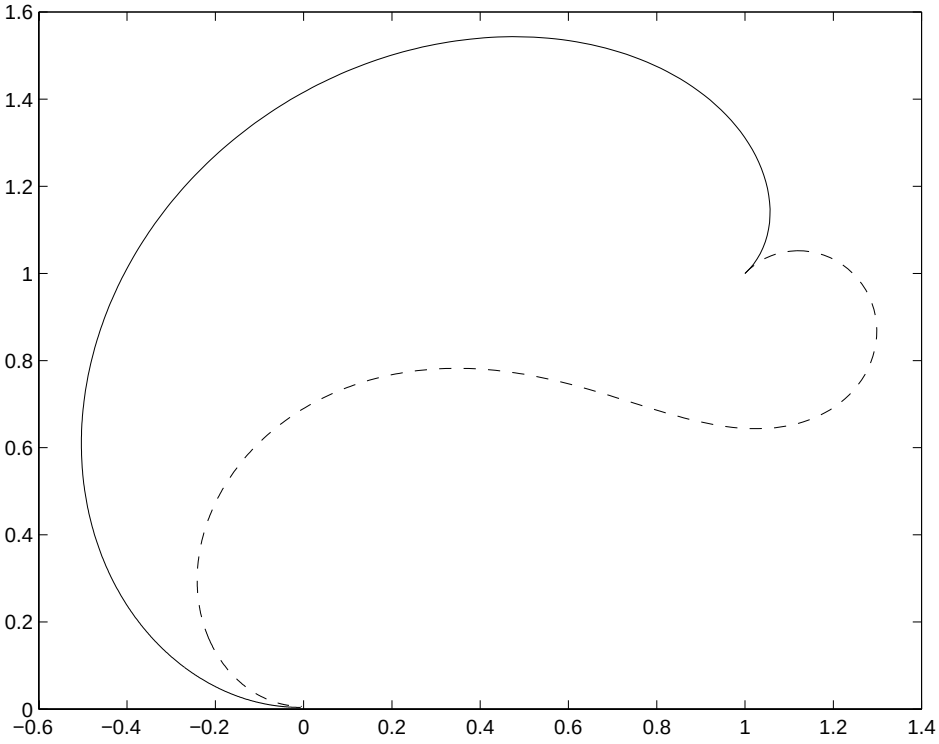

5.5.Paths starting in $(1,1)$ with orientations $\phi_0 = \pi/4$ (dashed line) and $\phi_0 - 7\pi/4$ (solid line) with gains $\gamma = 1,\ h = 2,\ \beta = 2.91$.

The convergence to zero of α, θ, ϕ, u and c for the two paths reported in figure (5.5) is shown in figures (5.6) and 5.7). The developed control strategy can be adopted either for path tracking of a given 2D curve, or to navigate among via points or to design an autonomous navigation algorithm: a simple path tracking controller can be realized assuming that the target state space point $(0,0,0)$ moves along the desired curve. This approach has been analyzed by Aicardi et al.[2] for the unicycle model (equation (5.3)) with the control law given by equations (5.4) and (5.5) and can be extended to the kinematic model equation (5.7) controlled by equations (5.15) with minor changes. As far as autonomous navigation is concerned, the proposed control strategy is appealing being globally convergent and requiring only position and orientation errors that can be reasonably measured by standard on board vehicle sensors. Yet for a practical implementation on real systems two aspects of the proposed control law must be considered: the maximum vehicles curvature radius and actuator saturation. The curvature upper bound constraint can be managed assuming to approach the target form a sufficiently

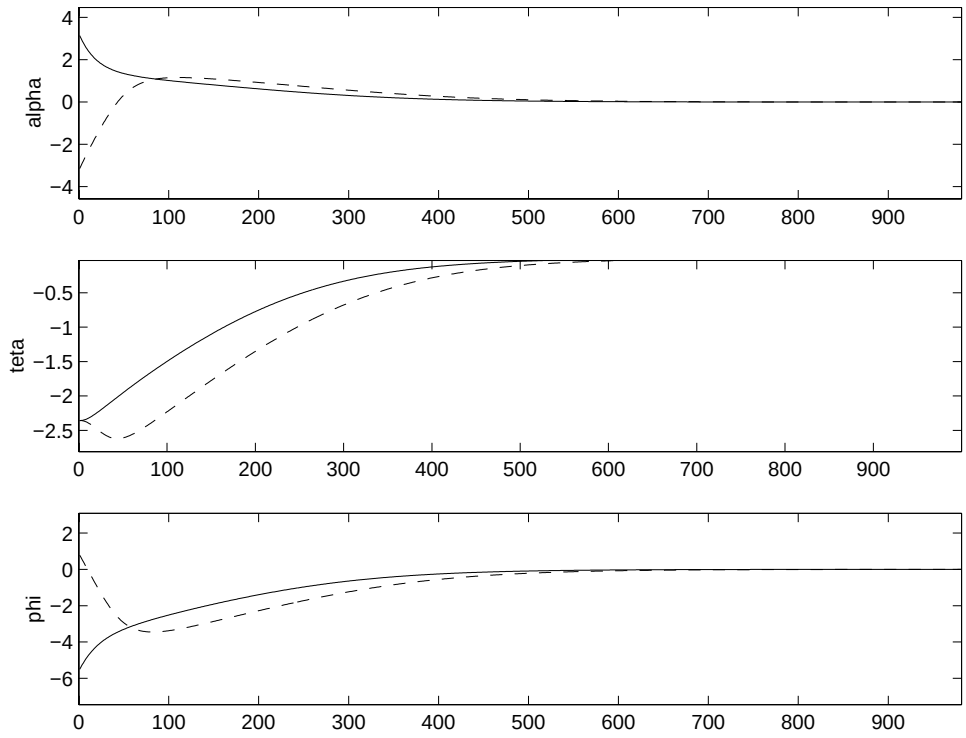

5.6.Convergence of α, θ, ϕ for the paths starting in (1,1) with initial orientation $\phi_0 = \pi/4$ (dashed lines) and $\phi_0 = -7\pi/4$ (solid lines).

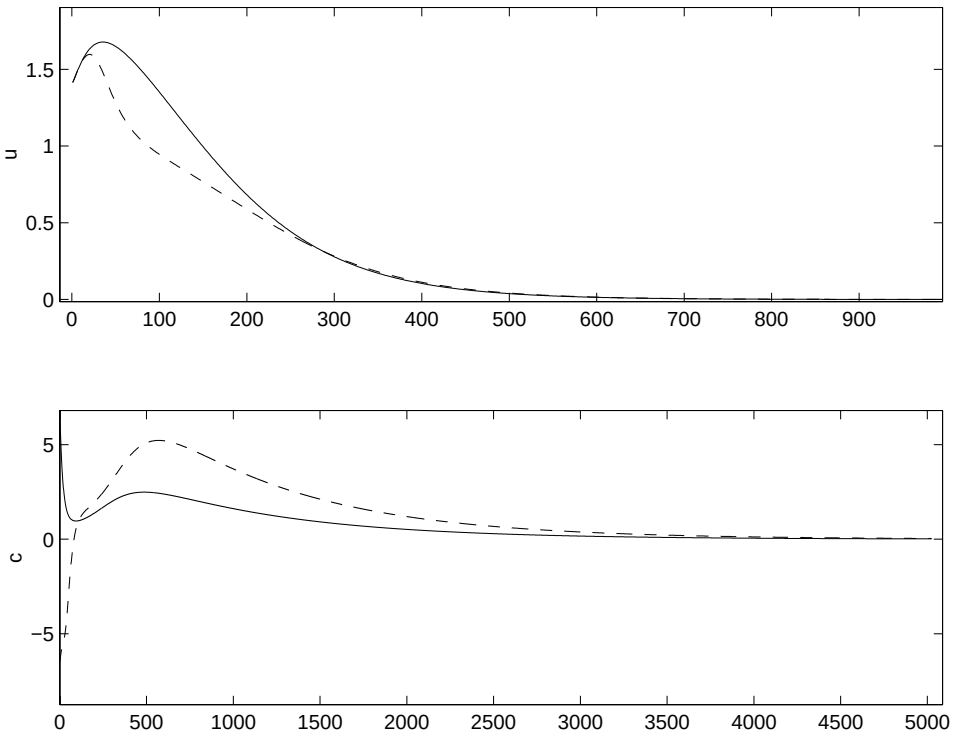

5.7.Convergence of c and u for the paths starting in $(1, 1)$ with initial orientations $\phi_0 = \pi/4$ (dashed lines) and $\phi_0 = -7\pi/4$ (solid lines). Notice the different time scales of the convergence of u and c.

distant point. As discussed above, if α converges to a region where $\sin\alpha \simeq \alpha$ being e greater then some limit $e^*(\alpha_0, \theta_0, \bar{c})$, then c will converge to zero without ever exceeding some prescribed upper bound $\bar{c}$. Actuator saturation must be considered with reference to the proportional control law $u = \gamma e$ equation (5.8). Notice that as long as γ is strictly positive, the value of γ does not affect the convergence properties of the state (as h and β do) but only the convergence rate, so one could argue that choosing γ sufficiently small can always avoid saturation problems. Indeed in some applications, as the path tracking problem where the moving target is always reasonably close, this is the most simple way of dealing with saturation, but in other circumstances, as autonomous navigation on long distances, it is not. The point is then to understand if and how actuator saturation due to $u = \gamma e$ affects the convergence of the state to the target $(0, 0, 0)$ and eventually design a different bounded control law for u. Actuator saturation occurring with a straight forward implementation of equations (5.15) can be modelled as:

$$u = \gamma e \; sat(\gamma e, \bar{u}) : \gamma > 0 \tag{5.19}$$

being sat a discontinuous function defined as

$$sat(x, y) = \begin{cases} 1 \; \forall \; |x| < y \\ \frac{y}{|x|} \; \forall \; |x| \geq y \end{cases} \quad \forall \; y > 0 \tag{5.20}$$

that models a *hard* saturation of u. With only marginal technical differences related to the discontinuity of $sat(\gamma e, \bar{u})$ for $\gamma e = \bar{u}$, the whole control law design procedure going form equation (5.9) to equation (5.15) can be replicated replacing $\gamma e \; sat(\gamma e, \bar{u})$ to γe: as a result equations (5.9), (5.11), (5.13) and (5.14) should be multiplied by $sat(\gamma e, \bar{u})$ and this will not affect either the global stability properties or the convergence analysis of $c \to 0$ developed for the unsaturated case as long as e is finite and $\bar{u} > 0$ (obvious). Indeed this is a satisfactory result as it suggest that a straight forward implementation of equations (5.15) will guarantee convergence even in presence of a *hard* saturation on u as the one modelled by equation (5.19). As an example the simulation shown in figure (5.5) relative to the starting configuration $(1, 1, -7\pi/4)$ with gains $\gamma = 1$, $h = 2$, $\beta = 2.91$ has been repeated with the same gains saturating the linear velocity u to 0.5, i.e. $\bar{u} = 0.5$ in equation (5.19). The resulting path and the values of α, θ, ϕ, u and c for the saturated and unsaturated cases are reported in figures (5.8) and (5.9). Another way of approaching the saturation problem is to choose a smooth and bounded control law for u compatible with the actuator dynamics. Perhaps the most simple choice is to compute u as:

$$u = \frac{\gamma e}{\frac{e}{a} + 1} \tag{5.21}$$

so that, as shown in figure (5.10), u is smooth (*soft* saturation), bounded by γa and linear in e when $e \ll a$. Replacing equation (5.21) in equation (5.9) and computing V

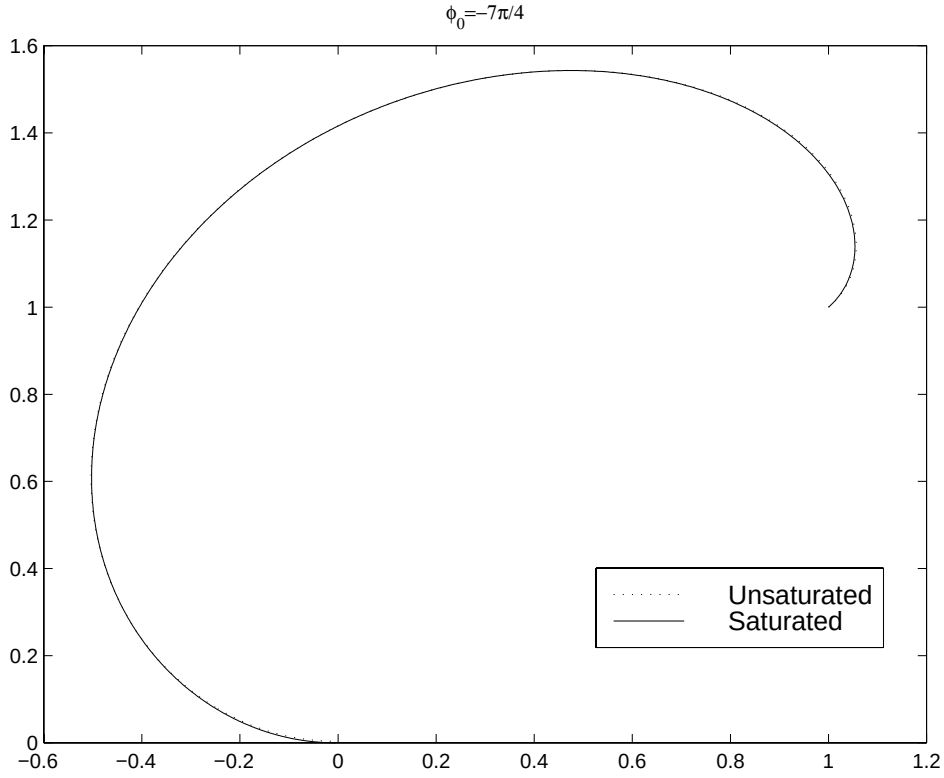

5.8.Paths with saturated (solid line) and unsaturated (dashed line) u. Refer to text for details.

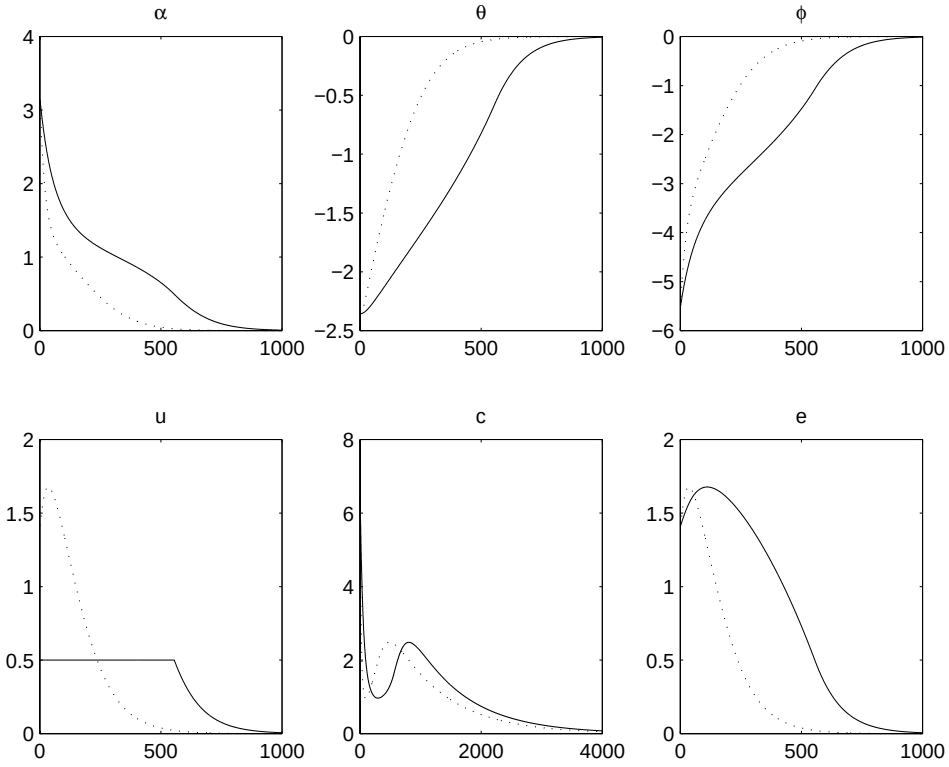

5.9.Saturated ($\bar{u} = 0.5$, solid lines) and unsaturated (dashed lines) results for the same initial configuration ($1, 1, -7\pi/4$) and same gains $\gamma = 1$, $\beta = 2.91$, $h = 2$.

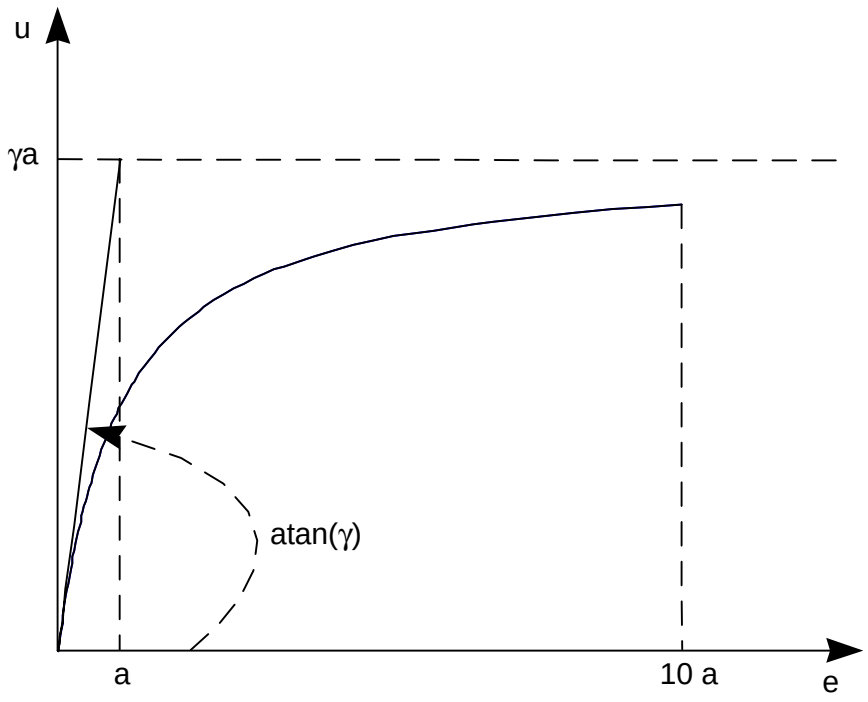

5.10.Saturated velocity input signal u.

and $\dot{V}$ gives

$$\begin{aligned} \dot{e} &= -\frac{\gamma e}{e/a+1}\cos\alpha \\ \dot{\alpha} &= -\frac{\gamma e}{e/a+1}\left(c-\frac{\sin\alpha}{e}\right) \\ \dot{\theta} &= \frac{\gamma}{e/a+1}\sin\alpha \end{aligned} \tag{5.22}$$

$$\begin{aligned} \dot{V} &= \frac{d}{dt}(\frac{1}{2}\alpha^2+h\theta^2) = \alpha\dot{\alpha}+h\theta\dot{\theta} = \\ &= \frac{\gamma}{e/a+1}(\alpha\sin\alpha+h\theta\sin\alpha-ce\alpha) \end{aligned}$$

which suggests to choose c as

$$c=\left(\frac{\sin\alpha}{e}+h\frac{\theta}{e}\frac{\sin\alpha}{\alpha}+\beta\frac{\alpha}{e}\right)(e/a+1):\beta>0 \tag{5.23}$$

With such a choice of c the derivative of the candidate Lyapunov function V is once again given by equation (5.13) and the whole global stability analysis described above for the unsaturated $u=\gamma e$ control law can be easily replicated: the conclusion is that the system given by equation (5.7) is globally asymptotically stable under the action of the control signals u and c given by equations (5.21) and (5.23) (or equations (5.15)). Indeed when $e \ll a$ the two control strategies are identical an so are the stability properties of the system. On the contrary when $e \gg a$ the linear velocity u tends to its upper bound γa (rather then to infinity) and c tends to the finite, but not null, value of:

$$\lim_{e\to\infty} c=\frac{1}{a}\left(\sin\alpha+h\theta\frac{\sin\alpha}{\alpha}+\beta\alpha\right)$$

This shows that the a parameter must be tuned keeping into account a trade off between the maximum allowed linear speed γa and the maximum allowed curvature. Notice however that the curvature of the path generated by the controls given by equations (5.23) and (5.21) will generally be larger then the curvature relative to the unsaturated scheme: indeed the curvature given by equation (5.23) is the same one given by equations (5.15) multiplied by $(e/a+1)>1$. The bounded, smooth and "slow" dependence of u from e given by equation (5.21) is payed in terms of a larger curvature. This is clearly visible in the simulation results shown in figures (5.11) (5.12).

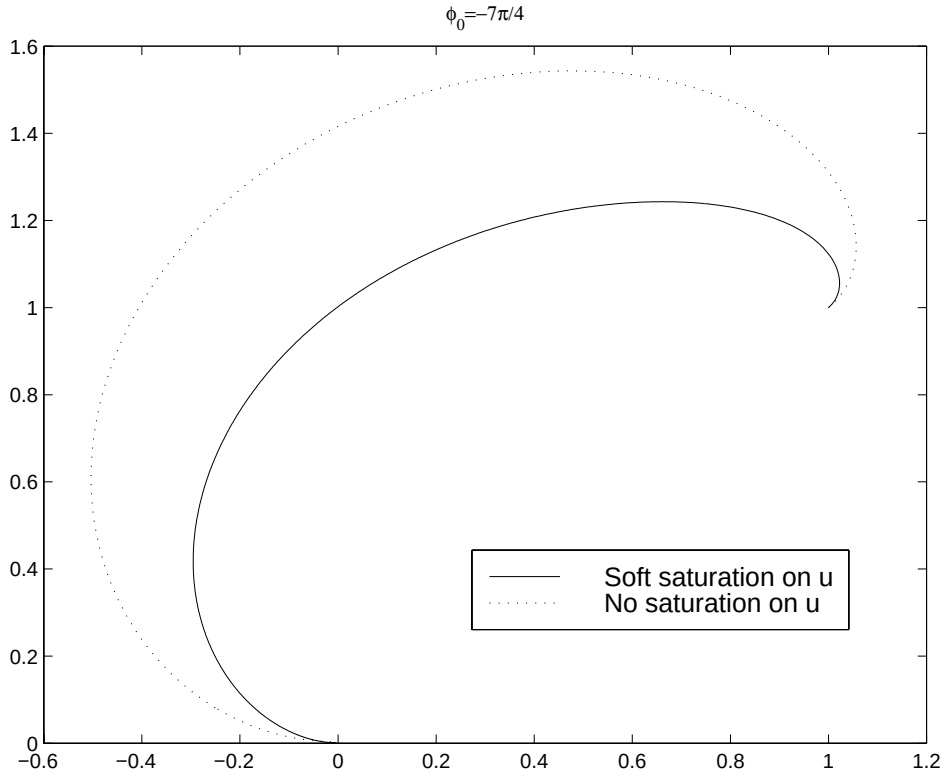

5.11.The solid and dashed line paths correspond to the implementation of the *soft* saturation scheme being $a = 1$, $\gamma = 0.8$, $h = 2$, $\beta = 2.91$ and the unsaturated scheme being $\gamma = 1$, $h = 2$, $\beta = 2.91$.

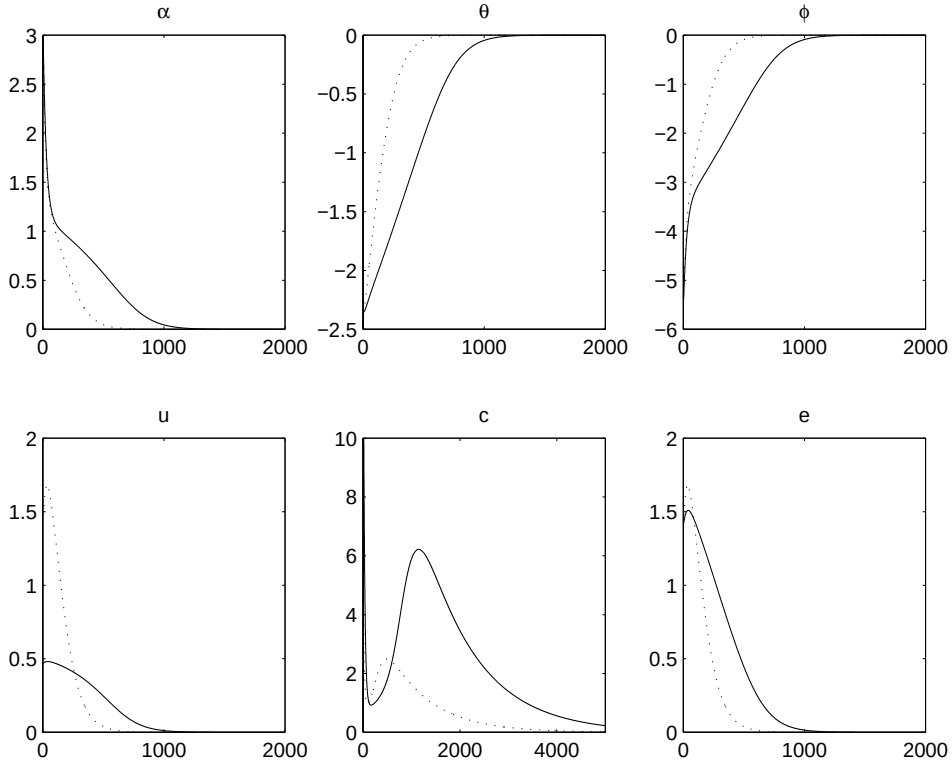

5.12.The solid and dashed lines are relative to the *soft* saturation scheme and to the unsaturated scheme of the paths shown in the previous figure.

5.2 Path Planning

Having developed a time invariant control law that globally and asymptotically stabilizes the car like systems given by equation (5.7) in the origin, attention is now focused on the path planning problem. As discussed by Aicardi et al.[2] for the unicycle model, assuming the target to move on a reference path such control scheme can be successfully employed to design a path tracking controller. The point is thus to generate a suitable reference path. In order to better define what should be considered a "suitable" reference path, some notation must be introduced. In the following a *configuration* will denote the vector describing the position and orientation at a certain time of the given system. The configuration of a $2D$ vehicle is given, e.g., by a $3D$ vector (x, y, ϕ) as shown in figure (5.1). Consider an elongated rigid body in a fluid environment as an open frame ROV, a slender body AUV, or a laminar plate grasped by a robotic manipulator moving (for simplicity) in the plane $z = 0$ (refer to figure (5.13)): as discussed in chapter 3 neglecting time varying currents the hydrodynamic load in deep water ($\geq 5m$) where wave effects are virtually absent is due to drag, lift and added mass forces. Drag is anti-parallel to the velocity and drag coefficients are proportional to the surface of attach. Lift is normal to the velocity direction, proportional to its value and to the angle of attach provided it is small enough ($\leq 12^o$ as an order of magnitude, stall occurs for higher values). Added mass forces are proportional to accelerations $\frac{du}{dt}, \frac{dv}{dt}, \frac{dr}{dt}$ through added mass coefficients which depend on the body's shape. To avoid large sway drag forces and surge added mass forces that cause major hydrodynamic load on an elongated body the lateral sway velocity v and the linear acceleration $\frac{du}{dt}$ should be kept null. Notice that the constraint on null sway makes the present problem very similar to the nonholonomic car-like path planning problem. Yaw velocity r and acceleration $\frac{dr}{dt}$ should be minimized as the large lateral surface produces strong moments along the z axis. Lift forces can be controlled through the value of surge velocity u. Thus assuming that $v = 0$ and that surge u velocity is kept constant and small to avoid added mass stresses and limit lift effects, the major dissipative force acting on the body will be caused by drag rotation moment in the z direction that at low speeds (see chapter 4) is linear in r. The energy associated with such drag moment is proportional to $\int r d\theta = \int r \frac{d\theta}{ds} ds = \int r k ds = u \int k^2 ds$ where s is the curvilinear coordinate, $k = r/u$ the paths curvature and u the constant surge velocity. This calculation suggests to consider the minimization of the cost function $J_I = \int k^2 ds$ with fixed boundary configurations as a path design criterion. Notice that such criterion produces smooth paths that are, as far as their "elastic energy" is concerned, the closest possible to a straight line. This makes the suggested criterion appealing also for wheeled land robots and indeed the problem of finding a smooth and minimum curvature trajectory between two given configurations has received a very wide attention in the robotic literature, specially regarding the steering of nonholonomic mobile robots. From the pioneering work of Dubins [83] who calculated the shortest path of bounded curvature among two configurations, many other authors focused their attention on the generation of bounded curvature $2D$ paths. In synthesis Dubins' results state

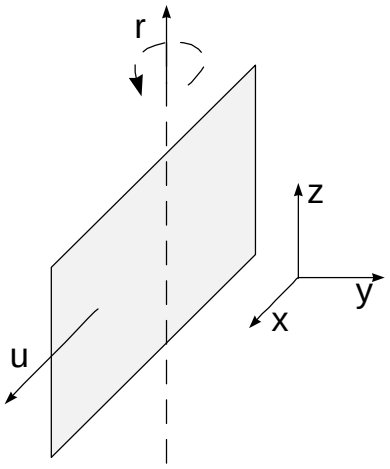

5.13.Laminar plate moving at constant z and with fixed yaw axis direction parallel to z.

that the shortest $2D$ path of bounded curvature between to fixed configurations may be traced joining straight lines and circular arcs of curvature smaller or equal to the maximum allowed. Dubins results have been extended to the case of a vehicle moving both back and forward by Reeds and Shepp [84]and more recently the issue of computing the shortest path for a nonholonomic vehicle either in an obstacle free workspace or in presence of obstacles has been discussed and refined, among the others, by J.D.Boissonnat et al.[85], X.N.Bui et al.[86], Desaulniers et al.[87], Reister et al.[88], A.M.Shkel et al.[89], Bicchi et al.[90], Moutarlier et al.[91], Desaulniers et al.[92] and Szczerba et al.[93]. Kanayama et al.[94] suggest the use of paths generated joining cubic spirals and arc of circles to minimize two cost functions related to curvature and jerk energies while A.M.Hussein et al.[95] generate smooth paths optimizing the integral of the square acceleration instead of curvature. One of the cost functions used by Kanayama et al.[94], and that is at the center of the present paper, is the integral over the path's lengths of its square curvature. A similar optimal criterion has been taken into account also by Reuter [96] within an optimal control approach. Indeed the minimization of $\int k^2 ds$ with fixed boundary configurations is a problem with an interest of its own as such cost function can be physically interpreted as proportional to the elastic energy of the curve. Due to this fact the sought plane path is sometimes called the *least energy curve* in literature. Indeed this interpretation makes the problem appealing also to researchers of other fields as A.M.Bruckstein et al.[97], B.K.P.Horn [98] and M.Kallay [99] who addressed a very similar problem to the one here discussed within a different framework and formulation. It will be shown that Horn's [98] and Kallay's [99] $2D$ results can be viewed as the projection on a plane of a more general $3D$ Euler-Poisson equation.

5.2.1 Curvature

Consider a generic differentiable curve $\mathbf{C}$ parametrized by the coordinate ξ, so that in Cartesian coordinates the points of $\mathbf{C}$ are $x = C_1(\xi)$, $y = C_2(\xi)$, $z = C_3(\xi)$. The paths curvilinear coordinate s is defined as

$$s = \int_0^{\xi} \left| \frac{d\mathbf{C}(\zeta)}{d\zeta} \right| \, d\zeta \tag{5.24}$$

being

$$\begin{aligned} \frac{d}{d\zeta}\mathbf{C} &\triangleq \mathbf{e}_1 \frac{dC_1}{d\zeta} + \mathbf{e}_2 \frac{dC_2}{d\zeta} + \mathbf{e}_3 \frac{dC_3}{d\zeta} \\ (\mathbf{e}_1, \mathbf{e}_2, \mathbf{e}_3) &: \text{reference unit vectors} \end{aligned}$$

and the unit tangent vector $\mathbf{T}$ is defined as

$$\mathbf{T} \triangleq \frac{d\mathbf{C}}{d\zeta} \Bigg/ \left| \frac{d\mathbf{C}}{d\zeta} \right| \tag{5.25}$$

Differentiating equation (5.24) it follows that

$$\frac{ds}{d\zeta} = \left| \frac{d\mathbf{C}}{d\zeta} \right| \tag{5.26}$$

so that the unit tangent $\mathbf{T}$ can be computed as

$$\mathbf{T} = \frac{d\mathbf{C}}{ds} \tag{5.27}$$

By definition the curvature is a vector given by

$$\mathbf{k} \triangleq \frac{d\mathbf{T}}{ds} \tag{5.28}$$

so that in the $2D$ case

$$\mathbf{k} \triangleq \frac{d\mathbf{T}}{ds} \Rightarrow k = \left| \frac{d\theta}{ds} \right|$$

being $d\theta$ the angular deviation relative to a step ds along the path. In many $2D$ applications the *signed curvature*

$$k = \frac{d\theta}{ds} \tag{5.29}$$

is adopted. Notice that having $\mathbf{T}$ unit constant norm, by definition, $\mathbf{k}$ and $\mathbf{T}$ are normal, i.e. $\mathbf{k} \cdot \mathbf{T} = 0$. To compute the curvature k of a generic curve $\mathbf{C} = (C_1(\xi), C_2(\xi), C_3(\xi))$

the following formula is most useful

$$k^2 = \frac{\left| \frac{d\mathbf{C}}{d\xi} \wedge \frac{d^2\mathbf{C}}{d^2\xi} \right|^2}{\left| \frac{d\mathbf{C}}{d\xi} \right|^6} \tag{5.30}$$

Equation (5.30) can be proved by direct calculation as follows: denoting with the symbol $'$ the derivative with respect to ξ and with m the norm of $d\mathbf{C}/d\xi$, i.e.

$$m \triangleq |\mathbf{C}'| = \left| \frac{d\mathbf{C}}{d\xi} \right|$$

equations (5.25), (5.26) and (5.28) imply

$$\mathbf{C}' = m\mathbf{T} \tag{5.31}$$
$$\mathbf{C}'' = m'\mathbf{T} + m^2\mathbf{k} \tag{5.32}$$

Next with reference to the vector property given by equation (2.3) and to the above equations for $\mathbf{C}'$ and $\mathbf{C}''$, consider

$$\begin{aligned}
\left| \frac{d\mathbf{C}}{d\xi} \wedge \frac{d^2\mathbf{C}}{d^2\xi} \right|^2 &= (\mathbf{C}' \wedge \mathbf{C}'') \cdot (\mathbf{C}' \wedge \mathbf{C}'') = ((\mathbf{C}' \wedge \mathbf{C}'') \wedge \mathbf{C}') \cdot \mathbf{C}'' = \\
&= -\mathbf{C}'' \cdot (\mathbf{C}' \wedge (\mathbf{C}' \wedge \mathbf{C}'')) = -\mathbf{C}'' \cdot (\mathbf{C}'(\mathbf{C}' \cdot \mathbf{C}'') - \mathbf{C}''(\mathbf{C}' \cdot \mathbf{C}')) = \\
&= (\mathbf{C}'' \cdot \mathbf{C}'')(\mathbf{C}' \cdot \mathbf{C}') - (\mathbf{C}' \cdot \mathbf{C}'')^2 = (m'^2 + m^4k^2)m^2 - m^2m'^2 = \\
&= m^6k^2
\end{aligned}$$

which concludes the proof. In terms of the Cartesian coordinates $(x(\xi), y(\xi), z(\xi))$ equation (5.30) yields

$$k^2 = \frac{(y'z'' - z'y'')^2 + (x'z'' - z'x'')^2 + (x'y'' - y'x'')^2}{(x'^2 + y'^2 + z'^2)^3} \tag{5.33}$$

Moreover from equation (5.32) it follows that

$$m' = \mathbf{C}'' \cdot \mathbf{T} \Rightarrow m^2\mathbf{k} = \mathbf{C}''(\mathbf{T} \cdot \mathbf{T}) - \mathbf{T}(\mathbf{C}'' \cdot \mathbf{T}) \Rightarrow$$

$$m^2\mathbf{k} = \mathbf{T} \wedge (\mathbf{C}'' \wedge \mathbf{T}) \Rightarrow \mathbf{k} = \frac{\mathbf{C}' \wedge (\mathbf{C}'' \wedge \mathbf{C}')}{|\mathbf{C}'|^4}$$

showing the relation between curvature vector and second derivative of a curve.

5.2.2 Planning criterion: a variational calculus approach

The above discussion regarding the energy that a rigid body dissipates during a $2D$

motion in a fluid suggested the minimization of the integral of the square curvature of the path over length with fixed boundary configurations, i.e.

$$J_I = \int_0^L k^2 ds \tag{5.34}$$

$$\text{in } 2D \quad \begin{cases} (x(0), y(0), \theta(0)) = (x_0, y_0, \theta_0) \\ (x(L), y(L), \theta(L)) = (x_L, y_L, \theta_L) \\ \left.\frac{y'}{x'}\right|_0 = \tan\theta_0 \; ; \; \left.\frac{y'}{x'}\right|_L = \tan\theta_L \end{cases} \tag{5.35}$$

$$\text{in } 3D \quad \begin{cases} (x(0), y(0), z(0), p(0), q(0), r(0)) = (x_0, y_0, z_0, p_0, q_0, r_0) \\ (x(L), y(L), z(L), p(L), q(L), r(L)) = (x_L, y_L, z_L, p_L, q_L, r_L) \\ p, q, r : \text{Euler angles} \end{cases} \tag{5.36}$$

Where in the $2D$ case θ_0 and θ_f are the initial and final angles between the curve and the x-axis. A most natural setting to solve the minimization of J_I with the given boundary conditions is classical analytical variational calculus which is preferred to a numerical optimal control solution as through variational calculus the general Euler-Poisson differential equation that the solution must satisfy can be computed. Notice that in equations (5.34), (5.35) and (5.36) L is not fixed and if $L \to \infty$ it is always possible to find a path for which $J_I \to 0$ as can be understood from figure (5.14). The cost on line segments is null and its value on the arc of circle $\widehat{P_1 P_2}$ is $\frac{\Delta\theta}{r}$, so if points P_1 and P_2 tend to infinity also r will and J_I will tend to zero. The junctions between straight lines and the arc of the circle where curvature is not defined can be made smooth with a Cornu spiral [100] which will not affect the cost when P_1 and P_2 tend to infinity. Solutions of infinite length as the one shown in figure (5.14) can not be found by variational calculus as they belong to the closure of the open set of curves in $\Re^2$. It will be demonstrated that if $|\theta(s) - \theta_0| > \pi$ holds for some s, a finite length solution never exists, so either an additional constraint on total length must be added or the cost function must be changed in order to penalize length. Notice that the minimization of J_I given by equation (5.34) as a planning criterion is somehow the dual problem of the most popular Dubins problem that has been extensively analyzed in the literature as discussed above. As a matter of fact the proposed planning criterion consists in finding the "least curvature" path, i.e. $\arg\min J_I$, of bounded length as opposed to the shortest path of bounded curvature, i.e. Dubins criterion. Within the nonholonomic vehicle path planning literature similar approaches have been considered by Kanayama

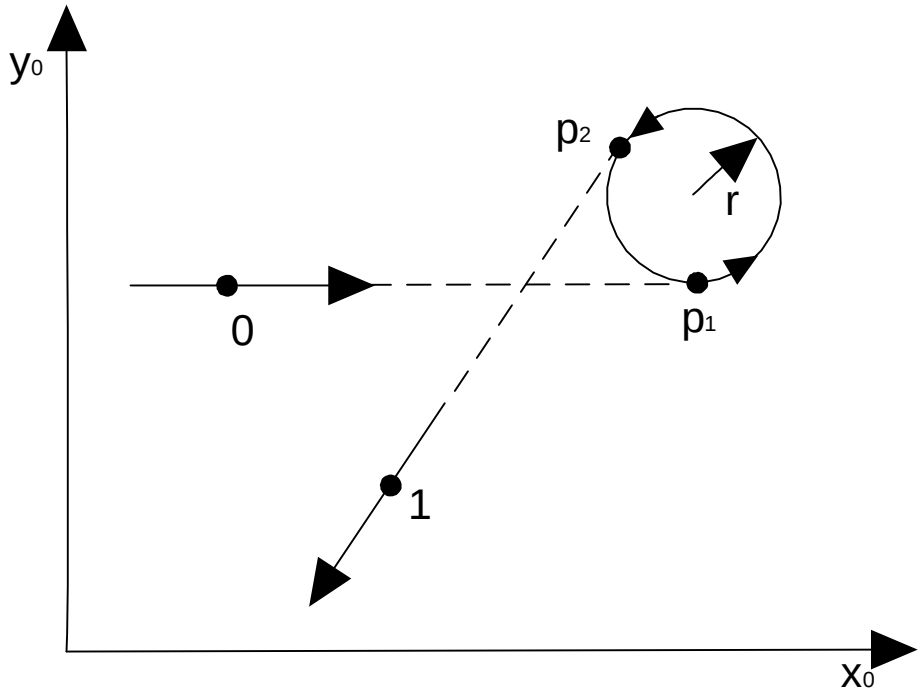

5.14.Infinite lenght solutions: a geometrical interpretation.

et al.[94] and Reuter [96]. In particular Kanayama et al.[94] consider the minimization of J_I given by equation (5.34), but over a given fixed length: having fixed the length it is not possible to satisfy boundary conditions as given in equations (5.35) on both the starting and ending configurations, but at most on one of the two. This is a consequence of the fact that the only solution of the minimization of J_I with fixed length, as stated in [94], is an arc of a circle [101]: with reference to equation (5.29) and indicating with $'$ the derivative with respect to the curvilinear coordinate s, i.e. $k \triangleq \frac{d\theta}{ds} \triangleq \theta'(s)$,

$$\min \int_0^{\bar{L}} \theta'^{\,2} ds : \bar{L} \text{ fixed} \Leftrightarrow \frac{\partial}{\partial \theta}\theta'^{\,2}(s) - \frac{d}{ds}\frac{\partial}{\partial \theta'}\theta'^{\,2}(s) = 0 \Rightarrow$$

$$\theta''(s) = 0 \Rightarrow \theta'(s) = const.$$

In the great majority of the practical situations length is not given a priori, but only the initial and final configurations are. Indeed if the cost J_I is to be interpreted as proportional to the "elastic energy" of the path or to the energy dissipated by rotational drag to join two given configurations, equations (5.35) must be satisfied. The cost function considered by Reuter [96] within an optimal control framework is given by

$$J_R \triangleq \int_0^L \left(\alpha k^2 + \beta \left(\frac{d^2 k}{ds^2}\right)^2\right) ds = \alpha J_I + \beta \int_0^L \left(\frac{d^2 k}{ds^2}\right)^2 ds$$

with non-fixed length. The major advantage of considering such a cost function is that having J_R a dependance on both k and k'', boundary conditions may be imposed on the direction, the curvature and the curvature derivative at the boundary positions, i.e. the minimum of J_R must be computed adding to the boundary conditions given by equation (5.35) the conditions $k(0) = k_0$, $k(L) = k_L$, $k'(0) = k'_0$, $k'(L) = k'_L$. Nevertheless in [96] only the numerical solution of the optimization problem $\arg\min J_R$ is addressed and such solutions solves the problem of interest $\arg\min J_I$ only if $\beta = 0$, thus a variational approach solution to the minimization of J_I for a generic curve parametrization will be presented for both the $3D$ and $2D$ case.

With reference to equation (5.30) and remembering that for the arbitrary parametrization ξ the infinitesimal curve length element ds can be written as $ds = (x'^{\,2} + y'^{\,2} + z'^{\,2})^{1/2}$ being $'$ the derivative operator with respect to ξ, the cost function J_I is

$$\begin{aligned} J_I &= \int_0^{\xi_f} \frac{(y'z'' - y''z')^2}{(x'^{\,2} + y'^{\,2} + z'^{\,2})^{5/2}} d\xi + \int_0^{\xi_f} \frac{(z'x'' - z''x')^2}{(x'^{\,2} + y'^{\,2} + z'^{\,2})^{5/2}} d\xi \\ &\quad + \int_0^{\xi_f} \frac{(y''x' - x''y')^2}{(x'^{\,2} + y'^{\,2} + z'^{\,2})^{5/2}} d\xi \end{aligned} \tag{5.37}$$

The $2D$ case, which must be optimized with boundary conditions given in (5.35), is obtained for $z = constant \rightarrow z' = z'' = 0$. Indicating respectively with G_1, G_2 and G_3 the three integrands of equation (5.37) the following hold $J_I = \sum_{i=1}^{3} \int_0^{\xi_f} G_i \, d\xi$ and

$$\sum_{i=1}^{3} G_i = k^2 \frac{ds}{d\xi} \tag{5.38}$$

As each G_i is positive by definition, equation (5.37) will be minimized if and only if each term of (5.37) will be; thus the minimization conditions for a generic term G_i must be sought. Lets consider for example G_3 and the minimization of $\nu = \int_0^{\xi_f} G_3 \, d\xi$. Assuming

$$F \triangleq G_3 = \frac{(y''x' - x''y')^2}{(x'^2 + y'^2 + z'^2)^{5/2}} \tag{5.39}$$

and indicating with F_λ its partial derivative with respect to any quantity λ the solution $(x(\xi), y(\xi), z(\xi))$ to the minimization of $\nu = \int_0^{\xi_f} F \, d\xi$ has to satisfy Euler-Poisson's equations [101]:

$$\left.\begin{aligned} F_x - \frac{d}{d\xi} F_{x'} + \frac{d^2}{d\xi^2} F_{x''} = 0 \\ F_y - \frac{d}{d\xi} F_{y'} + \frac{d^2}{d\xi^2} F_{y''} = 0 \\ F_z - \frac{d}{d\xi} F_{z'} = 0 \end{aligned}\right\} \tag{5.40}$$

If the total length had been fixed to L^* the optimal curve would have to satisfy (5.40) with fixed boundary configurations as given by equations (5.35) in $2D$ or equations (5.36) in $3D$, and ξ_f such that $\int_0^{\xi_f} (x'^2 + y'^2 + z'^2)^{1/2} d\xi = L^*$; if, on the contrary, the total length is not fixed equation (5.40) must hold with fixed boundary configurations given by equations (5.35) or (5.36) and with the constraint of null variation $\Delta\nu$ due to the moving boundary ξ_f. The expression of the variation $\Delta\nu$ due to the moving boundary ξ_f can be calculated extending the same techniques [101] adopted when F depends on a single function and it's first derivative, i.e. $F = F(x, y(x), y'(x))$, to the present situation where $F = F(\xi, x, y, z, x', y', z', x'', y'', z'')$. Assuming equation

(5.40) to be satisfied the variation due to moving boundary is

$$\begin{aligned}\Delta\nu = &\Big[F - y''F_{y''} - y'\left(F_{y'} - \tfrac{d}{d\xi}F_{y''}\right) + \\ &-x''F_{x''} - x'\left(F_{x'} - \tfrac{d}{d\xi}F_{x''}\right) - z'F_{z'}\Big]\Big|_{\xi_f}\delta\xi_f + \\ &+F_{y''}|_{\xi_f}\,\delta y'_f + F_{x''}|_{\xi_f}\,\delta x'_f + \left(F_{y'} - \tfrac{d}{d\xi}F_{y''}\right)\Big|_{\xi_f}\delta y_f \\ &+\left(F_{x'} - \tfrac{d}{d\xi}F_{x''}\right)\Big|_{\xi_f}\delta x_f + F_{z'}|_{\xi_f}\,\delta z_f\end{aligned} \tag{5.41}$$

For fixed boundary configurations, as required by (5.35) in $2D$, $\delta x_f = \delta y_f = \delta z_f = \delta x'_f = \delta y'_f = \delta z'_f = 0$ and $\delta\xi_f \neq 0$ as the final configuration is assigned, but length is not. Thus to guarantee null $\Delta\nu$ the term in square brackets of equation (5.41) must be null. With reference to equations (5.40) and (5.39) notice that $F_x = F_y = F_z = 0$ and $F_\xi = 0$ by definition of F so that the following first integrals must hold:

$$\left.\begin{aligned} F_{x'} - \frac{d}{d\xi}F_{x''} &= -\alpha_1 \\ F_{y'} - \frac{d}{d\xi}F_{y''} &= -\alpha_2 \\ F_{z'} &= -\alpha_3 \end{aligned}\right\} \tag{5.42}$$

for some constant α_1, α_2 and α_3. Moreover, by direct calculation follows that

$$F - y''F_{y''} - x''F_{x''} = -F$$

and that

$$\begin{aligned} -\frac{d}{d\xi}F &= \frac{d}{d\xi}(F - y''F_{y''} - x''F_{x''}) = \\ &= x''[F_{x'} - \frac{d}{d\xi}F_{x''}] + y''[F_{y'} - \frac{d}{d\xi}F_{y''}] + z''F_{z'} \end{aligned}$$

Substituting equation (5.42) in this last equation and integrating implies

$$F = \frac{(y''x' - y'x'')^2}{(x'^{\,2} + y'^{\,2} + z'^{\,2})^{5/2}} = \alpha_1\, x' + \alpha_2\, y' + \alpha_3\, z' + \beta \tag{5.43}$$

This differential equation must be solved with boundary configurations given by equations (5.36) and either $\int_0^{\zeta_f}(x'^{\,2} + y'^{\,2} + z'^{\,2})^{1/2}d\zeta = L^*$ if L^* is fixed, or $\Delta\nu = 0$ being $\Delta\nu$ defined in (5.41) if maximum length is not fixed. This latter hypothesis implies $\beta = 0$ as can be shown substituting (5.42) in (5.41). Moreover equation (5.43) that has been derived for $F \equiv G_3$ can be shown to hold, with different constants α_i $i = 1, 2, 3$

and β, also for G_1 and G_2. As a consequence substituting these equations in (5.38) the general $3D$ Euler-Poisson equation solving the optimization problem (5.34) for an arbitrary parameterization ξ is found to be:

$$k^2 \frac{ds}{d\xi} = \mathbf{a} \cdot \frac{d\mathbf{C}(\xi)}{d\xi} + b \tag{5.44}$$

where $\mathbf{a}$ and b are constants that depend on the given boundary conditions. As follows from the above discussion, b is either null if no length constraint is imposed, or eventually non null in order to satisfy a given length L^*. As torsion is not specified, equation (5.44) by itself, projected on a plane and with given boundary configurations, uniquely determines a $2D$ curve, but not a $3D$ one. In the $2D$ situation $z = constant$ with a curvilinear parameterization $\xi = s$ equation (5.44) is reduced to the same equations calculated in the plane starting from a Cartesian parameterization [98] [99], i.e.,

$$k^2(s) = \mathbf{a} \cdot \mathbf{T}(s) + \beta = \alpha \cos(\theta - \varphi) + \beta \tag{5.45}$$

being the vector $\mathbf{a} = (\alpha_1, \alpha_2)$, α it's norm and φ it's phase. Equation (5.45) had been already presented by Horn [98] in 1983 and then discussed by Kallay [99] and Bruckstein et al.[97] in 1986 and 1990 within the computer graphics research community. Nevertheless in these previous works the variational problem was solved for a one valued real function $y : \Re \rightarrow \Re$ and the so computed Euler equation was then "extended" to the case of a $2D$ curvilinear parametrized curve $(x(s), y(s))$. Indeed the $2D$ result is the same, but a priori this fact is not obvious as the set of real valued functions $y(x)$ among which the solution was initially computed is a subset of the larger set of $2D$ curves $(x(\xi), y(\xi))$. Moreover having approached and solved the minimization problem directly in the family of $3D$ curves, the most general $3D$ solution given by equation (5.44) has been obtained [102] and a much deeper insight in the interpretation of the β parameter has been presented.

5.2.3 Solution properties

With reference to equation (5.45) the following properties hold:

i) If no constraint is imposed on maximum length (i.e. $\beta = 0$, see (5.41)) and $|\theta(s) - \theta_0| > \pi$ for some s equation (5.45) has no solution other than $\alpha = 0$, i.e. a straight line of infinite length, a solution of the kind depicted in figure (5.14). Moreover when a finite non-constrained length solution exists ($\beta = 0$, but $\cos(\theta - \varphi) > 0$ on the whole path) it is never a finite radius circular arc (constant non null curvature) as equation (5.45) shows that constant curvature would imply a constant unit tangent vector $\mathbf{T}(s)$, i.e. a straight line once again.

ii) To completely determine the path from equation (5.45) the constants α_1, α_2 and, eventually, β must be calculated on the basis of boundary conditions (5.35). As suggested by M.Kallay [99], if the paths curvature is strictly different from zero over the

whole length, this may be accomplished solving numerically the following nonlinear system

$$\left.\begin{aligned} x_f &= \int_{\theta_0}^{\theta_f} \frac{\cos(\theta)}{k(\theta)}\, d\theta \\ y_f &= \int_{\theta_0}^{\theta_f} \frac{\sin(\theta)}{k(\theta)}\, d\theta \\ L^* &= \int_{\theta_0}^{\theta_f} \frac{1}{k(\theta)}\, d\theta \end{aligned}\right\} \tag{5.46}$$

being k given by equation (5.45). If, on the contrary, the paths curvature is null for some s as when k changes sign, equations (5.46) are not defined and a different approach must be adopted. The issue of computing the path for given boundary configurations integrating equation (5.44) will be discussed in the following section for both constant and non constant sign curvature paths. The initial configuration can always be thought as $(x_0 = 0, y_0 = 0, \theta_0 = 0)$ as this is equivalent to choosing the reference frame. The last equation of (5.46) is needed to calculate β if the final length is assigned. Notice once again that if $|\theta(s) - \theta_0| \leq \pi \; \forall \; s$ belonging to the path then the length needs not to be penalized ($\beta = 0$) and the curvature can be computed for every point of the path as $k = \pm\sqrt{\mathbf{a} \cdot \mathbf{T}}$ being the sign fixed according to the curve direction. Following the previous observation the β parameter needs to be fixed to a non null positive value only if the range of the values of $\theta(s)$ along the path is such that $\mathbf{a} \cdot \mathbf{T}$ can not stay positive for every s. Nevertheless from an engineering point of view fixing the total length is as unreasonable as dealing with infinitely long paths. The most natural approach is to weight curvature and length through some parameter. Indeed within the developed formulation (equations 5.40 through 5.42) it can be shown that if the cost function to be minimized is changed from equation (5.34) with *fixed* L to $\int_0^L (k^2 + \mu)\, ds$ with *non fixed* L, being μ a positive constant that penalizes length, the Euler-Poisson equation to be solved has exactly equation's (5.45) structure with the fixed μ parameter in place of the unknown β, i.e. $k^2(s) = \mathbf{a} \cdot \mathbf{T}(s) + \mu$. This is not surprising as μ (or β) can be thought of as a Lagrange multiplier that transforms the L-constrained minimization of (5.34) problem, in the equivalent L-unconstrained minimization of $\int_0^L (k^2 + \mu)\, ds$ problem. Given this different and more appealing interpretation of the freely fixed β it will be sufficient to solve the first two equations of (5.46) in order to calculate $\mathbf{a}$ and thus the optimal path.

iii) If boundary conditions (5.35) are such that $\theta(s) \simeq 0$ over the whole length of the path than the tangent vector $\mathbf{T}(s)$ can be approximated by $\mathbf{T}(s) \cong (1, \theta(s))$ so that equation (5.45) implies

$$\frac{d\theta}{ds} = \alpha_2\, \theta(s) + \beta + \alpha_1$$

being $\frac{d\theta}{ds} = k$ by definition of curvature. Integrating this equation with initial condition

$\theta(0) = 0$ yields $\theta(s) = \frac{\alpha_2}{4}s^2 \pm s\sqrt{\beta + \alpha_1}$ or

$$k(s) = \frac{\alpha_2}{2}s \pm \sqrt{\beta + \alpha_1} \tag{5.47}$$

i.e., the curve is a clothoid or Cornu spiral. Cornu spirals are curves defined by $k(s) = k_c s + k_0$ and are used mostly in highway and railway design to link smoothly (up two second derivative) two curves possibly of different curvature [100] as two circles of different radius, straight lines and circles, two different straight lines, or similar. Special-case clothoids are circles ($k_c = 0, k_0 \neq 0$) and straight lines ($k_c = k_0 = 0$). In robotic applications they have been first analyzed by Kanayama et al.[103] and used for smoothing trajectories by Fleury et al.[104], but apparently had never shown to be minimal energy when $\theta(s) \simeq 0$. The major limit in their use is due to the difficulty in calculating k_c and k_0 for given boundary configurations. Nevertheless in the hypothesis $\theta(s) \simeq 0$ (the only case of interest) clothoids can be approximated by a cubic polynomial with the same degree of approximation used in $\mathbf{T}(s) \cong (1, \theta(s))$. From equation (5.43) when $z' \equiv z'' \equiv 0$ ($2D$) and $\xi \rightarrow x$ (Cartesian parameterization) and approximating $(1 + y'^2(x)) \sim 1 \; \forall \; x$ (which is equivalent to $\mathbf{T}(s) \cong (1, \theta(s)) \; \forall \; s$) follows that $y''^2(x) = \alpha_2 \, y'(x) + \alpha_1 + \beta \Longrightarrow y(x) = \sum_{n=0}^{3} a_n x^n$ i.e. a cubic polynomial satisfying the two boundary configurations.

5.2.4 Solution examples

The major difficulty in the implementation of the above reported $2D$ results is related to the calculation of the parameter $\mathbf{a}$ given the final boundary configuration (as noticed previously the initial configuration can always be taken to be $(0, 0, 0)$ as this is equivalent to choosing the reference frame). Equation (5.44) can not be trivially integrated, thus a numerical algorithm is required. Two different cases may be distinguished:

- constant sign, non null curvature paths
- non constant sign curvature paths called *S-shaped* paths in the following

As far as the first case is concerned the parameters $\alpha > 0$ and φ of equation (5.45) can be computed as

$$\arg\min_{\alpha,\varphi} \left[\left(x_f - \int_0^{\theta_f} \frac{\cos\theta}{\pm\sqrt{\alpha\cos(\theta - \varphi) + \beta}} d\theta \right)^2 \right. \tag{5.48}$$
$$\left. + \left(y_f - \int_0^{\theta_f} \frac{\sin\theta}{\pm\sqrt{\alpha\cos(\theta - \varphi) + \beta}} d\theta \right)^2 \right]$$

being (x_f, y_f, θ_f) the given final boundary configuration and $\beta \geq 0$ a constant that needs to be non null only if for the given (x_f, y_f, θ_f) no solution exists for $\beta = 0$, as when $|\theta_f| > \pi$. The sign in front of the square roots is unambiguously fixed according

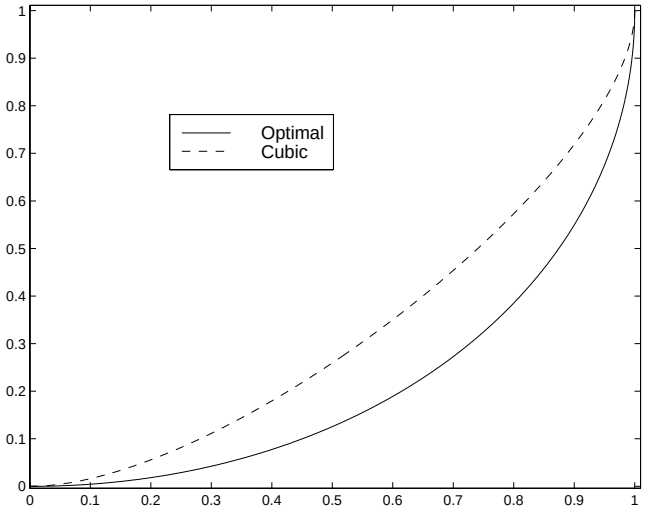

5.15.Optimal 90^o curve, obtained assuming $(1, 1, \pi/2)$ as final configuration and $\beta = 0$, and cubic spline 90^o curve.

to the desired curve direction. The minimum problem given by equation (5.48) can be solved by standard numerical methods as the simplex method. Examples of the paths obtained with this approach are displayed in figures (5.15) and (5.17). The $\mathbf{a}$ parameter of S-shaped paths can not be computed with the above suggest method as by definition of S-shaped path the curvature takes a null value for some value θ^* of θ. As shown by the example reported in figure (5.18), where $\beta = 0$ for the sake of simplicity, once that the curvature reaches a null value as θ evolves k has to change sign as not so doing would imply a discontinuity in the derivative of k with respect to θ. Indeed once that the curvatures sign is fixed at the starting configuration $(0, 0, 0)$, the apparent possible ambiguity in ks sign choice is completely solved by the above observation: if a θ^* such that $k(\theta^*) = 0$ is reached the curvature changes sign. In order to compute $\mathbf{a}$ for a given final configuration and with reference to equations (5.6) consider the kinematics of an ideal point following the S-shaped path with unit velocity

$$\dot{x} = \cos\theta \tag{5.49}$$

$$\dot{y} = \sin\theta \tag{5.50}$$

$$\dot{\theta} = k = \pm\sqrt{a_1\cos\theta + a_2\sin\theta} \tag{5.51}$$

A possible algorithm to compute $\mathbf{a} = (a_1, a_2)$ is

$$\mathbf{a} = \arg\min_{a_1,a_2} J_S$$

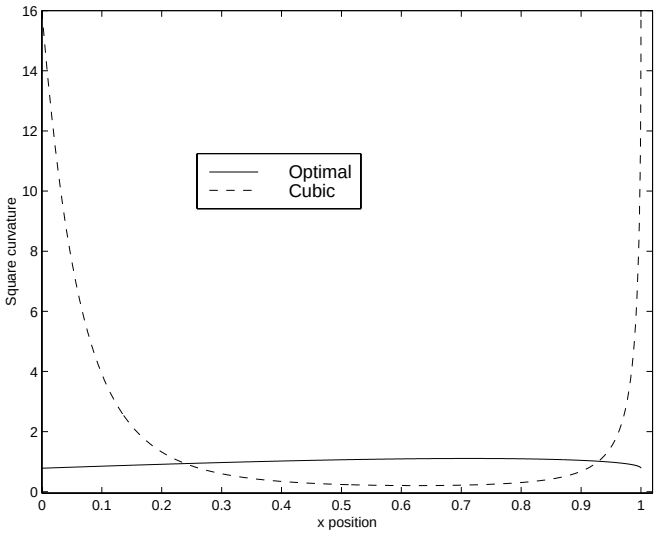

5.16.Square curvature for an optimal 90^o curve and a cubic spline path versus the x position.

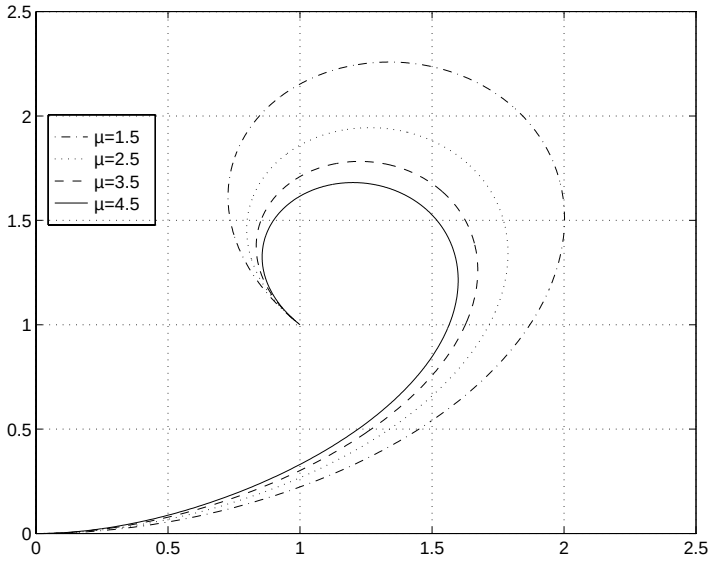

5.17.Paths of constant curvature sign for final configuration $(1, 1, 7\pi/4)$ and varius values of μ, i.e. β.

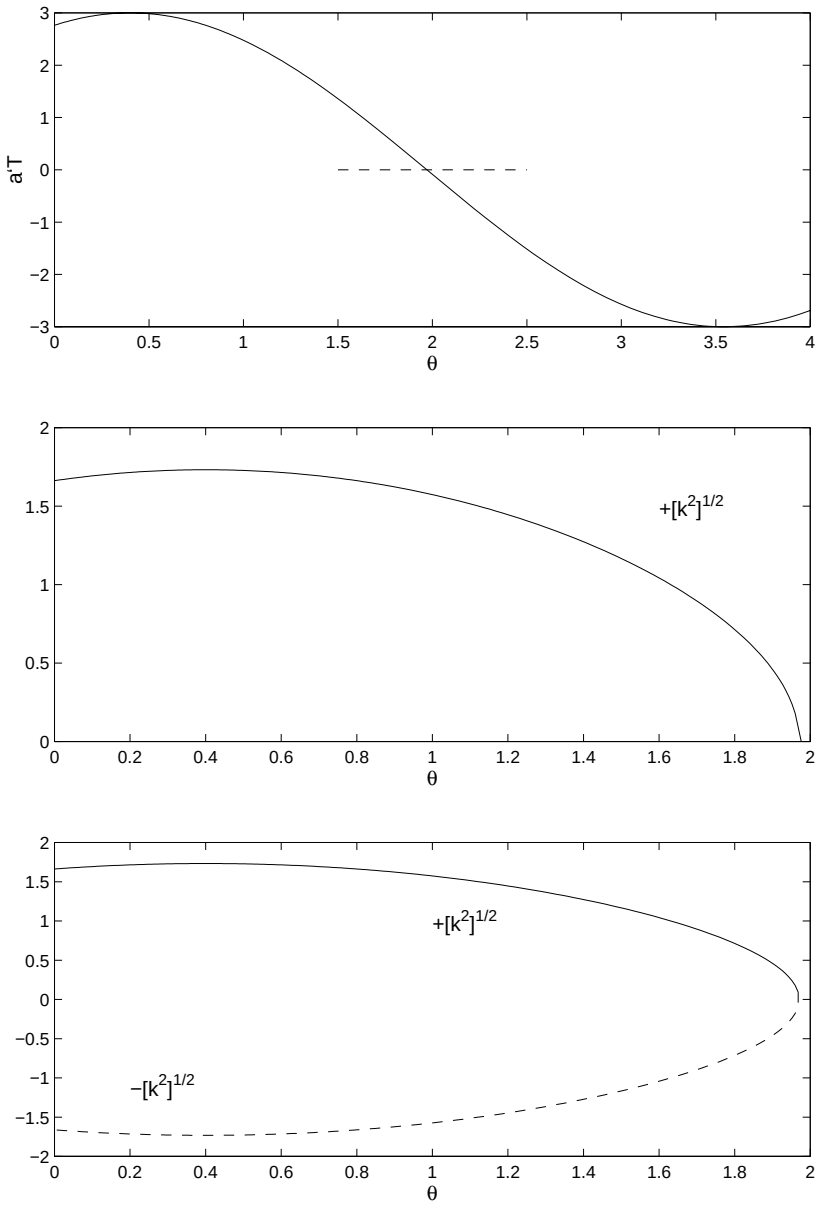

5.18.From top to bottom: $k^2 = \mathbf{a} \cdot \mathbf{T}$ and k as functions of θ in the hypothesis that k is always positive or that it changes sign at θ^* being θ^*such that $k(\theta^*) = 0$.

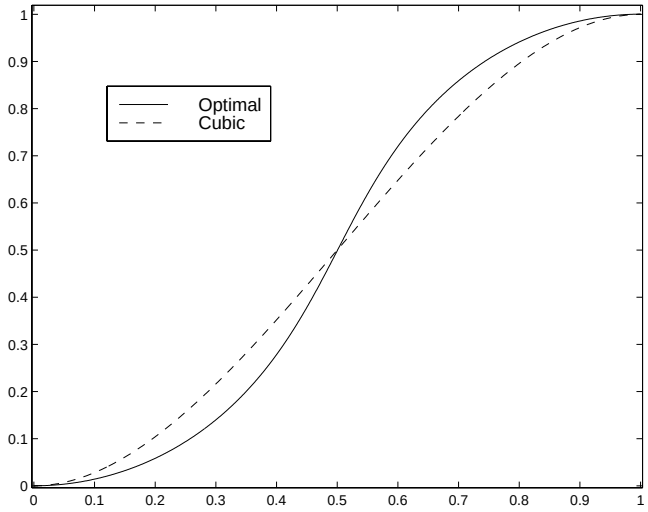

5.19.Optimal and cubic spline paths to the configuration $(1, 1, 0)$, $\beta = 0$.

being J_S computed according to

- **STEP** *(i)* : initialize ks sign at the starting configuration $(0, 0, 0)$
- **STEP** *(ii)* : integrate (Euler integration has been employed in the worked examples) equation (5.51) with the sign fixed at step *(i)* from $\theta = 0$ to $\theta = \theta^*$, being θ^* such that $a_1 \cos\theta^* + a_2 \sin\theta^* = 0$, and from θ^* to θ_f with the opposite sign.
- **STEP** *(iii)* : having computed $\theta(t)$ at step *(ii)* such that $\theta(0) = 0$ and $\theta(t_f) = \theta_f$ integrate equations (5.49) and (5.50) to yield $\bar{x}(\mathbf{a}, \theta_f) = \int_0^{t_f} \cos\theta(t)dt$ and $\bar{y}(\mathbf{a}, \theta_f) = \int_0^{t_f} \sin\theta(t)dt$
- **STEP** *(iii)* : $J_S = (x_f - \bar{x}(\mathbf{a}, \theta_f))^2 + (y_f - \bar{y}(\mathbf{a}, \theta_f))^2$.

Examples of paths computed according to this algorithm are given in figures (5.19) and (5.21). In the reported examples the minimization of J_S has been performed by the simplex method provided by the Matlab software. Notice that in all the presented examples the square curvature of the optimal paths is dramatically lower then the cubic spline square curvature over the whole path. Cubic splines have been used to compare the optimal solution behaviour as they are the least order polynomials satisfying the given boundary configurations. Although these numerical solution methods are straight forward they are not suitable for on line path planning algorithms thus future work will investigate alternative approaches to the calculation of the constants in equation (5.44).

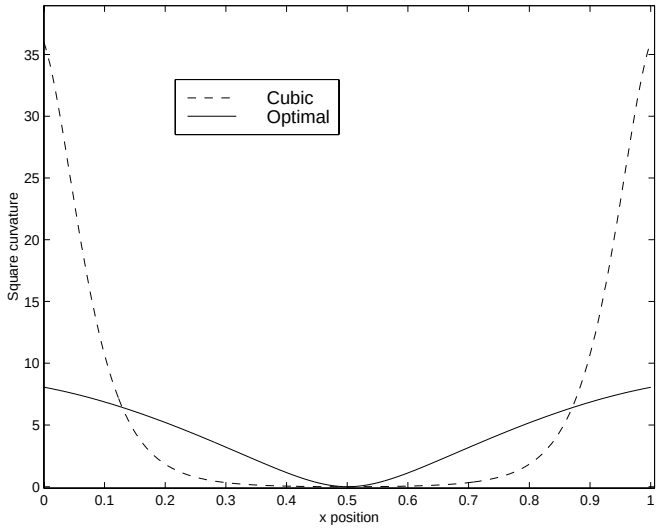

5.20.Square curvature versus the x position of the cubic spline and optimal paths having $(1, 1, 0)$ as final configuration; $\beta = 0$.

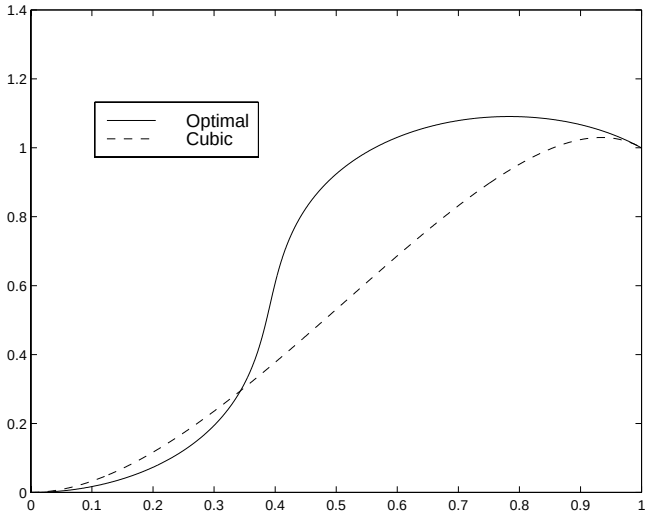

5.21.Cubic spline and optimal paths for the $(1, 1, -\pi/4)$ final configuration with $\beta = 0$.

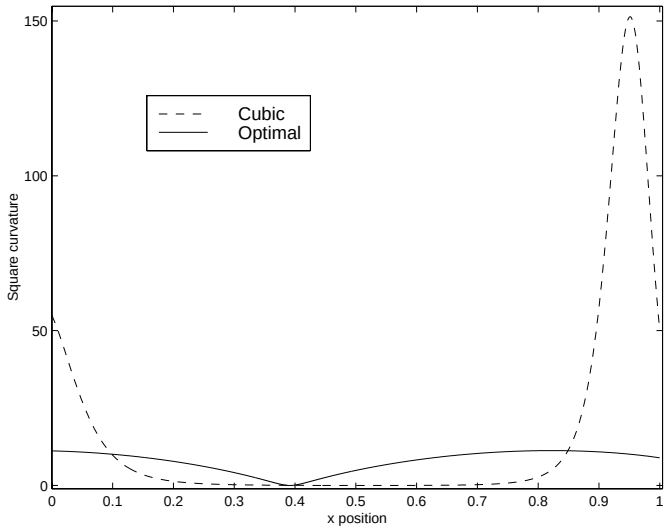

5.22.Square curvature versus x position for the cubic spline and optimal paths relative to the final configuration $(1, 1, -\pi/4)$.

References

[1] G. Casalino, M. Aicardi, A. Bicchi, and A. Balestrino. Closed-loop steering for unicycle-like vehicles: A simple lyapunov like approach. In *IFAC Symposium on Robot Control, Sy.Ro.Co'94*, pages 291–298, Capri, Italy, September 1994.

[2] M. Aicardi, G. Casalino, A. Bicchi, and A. Balestrino. Closed loop steering of unicycle-like vehicles via lyapunov techniques. *IEEE Robotics and Automation Magazine*, pages 27–35, March 1995.

[3] D. Fryxell, P. Oliveira, A. Pascoal, C. Silvestre, and I. Kaminer. Navigation, guidance and control of AUVs: An application to the marius vehicle. *Control Engineering Pratice*, 4(3):401–409, 1996.

[4] D. R. Yoerger and J.-J. E. Slotine. Robust trajectory control of underwater vehicles. *IEEE Jou. Oceanic Eng.*, 10(4):462–470, 1985.

[5] R. Cristi, F. A. Papoulias, and A. Healey. Adaptive sliding mode control of autonomous underwater vehicles in the dive plane. *IEEE Jou. Oceanic Eng.*, 15(3):152–160, 1990.

[6] A. J. Healey and D. Lienard. Multivariable sliding mode control for autonomous diving and steering of unmanned underwater vehicles. *IEEE Jou. Oceanic Eng.*, 18(3):327–339, 1993.

[7] J. P. Cunha, R. R. Costa, and L. Hsu. Design of a high performance variable structure position control of ROV's. *IEEE Jou. Oceanic Eng.*, 20(1):42–55, 1995.

[8] M. L. Corradini and G. Orlando. A discrete time adaptive variable-structure controller for MIMO systems, and its application to an underwater ROV. *IEEE Trans. on Control Systems Technology*, 5(3):349–359, 1997.

[9] G. Bartolini, E. Punta, and E. Usai. Tracking control of underwater vehicles including thruster dynamics by second order sliding modes. In *IEEE Oceans'98*, pages 1645–1649, Nice, France, September 1998.

[10] T. I. Fossen and S. I. Sagatun. Adaptive control of nonlinear underwater robotic systems. In *IEEE Int. Conf. on Robotics and Automation, ICRA'91*, Sacramento, CA, USA, April 1991.

[11] T. I. Fossen and O. Fjellstad. Robust adaptive control of underwater vehicles: A comparative study. In *3rd IFAC Workshop on Control Applications in Marine Systems, CAMS'95*, pages 66–74, Trondheim, Norway, May 1995.

[12] A. K. Ramadorai and T. J. Tarn. On modeling and adaptive control of underwater robots. In *4th International Advanced Robotics Program, IARP'92*, Genoa, Italy, November 1992.

[13] S. I. Sagatun and R. Johansson. Optimal and adaptive control of underwater vehicles. In *4th IFAC Symposium on Robot Control, Sy.Ro.Co.'94*, Capri, Italy, 1994.

[14] J.Yuh. Modeling and control of underwater robotic vehicles. *IEEE Transactions on Systems, Man, and Cybernetics*, 20(6):1475–1483, 1990.

[15] G. Conte and A. Serrani. Disturbance attenuation via lyapunov techniques for autonomous underwater vehicles. In *International Advanced Robotics Program, IARP'98*, Lafayette, Lousiana, USA, February 1998.

[16] G. Conte and A. Serrani. Global robust tracking with disturbance attenuation for unmanned underwater vehilces. In *IEEE Int. Conf. on Control Applications, CCA'98*, pages 1094–1098, Trieste, Italy, September 1998.
[17] G. Conte and A. Serrani. Robust control of a remotely operated underwater vehicle. *Automatica*, 34(2):193–198, 1998.
[18] J. Yuh. A neural controller for underwater robotic vehicles. *IEEE Jou. Oceanic Eng.*, 15(3):161–166, 1990.
[19] J.Yuh. Learning control for underwater robotic vehicles. *IEEE Control Systems*, pages 39–46, April 1994.
[20] P. J. Craven, R. Sutton, and Y. M. Dai. A neurofuzzy technique applied to UUV autopilot design. In *IFAC Conference on Marine Craft Maneuvering and Control, MCMC'97*, Brijuni, Croatia, September 1997.
[21] H. Mahesh, J. Yuh, and R. Lakshmi. A coordinated control of an underwater vehicle and robotic manipulator. *Journal of Robotic Systems*, 8(3):339–370, 1991.
[22] I. Schjølberg and T. I. Fossen. Modelling and control of underwater vehicle-manipulator systems. In *3rd Conference on Marine Craft Maneuvering and Control, MCMC'94*, pages 45–57, September 1994.
[23] S. McMillan, D.E. Orin, and R.B. McGhee. Efficient dynamic simulation of an underwater vehicle with a robotic manipulator. *IEEE Transactions on Systems, Man, and Cybernetics*, 25(8):1194–2006, 1995.
[24] T. J. Tarn, G. A. Shoults, and S. P. Yang. Dynamical model for an underwater vehicle with multiple robotic manipulators. In *6th International Advanced Robotics Program, IARP'96*, pages 1–23, Toulon, France, March 1996.
[25] T. W. McLain and S. M. Rock. Development and experimental validation of an underwater manipulator hydrodynamic model. *Int. Jou. of Robotics Research*, 17(7):748–759, 1998.
[26] M. W. Dunnigan and G. T. Russel. Evaluation and reduction of the dynamic coupling between a manipulator and an underwater vehicle. *IEEE Jou. Oceanic Eng.*, 23(3):260–273, 1998.
[27] C. Canudas de Wit and Diaz. Robust nonlinear control of an underwater vehicle/manipulator system with composite dynamics. In *IEEE Int. Conf. on Robotics and Automation, ICRA'98*, pages 452–456, Leuven, Belgium, May 1998.
[28] M. Caccia, A. Carta Colombo, G. Casalino, M. Decia, and G. Veruggio. Closed-loop approach algorithm based on lyapunov techniques for an autonomous underwater vehicle. In *3rd IFAC Workshop on Control Applications in Marine Systems, CAMS'95*, pages 101–106, Trondheim, Norway, May 1995.
[29] M. Caccia, G. Veruggio, G. Casalino, S. Alloisio, C. Grosso, and R. Cristi. Sonar based bottom estimation in UUVs adopting a multi-hypothesis kalman filter. In *Proc. International Conference on Advanced Robotics, ICAR'97*, pages 745–750, Monterey, CA, USA, July 1997.
[30] M. Caccia, G. Casalino, R. Cristi, and G. Veruggio. Acoustic motion estimation and control for an unmanned underwater vehicle in a structured environment. *Control En-*

gineering Practice, 6:661–670, 1998.
[31] R. Smith, A. Stevens, A. Frost, and P. Probert. Developing a sensor-based underwater navigation system. In *6th International Advanced Robotics Program, IARP'96*, Toulon, France, March 1996.
[32] T. I. Fossen. *Guidance and Control of Ocean Vehicles*. John Wiley & Sons, England, 1994.
[33] P. M. Morse and H. Feshbach. *Methods of Theoretical Physics*. Mc Graw-Hill Inc. and Kogakusha Ltd., International Student Edition 1953.
[34] J. N. Newman. *Marine Hydrodynamics*. The MIT Press, Cambridge, Massachusetts, 1977.
[35] L. M. Milne-Thomson. *Theoretical Hydrodynamics*. Dover Publications Inc., New York, New York, Fifth edition 1968.
[36] H. Lamb. *Hydrodynamics*. Cambridge University Press, Cambridge, UK, Sixth edition 1932.
[37] N. E. Kochin, I. A. Kibel, and N. V. Roze. *Theoretical Hydromechanics*. Interscience Publishers, John Wiley & Sons, 1964.
[38] K. R. Goheen. Modeling methods for underwater robotic vehicle dynamics. *Journal of Robotic Systems*, 8(3):295–317, 1991.
[39] G. Conte and A. Serrani. Modelling and simulation of underwater vehicles. In *IEEE Int. Symposium on Computer-aided Control System Design*, pages 62–67, Dearborn, MI, USA, September 1996.
[40] P. V. Pavlou and K. J. Kyriakopoulos. Wave force identification and compensation for an underwater vehicle. In *IFAC Conference on Marine Craft Maneuvering and Control, MCMC'97*, pages 19–24, Brijuni, Croatia, September 1997.
[41] J. S. Riedel and A. Healey. Model based predictive control of AUVs for station keeping in a shallow water wave environment. In *International Advanced Robotics Program, IARP'98*, Lafayette, Lousiana, USA, February 1998.
[42] J. S. Riedel and A. Healey. Shallow water station keeping of AUVs using multi-sensor fusion for wave disturbance prediction and compensation. In *IEEE Oceans'98*, pages 1065–1069, Nice, France, September 1998.
[43] P. Anathakrishhnan and K-Q. Zhang. AUV motion in a wave field. In *IEEE Oceans'98*, pages 1059–1063, Nice, France, September 1998.
[44] D. R. Yoerger, J. G. Cooke, and J.-J. E. Slotine. The influence of thruster dynamics on underwater vehicle behavior and their incorporation into control system design. *IEEE Jou. Oceanic Eng.*, 15(3):167–178, 1990.
[45] C. L. Tsukamoto, W Lee, J. Yuh, S. K. Choi, and J. Lorentz. Comparison study on advanced thruster control of underwater robots. In *IEEE Int. Conf. on Robotics and Automation, ICRA'97*, pages 1845–1850, Albuquerque, New Mexico, USA, April 1997.
[46] A. J. Healey, S. M. Rock, S. Cody, D. Miles, and J. P. Brown. Toward an improved understanding of thruster dynamics for underwater vehicles. *IEEE Jou. Oceanic Eng.*, 20(4):354–361, 1995.
[47] M.W. Spong and M. Vidyasagar. *Robot Dynamics and Control*. John Wiley & Sons,

New York, NY, 1989.
[48] T. J. Tarn, G. A. Shoults, and S. P. Yang. Dynamical model for a free-floating underwater vehicle with an $n-$axis manipulator. In *Joint US/Portugal Workshop: Undersea Robotics and Intelligent Control*, Lisbon, Portugal, March 1995.
[49] B. Lévesque and M. J. Richard. Dynamic analysis of a manipulator in a fluid environment. *Int. J. Robot. Res.*, 13(3):221–231, 1994.
[50] C. P. Sayers, D. R. Yoerger, R. P. Paul, and J. S. Lisiewicz. A manipulator work package for teleoperation from unmanned underwater vehicles - current feasibility and future applications. In *6th International Advanced Robotics Program, IARP'96*, Toulon, France, March 1996.
[51] T. W. McLain, S. M. Rock, and M. J. Lee. Experiments in the coordination of underwater manipulator and vehicle control. In *IEEE Oceans'95*, 1995.
[52] T. W. McLain and S. M. Rock. Experiments in the hydrodynamic modeling of an underwater manipulator. In *Symposium on Autonomous Underwater Vehicle Technology, AUV'96*, pages 463–469, Monterey, CA, USA, June 1996.
[53] T. W. McLain, S. M. Rock, and M. J. Lee. Experiments in the coordinated control of an underwater arm/vehicle system. *Autonomous Robots*, 3:214–232, 1996.
[54] T. Sarpkaya and C. J. Garrison. Vortex formation and resistance in unsteady flow. *Trans. ASME Journal Applied Mechanics*, pages 16–25, 1963.
[55] I. Schjølberg and O. Egeland. Motion control of underwater vehicle-manipulator systems unsing feedback linearization. In *3rd IFAC Workshop on Control Applications in Marine Systems, CAMS'95*, pages 54–59, Trondheim, Norway, May 1995.
[56] C. G. Goodwin and R. L. Payne. *Dynamic System Identification: Experiment Design and Data Analysis*. Academic Press, New York, San Francisco, London, 1977.
[57] G. H. Golub and C. F. Van Loan. *Matrix Computations, third edition*. The Johns Hopkins University Press, Baltimore, London, 1996.
[58] L. Ljung. *System Identification theory for the user*. Prentice-Hall, Inc. New Jersey, USA, 1987.
[59] Y. Bar-Shalom and X-R. Li. *Estimation and Tracking Principles, Techniques and Software*. Artech House, Boston-London, 1993.
[60] M. Caccia, G. Indiveri, A. Tiano, and G. Veruggio. Experimental comparison of identification methods for an open-frame ROV. In *IFAC Conference on Marine Craft Maneuvering and Control, MCMC'97*, pages 1–6, Brijuni, Croatia, September 1997.
[61] A Alessandri, M Caccia, G. Indiveri, and G. Veruggio. Application of LS and EKF techniques to the identification of underwater vehicles. In *IEEE Int. Conf. on Control Applications, CCA'98*, pages 1084–1088, Trieste, Italy, September 1998.
[62] K. R. Goheen and E. R. Jefferys. The application of alternative modelling techniques to ROV dynamics. In *IEEE Int. Conf. on Robotics and Automation, ICRA'90*, pages 1302–1309, Cincinnati, Ohio, USA, May 1990.
[63] D. J. Fryxell. *Modelling, Identification and Control of an Autonomous Underwater Vehicle*. Master Thesis, Universidade Técnica De Lisboa, Istituto Superior Técnico, 1994.

[64] S. Ziani-Cherif, G. Lebret, and M. Perrier. Identification and control of a submarine vehicle. In *Fifth IFAC Symposium on Robot Control, SYROCO '97,* pages 327–332, Nantes, Francia, September 1997.

[65] D. B. Marco, A. Martins, and A. J. Healey. Surge motion parameter estimation for the NPS Phoenix AUV. In *International Advanced Robotics Program, IARP'98*, Lafayette, Lousiana, USA, February 1998.

[66] K. R. Goheen and E. R. Jefferys. Multivariable self-tuning autopilots for autonomous and remotely operated vehicles. *IEEE Jou. Oceanic Eng.*, 15(3):144–150, 1990.

[67] G. Bruzzone and E. Spirandelli. Caratterizzazione del modulo propulsore del veicolo romeo tramite prove sperimentali in tunnel di cavitazione. Technical Report 248 (in Italian), CNR-IAN, 1996.

[68] W. H. Press, S. A. Teukolsky, W. T. Vetterling, and B. P. Flannery. *Numerical Recipes in C*. Cambridge University Press, 1992.

[69] P. Barak. Smoothing and differentiation by an adaptive degree polynomial filter. *Analytical Chemistry*, 67(17):2758–2762, 1995.

[70] A. Alessandri, R. Bono, M. Caccia, G. Indiveri, and G. Veruggio. Experiences on the modelling and identification of the heave motion of an open-frame UUV. In *IEEE Oceans'98*, pages 1049–1053, Nice, France, September 1998.

[71] J. Swevers and C. Ganseman. Experimental identification of robot manipulators. In *Proc. Workshop Modelling and Control of Mechanical Systems, Imperial College Press*, pages 137–152, London, UK, 17-20 June 1997.

[72] J. Swevers, C. Ganseman, D. Bilgin Tükel, J. De Schutter, and H. Van Brussel. Optimal robot excitation and identification. *IEEE Transactions on Robotics and Automation*, 13(5):730–740, 1997.

[73] M. Nomoto and M. Hattori. A deep ROV "DOLPHIN 3K": Design and performance analysis. *IEEE Jou. Oceanic Eng.*, 11(3):373–391, 1986.

[74] B. Siciliano and K. P. Valavanis, editors. *Control Problems in Robotics and Automation*, chapter Free-Floating Robotic Systems, by O. Egeland and K. Y. Pettersen. Springer-Verlag, 1998.

[75] B. Siciliano and K. P. Valavanis, editors. *Control Problems in Robotics and Automation*, chapter Trends in Mobile Robot and Vehicle Control, by C. Canudas de Wit. Springer-Verlag, 1998.

[76] R. Colbaugh, E. Barany, and K. Glass. Adaptive control of nonholonomic robotic systems. *Journal of Robotic Systems*, 15(7):365–393, 1998.

[77] Brockett, Millmann, and Sussmann, editors. *Differential Geometric Control Theory*, chapter Asymptotic Stability and Feedback Stabilization, by Brockett, R. W., pages 181–191. Birkhauser, Boston, USA, 1983.

[78] O. Egeland, M. Dalsmo, and Sørdalen O. J. Feedback control of a nonholonomic underwater vehicle with a constant desired configuration. *Int. Jou. of Robotics Research*, 15(1):24–35, 1996.

[79] K. Y. Pettersen and O. Egeland. Position and attitude control of an underactuated autonomous underwater vehicle. In *35^{th} Conference on Decision and Control, CDC'96*,

pages 987–991, Kobe, Japan, December 1996.

[80] E. Badreddin and A. Astolfi. State feedback control of a nonholonomic mobile robot. In *33^{rd} Conference on Decision and Control, CDC'94*, Buena Vista, FL, USA, 14-16 December 1994.

[81] A. Astolfi. A unifying approach to the asymptotic stabilization of nonholonomic systems via discontinuous feedback. Technical Report 94-1, Automatic Control Laboratory, Swiss Federal Institute of Technology ETH-Zentrum, 8092 Zurich, Switzerland, 1994.

[82] G. Casalino, G. Cannata, and M. Caccia. Lyapunov based closed-loop motion control for UUVs. In *3rd International Symposium on Methods and Models in Automation and Robotics*, pages 469–474, Miedzyzdroje, Poland, September 1996.

[83] L. E. Dubins. On curves of minimal length with a constraint on average curvature, and with prescribed initial and terminal positions and tangents. *American Journal of Mathemathics*, 79:497–516, 1957.

[84] J. A. Reeds and L. A. Shepp. Optimal paths for a car that goes both forwards and backwards. *Pacific Journal of Mathematics*, 145(2):367–393, 1990.

[85] J. Boissonnat, A. Cérézo, and J. Leblond. Shortest paths of bounded curvature in the plane. In *IEEE Int. Conf. on Robotics and Automation, ICRA'92*, pages 2315–2320, Nice, France, May 1992.

[86] X. Bui, J. Boissonnat, P. Souères, and J. Laumond. Shortest path synthesis for dubins non-holonomic robot. In *IEEE Int. Conf. on Robotics and Automation, ICRA'94*, pages 2–7, 1994.

[87] G. Desaulniers and F. Soumis. An efficient algorithm to find a shortest path for a car-like robot. *IEEE Transactions on Robotics and Automation*, 11(6):819–828, 1995.

[88] D. B. Reister and S. M. Lenhart. Time-optimal paths for high speed maneuvering. *Int. Jou. of Robotics Research*, 14(2):184–194, 1995.

[89] A. M. Shkel and V. J. Lumelsky. On calculation of optimal paths with constrained curvature: the case of long paths. In *IEEE Int. Conf. on Robotics and Automation, ICRA'96*, pages 3578–3583, Minneapolis, Minnesota, USA, April 1996.

[90] A. Bicchi, G. Casalino, and C. Santilli. Planning shortest bounded curvature paths for a class of nonholonomic vehicles among obstacles. In *IEEE Int. Conf. on Robotics and Automation, ICRA'96*, Minneapolis, Minnesota, USA, April 1996.

[91] P. Moutarlier, B. Mirtich, and J. Canny. Shortest paths for a car-like robot to manifolds in configuration space. *Int. Jou. of Robotics Research*, 15(1):36–60, 1996.

[92] G. Desaulniers, F. Soumis, and J. C. Laurent. A shortest path algorithm for a car-like robot in a polygonal environment. *Int. Jou. of Robotics Research*, 17(5):512–530, 1998.

[93] R. J. Szczerba, D. Z. Chen, and J. J. Uhran. Planning shortest paths among $2D$ and $3D$ weighted regions using framed subspaces. *Int. Jou. of Robotics Research*, 17(5):531–546, 1998.

[94] Y. Kanayama and B. Hartman. Smooth local path planning for autonomous vehicles. *Int. Jou. of Robotics Research*, 16(3):263–284, 1997.

[95] A. M. Hussein and A. Elnagar. On smooth and safe trajectory planning in $2D$ environments. In *IEEE Int. Conf. on Robotics and Automation, ICRA'97*, pages 3118–3123,

Albuquerque, New Mexico, USA, April 1997.

[96] J. Reuter. Mobile robots trajectories with continuously differentiable curvature: An optimal control approach. In *Int. Conference on Intelligent Robots and Systems, IEEE RSJ'98*, pages 38–43, Victoria, B.C., Canada, October 1998.

[97] A. M. Bruckstein and A. N. Netravali. On minimal energy trajectories. *Computer Vision, Graphics, and Image Processing*, 49:283–296, 1990.

[98] B. K. P. Horn. The curve of least energy. *ACM Transactions on Mathematical Software*, 9(4):441–460, 1983.

[99] M. Kallay. Plane curves of minimal energy. *ACM Transactions on Mathematical Software*, 12(3):219–222, 1986.

[100] D. S. Meek and D. J. Walton. The use of cornu spirals in drawing planar curves of controlled curvature. *Journal of Computational an Applied Mathematics*, 25:69–78, 1989.

[101] L. E. Elsgolts. *Equazioni Differenziali e Calcolo delle Variazioni*. Editori Riuniti, Edizioni MIR, Roma (in Italian), 1981.

[102] G. Indiveri, G. Cannata, and G. Casalino. Analytical synthesis of least curvature $2D$ paths for underwater applications. In *6th IEEE Mediterranean Conference on Control and Automation*, Alghero, Italy, June 1998.

[103] Y. Kanayama and B. Hartman. Smooth local path planning for autonomous vehicles. In *IEEE Int. Conf. on Robotics and Automation, ICRA'89*, pages 1265–1270, 1989.

[104] S. Fleury, P. Souères, J. Laumond, and R. Chatila. Primitives for smoothing mobile robot trajectories. In *IEEE Int. Conf. on Robotics and Automation, ICRA'93*, pages 832–839, Atlanta, Georgia, USA, May 1993.